Doctoral theses at NTNU, 2022:369

Sohail Shah

Atom probe tomography investigations of aging of Al-Zn-Mg(-Cu) alloys during room temperature storage or by cyclic plasticity

Doctoral thesis

NTNU
Norwegian University of Science and Technology
Thesis for the Degree of
Philosophiae Doctor
Faculty of Natural Sciences
Department of Materials Science and Engineering

NTNU
Norwegian University of
Science and Technology

Sohail Shah

Atom probe tomography investigations of aging of Al-Zn-Mg(-Cu) alloys during room temperature storage or by cyclic plasticity

Thesis for the Degree of Philosophiae Doctor

Trondheim, Desember 2022

Norwegian University of Science and Technology
Faculty of Natural Sciences
Department of Materials Science and Engineering

NTNU
Norwegian University of
Science and Technology

NTNU
Norwegian University of Science and Technology

Thesis for the Degree of Philosophiae Doctor

Faculty of Natural Sciences
Department of Materials Science and Engineering

ISBN 978-82-326-6580-8 (printed ver.)
ISBN 978-82-326-6973-8 (electronic ver.)
ISSN 1503-8181 (printed ver.)
ISSN 2703-8084 (online ver.)

Doctoral theses at NTNU, 2022:369

Printed by NTNU Grafisk senter

Preface

This thesis is submitted in fulfilment of requirements for the Doctor of Philosophy degree (Ph.D.) at Norwegian University of Science and Technology, Trondheim (NTNU). The doctoral work contained has been carried out at the Department of Materials Science and Engineering (DMSE), NTNU, in the period from July 2019 to July 2022.

This work has been carried out under the main supervision of professor Bjørn Holmedal, at DMSE, NTNU, and co-supervisions of Randi Holmestad at Department of Physics, NTNU, Dr. Calin Marioara and Dr. Sigurd Wenner at SINTEF Industry.

The thesis consists of two main parts. The first part includes the background, introduction and experimental methodologies relevant to this work. The second part contains four papers which have been published or prepared for submission. These papers present the core work and results of the candidate in the Ph.D. project.

Sohail Shah
Trondheim, July 2022

Publications included in this thesis:

Paper 1: ***Sohail Shah,*** Elisabeth Thronsen, Constantinos Hatzoglou, Sigurd Wenner, Calin D. Marioara, Randi Holmestad, and Bjørn Holmedal. "Effect of cyclic ageing on the early-stage clustering in Al–Zn–Mg (-Cu) alloys." *Materials Science and Engineering: A* (2022): 143280.

Paper 2: ***Sohail Shah,*** Akash Gopal, Elisabeth Thronsen, Constantinos Hatzoglou, Bjørn Holmedal. "Precipitation, mechanical properties and early slant ductile fracture in cyclic and naturally aged Al-Zn-Mg(-Cu) alloys"**.** Submitted in *Materials and Design*.

Paper 3: ***Sohail Shah,*** Elisabeth Thronsen, Frederic De Geuser, Constantinos Hatzoglou, Calin D. Marioara, Randi Holmestad, Bjørn Holmedal. "Comparison of a cluster identification method to a statistical approach for analyzing atom probe tomography data for GP zones in Al-Zn-Mg(-Cu) alloys"**.** Manuscript ready for submission in *Microscopy and Microanalysis.*

Paper 4: Elisabeth Thronsen, ***Sohail Shah,*** Constantinos Hatzoglou, Calin D. Marioara, Sigurd Wenner, Sigmund J. Anderson, Bjørn Holmedal, Randi Holmestad. "The evolution of precipitates in an Al-Zn-Mg alloy". Ready for submission in *Journal of Alloys and Compounds.*

Other scientific contributions:

Poster presentation: Atom Probe investigation of early-stage clustering by cyclic ageing in Al-Zn-Mg-(-Cu) alloys. ***Sohail Shah,*** Akash Gopal, Constantinos Hatzoglou, Bjørn Holmedal, May 8th -13th, 2022, Hawaii, USA.

Acknowledgements

These three years of my PhD journey brought me to the shore of great knowledge, creativity, and gratitude, anew; well equipped to face life ahead in all its glory. It was a profoundly humbling experience which steered me towards rediscovering my passion for science. Today, I stand in awe of the many people who helped me nurture my scientific outlook and paved the way for impactful research. Firstly, I want to extend my appreciation to Prof. Bjørn Holmedal, my primary supervisor aka my role model. His patient temperament, meticulous scrutiny down to dissecting every figure legend, timely advice encouraged me undertake each task as a learning challenge with an open mind. His long brainstorming sessions led to some good ideas being put forward in this thesis. My co-supervisors Dr Calin Marioara, Sigurd Wenner and Prof. Randi Holmestad molded this project with their intellect rigor and helpful feedbacks. A big thank you to Frederic De Geuser for his inputs and guidance in APT related methodologies for data interpretation using statistical approach. His understanding of APT related issues has given me an interesting path to explore during my PhD.

Special thanks to Dr. Constantinos Hatzoglou for his immense 'behind the screen' help with experimental methodologies and data interpretation. Your willingness to teach from scratch and providing valuable insights was truly admired. A big thank you for your inputs and dynamic approach to the problems encountered.

Many thanks to Pål Christian Skaret and Marit Olaisen Odden for their assistance with test setups and mechanical testing. Akash Gopal has been incredibly helpful with mechanical testing and discussions on the cyclic aging study. Elisabeth Thronsen has been a very nice colleague sharing her expertise in TEM and contributing immensely to discussions for many of the studies carried out in this thesis. Hanne Sofie-Søreide is thanked for her help and support in the APT lab and providing her valuable feedbacks on sample preparation and other APT related tasks.

An overall fun and learning atmosphere created at the DMSE has helped create many friendships and memories. Thank you for providing an uplifting atmosphere of scientific zeal and thorough professionalism for conducting this research. A big thank you to my colleagues;

Shiwei Pan, Arash Imani Aria, Hassan Morradi Asadkandi, Chunan Li, Feng Lu, Christoph Hell and Abdulla bin Afif.

Finally, a big thank you to my family who have stuck with me during the highs and lows of this intense period. The great sacrifices and their unwavering love and support has pushed me forward in this journey. You all are truly inspirational. I would like to dedicate this thesis to my dear mom whose words of encouragement and prayers continue to ring in my ears.

List of Acronyms

APT Atom Probe Tomography

TEM Transmission Electron Microscopy

CA Cyclic Ageing

PA Peak Age

NA Natural Age

RT Room Temperature

AA Artificial Age

TCO Truncated Octahedron

DSA Dynamic Strain Ageing

PCF Pair Correlation Function

RDF Radial Distribution Function

SHT Solution Heat Treatment

DIC Digital Image Correlation

CPS Cumulative Plastic Strain

IPM Iso Position Method

MSM Maximum Separation Method

TMP Thermomechanical Processing

FCC Face Centered Cubic

SSSS Supersaturated Solid Solution

HAADF-STEM High angle annular dark field scanning transmission electron microscopy

AQ As Quenched

OIM Orientation Imaging Microscopy

FIM Field ion Microscopy

ICF Image Compression factor

EPF Equivalent Pulse Fraction

GP Guinier-Preston

VRC Vacancy-rich clusters

EDS Energy dispersive X-ray spectroscopy

FFT Fast Fourier Transform

SPED Scanning Precession Electron Diffraction

Abstract

Aluminum (Al) alloys constitute an important group of engineering materials that find extensive usage owing to their properties, which include high strength to weight ratio, excellent conductivity, corrosion resistance and ease of forming. Al has rapidly become one of the most used materials in automotive applications driven by the demands to limit carbon dioxide emissions coupled with emphasis on less energy consumption in producing it. Yield strength and work hardening are important criteria for design and thermo-mechanical processing of Al alloys.

High strength Al alloys require a series of temperature treatments (typically between (120ºC to 200ºC) to form a high number density of nanoparticles. The motivation of this study is to investigate alternative methods of strengthening Al alloys and understanding the strength imparted to them using principle scientific instruments like atom probe tomography (APT) and transmission electron microscopy (TEM). APT is an excellent tool that enables the characterization of the chemistry of materials with nanometer resolution in three dimensions due to its high chemical sensitivity. This enables the study of different types of precipitate phases, their distribution, sizes and number densities in the alloy microstructure. The TEM also is used as a complementary tool to accurately quantify the clusters studied for the respective conditions owing to its higher resolving power and crystal structure determination.

The cyclic application of mechanical stress to Al alloys at room temperature, referred to as cyclic ageing (CA) is studied for Al-Zn-Mg(-Cu) alloys. These alloys are otherwise mostly used for automotive applications. CA causes dynamic precipitation of fine solute clusters that are uniformly distributed throughout the bulk and are responsible for enhancing the mechanical properties. Similar strengths and uniform elongations as compared to the peak aged (PA) condition is demonstrated for two 7xxx series of Al alloys, one containing copper (Cu) and one without. APT and TEM investigations confirmed a high number density of solute clusters exhibiting structural similarities to the GPI zones which are usually seen in natural ageing (NA) in such alloys. CA followed by 10 days of NA allowed these early-stage clusters to grow into more stable ones, thereby further improving the mechanical response. However, the structure of these clusters is fundamentally identical to the GPI zones observed during the NA, consisting of the truncated octahedron (TCO) building block.

Special emphasis on the fracture mode of the CA samples showed shear/slant fracture occurring at the same point as reaching maximum strength, i.e., the uniform limit. Interestingly, this was also seen for the NA samples. This, however, contrasted with the PA condition which underwent diffuse necking and exhibited the conventional post-necking ductility. Artificial aging (AA) of the CA and NA conditions restored a necking behavior similar as the one seen in the PA condition. The NA and CA conditions had similar microstructure, which is completely different from that of the PA condition, indicating that the precipitate structure controls the fracture type. The probable effect of dynamic strain aging (DSA) is also studied

with low temperature tests and strain mapping. From these tests, it could be concluded that DSA is not solely responsible on the early premature fracture of the studied 7xxx alloys.

Cluster identification in APT is typically challenging when considering clusters as small as the ones observed in CA and early-stage NA. The lateral resolution in the APT is heavily affected due to the variations in the electrostatic field observed as a result of the presence of chemical fluctuations (clusters and precipitates). This results in deflection of ion trajectories, and hence it is challenging to quantify the relevant information obtained. We adopt the pair correlation functions (PCF) methodology, based on the radial distribution functions (RDF) as a complementary methodology to quantify the early-stage clustering observed in the 7xxx alloys studied in this work. This is in addition to the iso-position methodology used to identify clusters and extract metallurgical information. The advantage of the PCF methodology being, it is a parameter independent methodology which extracts an average value of the entire dataset and serves as a robust methodology to quantify the chemical fluctuations.

The evolution of precipitates has been studied in the 7003 alloy. The alloy was NA for 1 year and was subjected to AA at 140°C to revisit the precipitation sequence in Al-Zn-Mg alloys. Dense population of GPI zones were observed in the NA condition with a small fraction of η' precipitates, as confirmed by TEM. With 10 minutes of AA, the hardness sharply drops form 121 HV to 88 HV. Similar number densities of clusters were observed as compared to the NA condition, however the Zn/Mg ratio decreased from 2 to 1.7 with a slight increase in the solute content in the matrix between the two conditions. The clusters were disordered and smaller, no longer exhibiting the GPI atomic structure. After a further 5 hours of AA at 140°C, η' was the dominant phase. This study helps understand the precipitation sequence in Al-Zn-Mg alloys better, with focus on the early stages of ageing.

Table of Contents

BACKGROUND

Chapter 1 Introduction

1.1 Motivation

Strengthening of aluminum (Al) alloys by solid state precipitation is one of the most effective and widely used strengthening methods currently. High strength Al alloys find a wide variety of applications in the automotive and the transport industry. The Al alloys used more commonly in the transport applications, include the 2xxx (Al-Cu-Mg), 6xxx (Al-Mg-Si) and 7xxx (Al-Zn-Mg) systems [1, 2]. Alloy strength is achieved by developing a fine distribution of uniform nanoscale particles, which impede the motion of dislocation, thereby increasing the strength for the above-mentioned Al alloy systems [3-8]. This is mostly achieved by thermo-mechanical processing, where the key issue is to control the nucleation and growth of these nano-sized precipitates. Many approaches have been tried to obtain a high nucleation rate like pre-straining the material after solution treatment (SHT) and before thermomechanical ageing [9, 10]. This introduces dislocations, which serve as heterogenous nucleation sites for precipitates during further heat treatments. Addition of certain trace elements has also been linked to interact with vacancies, such that they help catalyze nucleation of precipitates. Silver (Ag) + manganese (Mn) additions or Sn additions to Al-Cu alloys aids in higher nucleation of precipitates[11, 12].

Recently, Sun *et al.* [13] demonstrated a novel approach for precipitating a high number density of clusters, enabling the strengths to reach as high as that of the conventional peak aged material. The novel cyclic strengthening approach involves cyclic deformation of a solution heat treated and quenched 2xxx, 6xxx and 7xxx industrial alloy. During plastic deformation, the back-and-forth gliding of dislocations creates vacancies that are continuously produced during dragging of jogs. Local diffusion of solute is a consequence of the excess vacancies generated. The extremely fine distribution of solute clusters being formed, contributes to a major part of the strength, in a similar manner to that of the conventional artificially aged samples.

New challenges emerge when novel processing methods lead to even stronger properties but their behavior when exposed to in service conditions or elevated temperatures remain a

question mark. In this study, we focus on Al-Zn-Mg(-Cu) alloys consistent to precisely understand the cyclic strengthening mechanisms identical to those obtained by Sun *et al.* A fundamental understanding of this behavior and correlating the microstructure using the Atom Probe Tomography (APT) complimented by TEM to the mechanical response of the cyclically strengthened 7xxx system are the major motivations of this PhD.

Quantification of early-stage clusters in APT has been challenging, due to the lateral resolution being affected by variations of the electrostatic field between different phases that cause deflections in the trajectories of ions to the detector [14]. With clusters studied in this work being within the resolution limit of the APT, as suggested by De Geuser *et al* [15], identifying and quantifying these fine clusters is challenging. Moreover, cluster identification methodologies use fixed thresholds which is challenging to obtain and reproducible results. In this regard, the large volumes of microstructural information gained by APT will be used to implement the parameter free methodology of PCF to quantify clusters. This would serve as an additional tool to verify trends and quantitatively assess the metallurgical information extracted from APT such as number densities, volume fractions, solute ratios, and size distributions.

1.2 Objectives and scope

The material studied in this work are mainly Al-Zn-Mg(-Cu) alloys. The overall project objective is to establish a scientific basis based on a large volume of microstructural information gained through advanced APT work and correlate it to the mechanical response of the cyclically strengthening phenomenon. Plate materials are mainly studied in this work, however, axisymmetric 6xxx alloys have also been investigated to assess the effect of texture affecting the fracture modes and accumulated plastic strains. This is done in collaboration with a master's student in the same project. Keeping the overall goal in mind, the secondary objectives, which are directly relevant to this PhD, involve:

- Optimization of processing parameters for room temperature cyclic aging (CA) at different frequencies, stress, and number of cycles.
- Implement digital image correlation [16] methodology to quantify the strain measurements and accurate calculations of cumulative plastic strains (CPS) during CA.
- Study the fracture modes observed in conventionally aged and CA samples for extruded plates and compare it to axis-symmetric modes.

- Investigate the fracture modes for plate type 7xxx and 6xxx alloys and that of axi-symmetric 6xxx alloys.
- Conduct APT analysis on the CA conditions and quantify the chemistry of early-stage clusters formed.
- Summarise the CA effect on the strength and compare it to natural ageing (NA) by correlating the microstructure utilizing the APT and TEM methodologies.
- Comparing the cluster identification methodologies of iso-position (IPM) and maximum separation (MSM) to a parameter free method to quantify early-stage clustering in the Al-Zn-Mg(-Cu) alloys.
- Study the evolution of precipitates in Al-Zn-Mg systems to complement the TEM and to quantify the chemistry and correlate morphology of different phases through different heat treatments.

This PhD thesis is organized into two parts:

The section ***'Background'*** contains the following chapters:

Chapter 1 outlines the motivation and scientific background of this research work.

Chapter 2 focuses on giving an overview of the precipitation in Al alloys and more specifically dynamic precipitation in 7xxx system.

Chapter 3 discusses the APT experimental methodology, reconstruction parameters and optimizations for 7xxx system.

Conclusions and future work are addressed in Chapter 4.

The section ***'Research'*** contains the four articles produced during the PhD.

Chapter 2 Aluminum alloys and strengthening

2.1 The Al alloy system

The use of metals is one of the main cornerstones of the technological advancements that have been made over the past few decades and can be seen in our everyday lives. For instance, there is ever growing demand for fuel efficient vehicles in the automotive industry to reduce air pollution and reduce energy consumption. Al is widely used as a structural material giving emphasis to the mechanical properties. Despite pure Al having a yield strength of around 7-10 MPa, alloying Al with different elements (Zn, Mg, Si, Cu) coupled with different heat treatments, the mechanical response can be tremendously improved [17]. The age-hardening Al-Zn-Mg, Al-Cu and Al-Mg-Si alloy systems exhibit yield strengths from 200 to 600 MPa, greatly exploiting the precipitation strengthening phenomenon. Furthermore, in addition to the material strength, many additional properties such as ductility, weldability, formability and corrosion resistance can also be improved. Based on specific applications, it is the optimization of various properties that has given rise to many different alloying systems.

In the following section, the microstructural origins of Al alloys' properties are explained. The use of Al-Zn-Mg(-Cu) system is used as a main example, due to its high relevance to the research carried out in this PhD.

2.2 Processing of Al alloys

The effect of thermal ageing and mechanical processing- together denoted as thermomechanical processing (TMP), has been widely used in industrial applications. Figure 1 shows an example of the industrial TMP steps for an extruded 7xxx alloy. The materials will undergo changes in microstructure in all the processing steps, having consequences on the final material properties. The first steps of casting and extrusion indicated in Figure 1 is mainly used to shape and form the material while the solution heat treatment (SHT) and artificial ageing [18] are important for the formation of precipitate phases.

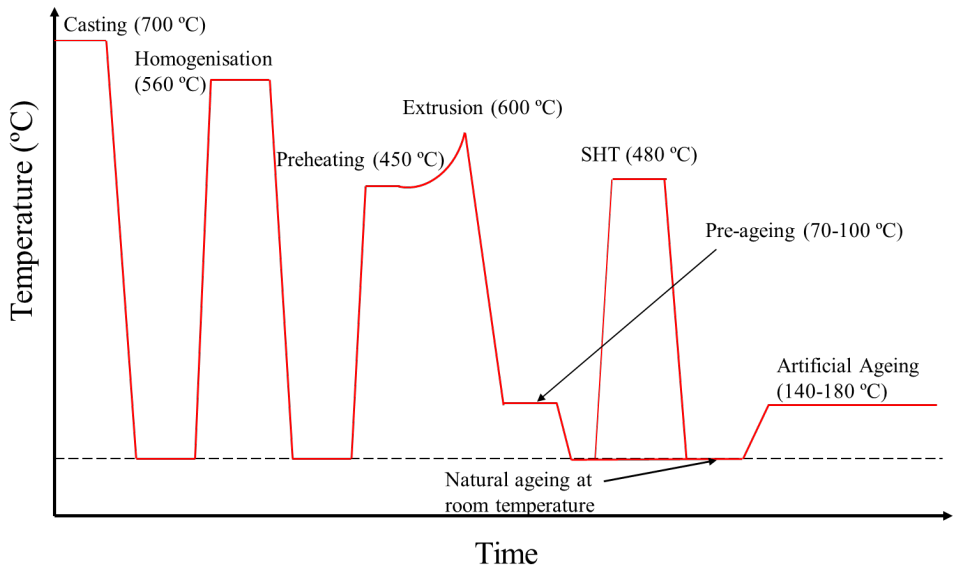

Figure 1. The thermomechanical processing carried out on extruded aluminum alloys.

Since the solubility of alloying elements is limited in Al, secondary phases are formed in order to minimize the total energy of the system. When an SHT treatment is carried out, the solute is uniformly distributed in the face-centered cubic (FCC) Al matrix. A rapid quench allows a high concentration of vacancies to appear, along with the solute in a state of non-equilibrium generally referred to as supersaturated solid solution (SSSS) [19]. The solute present in SSSS diffuses with the aid of vacancies by substitutional diffusion, which eventually nucleates atomic clusters that are regions enriched in solute. The nucleation is a result of a negative free energy change, while the growth/coarsening is a result of the balance between two forces: precipitate-matrix interface energy and volume free energy. It also depends on the lattice strain energy component. If we assume a cluster to be spherical this can be expressed as:

$$\Delta G_{total} = -\frac{4}{3}\pi r^3 \Delta G_b + 4\pi r^2 \gamma + 4\mu\delta^2 V \quad (1)$$

Where, ΔG_{total} is the change in free energy, r is the radius of the cluster, ΔG_b is the bulk free energy and γ is the interfacial energy. The term δ exists as the new phase formed can have a

different lattice parameter to the existing phase. μ is the shear modulus of the matrix and V is the volume of the unconstrained hole in the matrix. A more detailed understanding of cluster nucleation and growth can be found elsewhere [20-24].

2.3 Precipitation in Al-Zn-Mg alloys

The main strengthening potential of age-hardening Al alloys comes from the high density of nano sized precipitate phases formed due to thermal ageing. Precipitation involves the formation of a phase which is different in composition and crystal structure to that of the host matrix. This is usually in a sequence, with multiple metastable phases forming towards the equilibrium crystal structure. In typical 7xxx Al alloys, several different precipitate sequences exist and are partly dependent on the alloy composition, quenching condition and ageing temperatures[25-27]. The formation of metastable precipitates has a strong influence on the nucleation of other stable phases, which also allows the use of multiple step ageing to optimize properties. In the following section, we will discuss the precipitation sequence of Al-Zn-Mg(-Cu) alloys as it is the alloy system mainly investigated in this work.

2.3.1 GP zones

The established precipitation sequence for Al-Zn-Mg alloys is given as [28-31]:

$$\text{SSSS} \rightarrow \text{solute clusters} \rightarrow \text{GP zones(GPI and GPII)} \rightarrow \eta' \rightarrow \eta(MgZn_2) \qquad (2)$$

Clustering of solute in the as quenched state starts immediately which was detected by a rapid increase in hardness and electrical resistivity by Juhasz *et al.* [32]. Near room temperature, the formation of GPI zones occurs and quenched in vacancies play an important role in accelerating the rate of GPI zone formation by accelerating the diffusion process [33, 34]. HRTEM investigations have revealed that the GPI zones formed at room temperature are spherical and fully coherent with the Al matrix [35]. Both Zn and Mg take part in the formation of zones, though the rate of the process is controlled more by the motion of Mg atoms [30]. The atomic structure of GPI zones for 7xxx was recently determined and were found to be built by a single building block that connects along certain directions in the Al matrix. The basic unit can be

described as a truncated cube octahedron (TCO), consisting of three shells centered on a possible interstitial with a Zn/Mg ratio close to 2 [36]. An upper limit of temperature at which no GP zones formation exists, is noted to be around 120 ± 5ºC [37]. Usually, a multi-step ageing process, which generally involves a room temperature storage after quench, is followed. The first step involves ageing at a temperature lower than the dissolution temperature, to form a high number density of GP zones. GP zones formed at room temperature also act as nucleation sites for more stable precipitates. The second step (aging at 120ºC- 170ºC) involves the formation of the main hardening phase (η′).

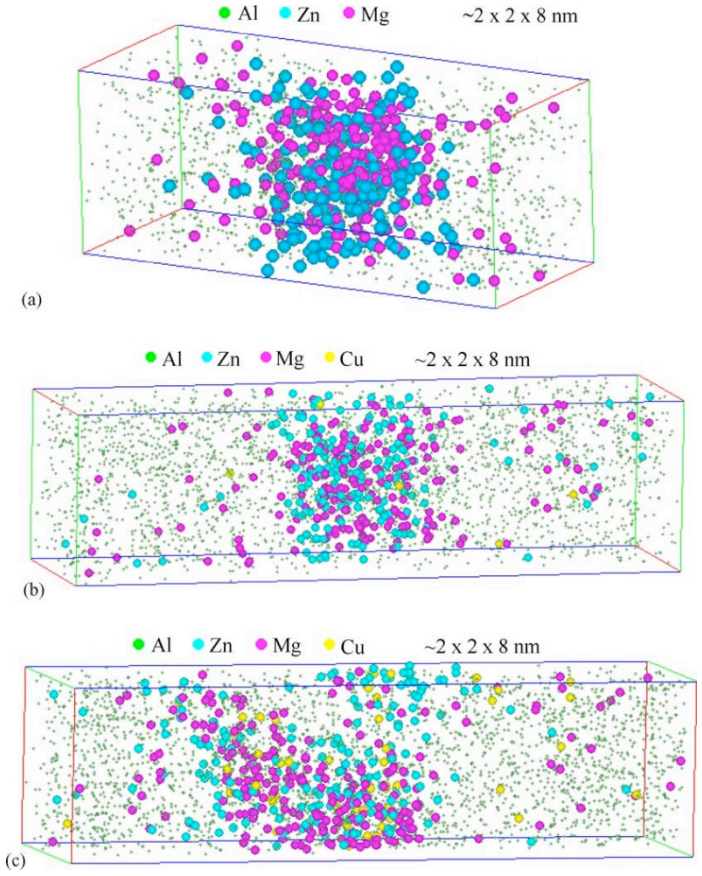

Figure 2. APT mapping of (a) spherical GP zone in a ternary 7xxx alloy, (b) spherical GP zone in a quaternary 7xxx alloy and (c) ellipsoidal GP zone of a quaternary alloy [38]. Reprinted by permission from Elsevier publishers.

The other type, called the GPII zone, forms above 70ºC from vacancy solute clusters (VRC), as exemplified in Equation (2) and when quenched from temperatures above 450ºC. These are elongated ellipsoidal in shape and are seen as more stable and may serve as nucleation for the semi-coherent η′ phase [39]. Figure 2 shows the two different types of GP zones detected by APT for a ternary and Cu containing quaternary 7xxx alloy system. The GPII zones shown in Figure 2(c) are ellipsoidal in shape and the Cu content is high, as reported by Chinh, N. Q., *et al.* [40].

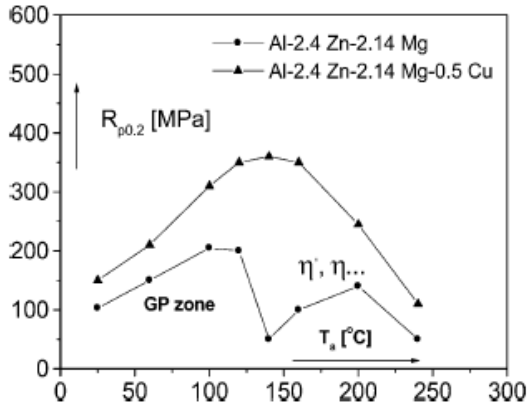

Figure 3. The effect of 2 hours of ageing at different temperatures on the YS of two different alloys investigated [40]. Reprinted by permission from Elsevier publishers.

The effect of Cu is seen to increase considerably the age hardening response potential in alloys as compared to alloys without Cu. Cu is not involved in the formation of new phases, rather, it increases the strength contribution per cluster along with refining the microstructure [41, 42]. Addition of 3 at.% Cu results in increase of hardness after quench with the nucleation of GPII zones, as seen by Fang, Xu, *et al.* [43]. These are quaternary high strength alloys which have very limited or no weldability.

The transition from GP zones to the main hardening phase is supported by two mechanisms:

- Complete reversion: When the alloy is heated to sufficiently high temperatures such that the volume fraction of GP zones decreases to the as quenched state, it is termed as

'reversion', as was first observed in the 1920s [30]. In such a case, the physical properties measured (hardness and mechanical properties) reach that of the AQ state.

- Partial reversion: Dissolution of GP zones and the nucleation of η′ takes place simultaneously. In such a case, the physical properties measured do not reach that of the AQ state. GP zones exceeding a critical size do not dissolve and serve as nucleation sites for η′ in such a case [44].

The transition from GP zones to the intermediate phase is more smoother without the reversion of GP zones, as reported by Chinh, N. Q., [40] also seen in Figure 3. The early-stage strength of Cu containing alloys is found to be higher than the Cu free alloy due to the presence of VRCs rich in Cu.

2.3.2 The η' phase

Upon ageing at temperatures higher than formation of GP zones, the maximum strength attained in Al-Zn-Mg alloys is associated with a metastable η′ phase. The formation of η′ is predominant at temperatures 120ºC- 170ºC [45], however, a small fraction of η′ nucleation has also been observed in long term NA of Al-Zn-Mg alloys. These are plate like precipitates on $\{111\}_{Al}$ and semi-coherent with the aluminum matrix . There are in total 13 reported η-phases with the Al matrix [26, 27] and have a hexagonal structure [46] with lattice parameters of a = 0.496 nm and c = 1.403 nm. Marioara *et al.* [47] resolved the structure of η′ and η_2 using the high angle annular dark field scanning transmission electron microscopy (HAADF-STEM) and labeled them as 'Type 1' and 'Type 2', respectively. VRCs have been found to be important in the nucleation of η′ in the case of low alloying element concentrations [30]. However, GP zone to η′ transition has also been a dominant mechanism studied by many groups [44] and is also one of the topics in this study. Other studies have linked nucleation of η′ to stacking faults, but without any direct observation [27, 31]. Partial reversion has been explained in several ways, one presuming that the overcritically sized GP zones can directly transform into nuclei of the η′ phase [27, 48, 49]. The role of VRCs is also highlighted as a potential nucleus for η′ phase with the co-precipitation of GPI and VRCs during preaging [50]. It is possible that two types of GP zones do form during preaging and the less stable one's dissolve feeding solute to the matrix while the more stable ones could be potential nuclei for

η′. Quenching to a temperature of artificial aging directly has been found to give a heterogenous nucleation of metastable precipitates [51]. This could possibly be on the VRCs or other heterogeneities. The two-step ageing process commonly used in 7xxx alloys allows the room temperature NA to increase the GP zones which in turn decreases the VRC formed immediately after the SHT.

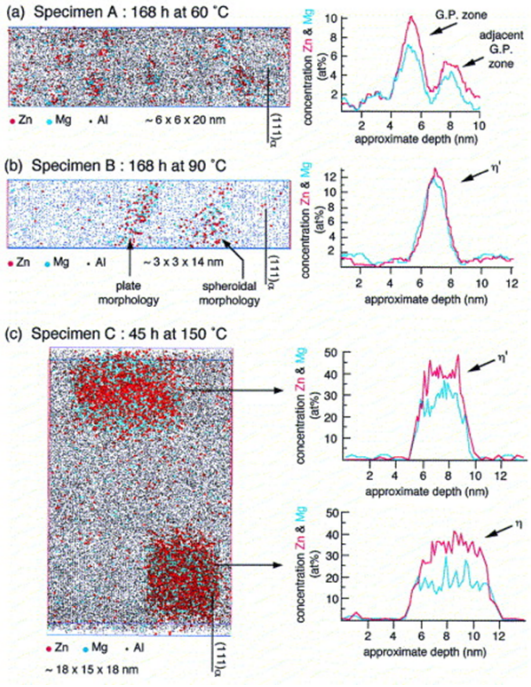

Figure 4. APT analysis and concentration profiles of precipitates present in specimens aged for (a) 168 h at 60ºC, (b) 168 h at 90 ºC and (c) 45 h at 150 ºC [52]. Reprinted by permission from Elsevier publishers.

Figure 4 shows the different types of precipitates during different aging treatments. A Zn/Mg ratio close to 1.4 has been quantified based on the APT results for η′ [52]. Zhao *et al.* [18] studied the composition evolution at different aging time and precipitate state for an Al-Zn-Mg(-Cu) alloy. A high number density of precipitates of the order 10^{24} m^{-3} was seen after 30 minutes of aging at 120ºC. The composition of precipitates plateau's after this until the peak aged state (12 hours at 120ºC) since this aged at a lower temperature than the typical aging temperature for peak age, the precipitates are still GP zones, in agreement with Marlaud *et al.*

[53]. In the over-aging state however, the composition was more compatible with that of η′. This study also highlights the stability of GP zones up to 120ºC.

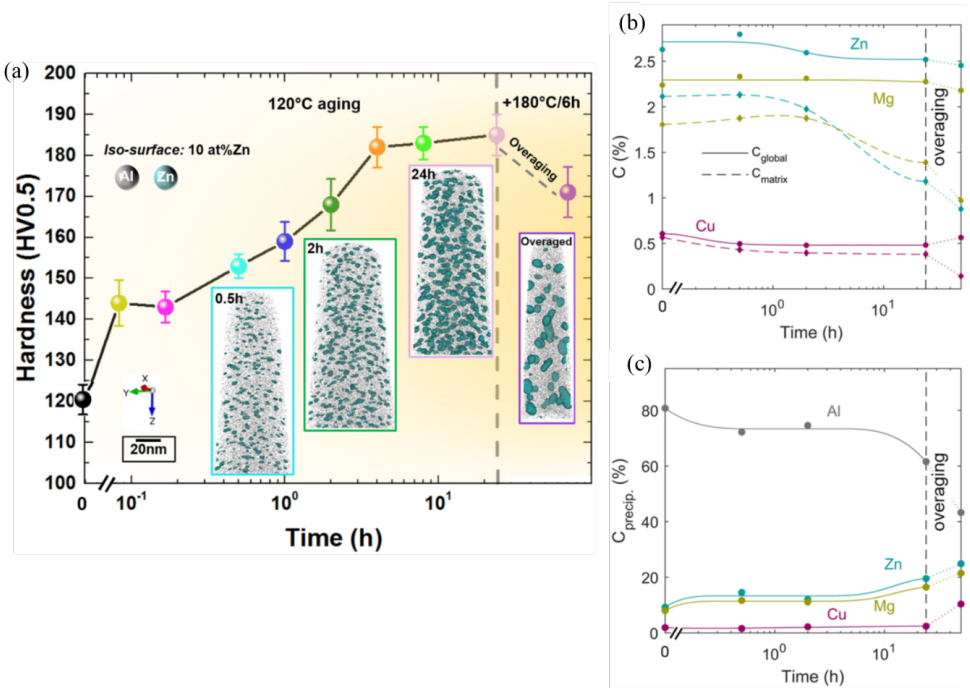

Figure 5. (a) Hardness evolution of the different precipitate state analyzed by APT. Composition evolution of the entire dataset along with the matrix composition shown in (b) and composition evolution for the precipitates shown in (c) as a function of different aging time [18]. Reprinted by permission from Elsevier publishers.

The equilibrium phase is considered to have a Zn/Mg close to 2 in accordance with its equilibrium concentration ($MgZn_2$), however, the crystal structure of the equilibrium phase is different and is not a semi-coherent phase like the η′.

2.4 Strengthening by dynamic precipitation

This section aims at providing an understanding of the dynamic precipitation occurring in metals and specifically in aluminum alloys. Later, the concept of low cycle fatigue on aluminum alloys and its effect on precipitation is highlighted.

2.4.1 Dislocation interaction

The dislocations that exist in a crystal lattice are in general mixed dislocations, for which edge and screw dislocations are special cases. A slip plane, contains the dislocation line and the Burgers vector. The main difference between the screw and the edge dislocation is that the burgers vector and dislocation line are perpendicular for a pure edge dislocation while they are parallel for a screw dislocation.

In metals, dislocations interact during plastic deformation. Three different types of interaction products are formed during the crossing of two dislocations: length-change, jog or kink [54]. A jog is a step on the dislocation line out of the plane, with length and magnitude equal to the Burgers vector of the other dislocation.

The glide plane of a dislocation has to contain its burger's vector and the dislocation line. Hence, when a screw dislocation receives a jog, the jog does not have a glide plane to glide along with the dislocation. As a consequence, the dragging of the jogs during the gliding of the dislocation leave behind dipole loops as seen in Figure 6. As a screw dislocation at some point stops, say being temporarily arrested at a set of sufficiently strong obstacles, it will have attached a number of such dipoles, which could be alternatively considered as either be a chain of vacancies or an extra line of self-substitutional atoms. During the time the dislocation is not moving, there is time for diffusion and the dipoles will pinch off into loops of self-interstitial or vacancy type. The vacancy loops formed, have a high concentration of vacancies leading to a non-equilibrium state in the localized region eventually causing diffusion of these vacancies into the surrounding bulk. This enables the vacancies to be utilized for nucleation or growth of precipitates (in our case, since we have underaged condition of the 7xxx alloys, we are precipitating GP zones).

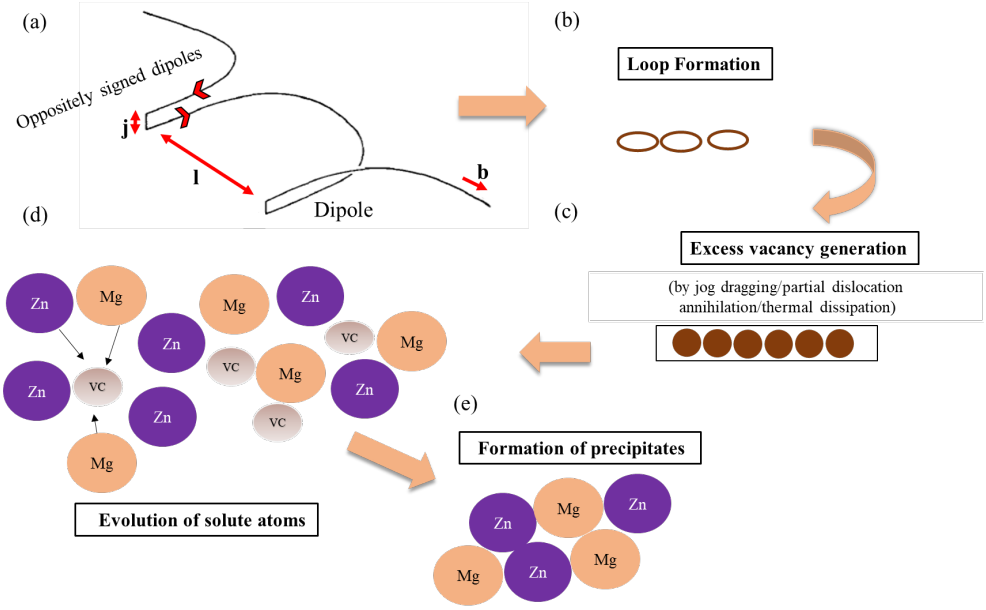

Figure 6. Schematic representation of formation of vacancies and precipitation during cyclic ageing.

2.4.2 Coupling dynamic precipitation and thermal aging

The conventional elevated temperature aging to induce precipitation has been used for many decades to obtain high strength states. The vacancies play an important role for the precipitation and are required to facilitate substitutional diffusion of the solute atoms playing a role for cluster/precipitates nucleation. In general, diffusion, and hence precipitation kinetics, are faster at elevated temperatures, as the equilibrium concentration of vacancies and their diffusivity increases with temperature [13]. However, the driving force for nucleation increases with higher supersaturation at lower temperatures [19]. This can be seen through Figure 7 wherein, for nucleation to proceed, an energy barrier ΔG^* must be overcome [19] as shown in Equation (3).

$$\exp\left(\frac{-\Delta G^*}{k_B T}\right) \tag{3}$$

This essentially implies that the probability of nucleation increases with a decrease in temperature.

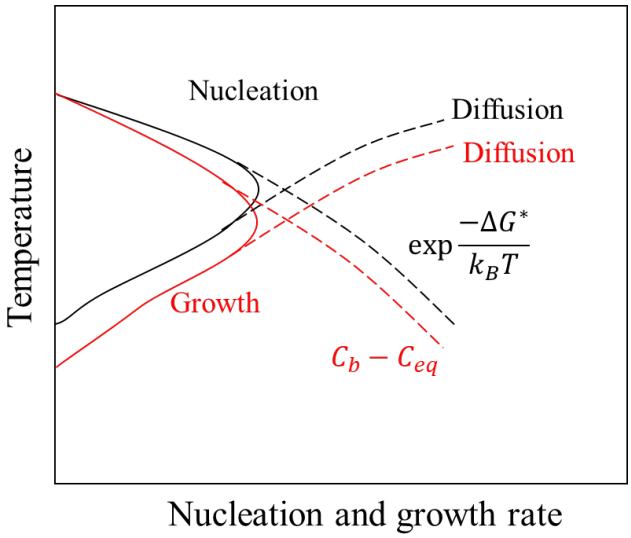

Figure 7. Schematic illustration of nucleation and growth rate of a secondary phase as a function of temperature. C_b is the bulk solute content and C_{eq} is the equilibrium solute content . k_B is the Boltzmann constant.

The growth rate of nucleated particles on the other hand, is diffusion controlled and increases with a rise in temperature as the vacancy concentration increases with higher temperature and accelerates solute transport. This indicates the combination of temperature and time for conventional precipitation aging to be a compromise between these two factors. This has prompted an increased interest in researchers to investigate and look for alternatives to break this compromise between thermodynamics and kinetics.

2.4.3 Previous investigations on dynamic precipitation

Plastic deformation modifies the precipitation behavior in multiple ways but in general mostly accelerates the kinetics as compared to static precipitation (in the absence of plastic deformation). Dynamic precipitation has been studied for aluminum alloys in tension [55, 56], fatigue [57-59] as well as high pressure torsion [60-62] before. Here, we focus on the microstructural changes during dynamic precipitation by plastic straining and fatigue/cyclic loading of Al alloys, since it is extremely relevant with the work done during this PhD.

When plastic straining is applied, several possible mechanisms can occur. For precipitates that have a significant misfit with the matrix, elastic stresses can have an effect on the precipitate nucleation as seen for an Al-Cu system [63]. An acceleration of nucleation is possible due to the presence of dislocations [64] or the growth and coarsening of precipitates is possible due to pipe diffusion [65]. Plastic deformation is known to change the equilibrium vacancy concentration, which could have an influence on the nucleation, growth as well coarsening mechanisms [66]. In other cases, a complete or partial dissolution of precipitates has been seen, due to shearing of precipitates by dislocations [56].

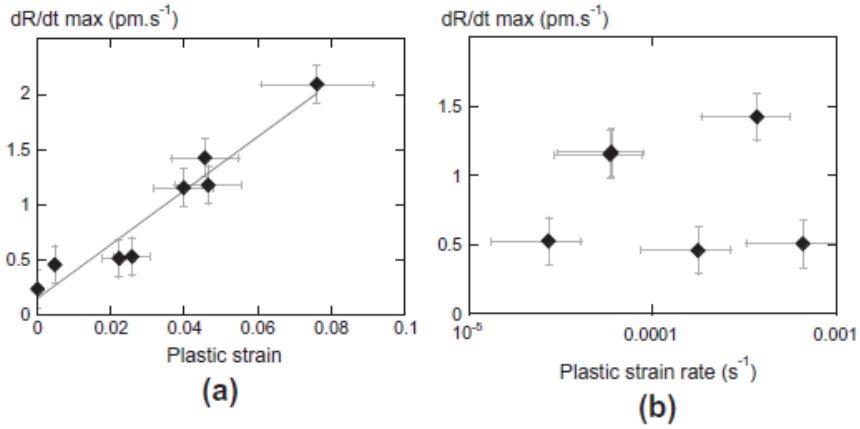

Figure 8. Maximum precipitate growth rate as a function of (a) plastic strain and (b) strain rate [9]. Reprinted, courtesy of Elsevier publishers.

The characteristics of the imposed strains (strain rate, strain or temperature) and the conditions used for precipitation (morphology of precipitates, SSSS and temperature) could possibly be

playing a part in dictating the dominating interaction phenomenon. Deschamps *et al.* [9] studied the effect of plastic straining (different strain rate and straining conditions) and observed an accelerated precipitate growth rate linearly with strain (Figure 8(a)) that reached a maximum at the end of the straining stage. The strain rate did not influence the precipitate growth rate as seen in Figure 8(b). The evolution of precipitate radius and volume fraction as function of strain and time shows the enhanced dynamic precipitation effect as opposed to conditions without deformation [64], as seen in Figure 8.

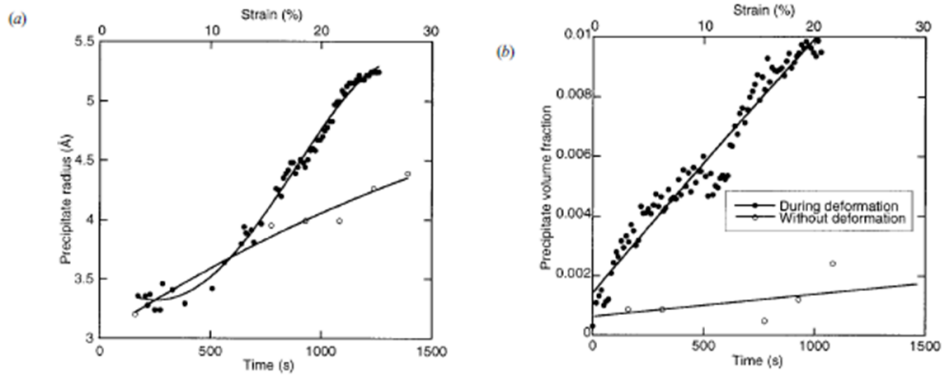

Figure 9. Evolution of (a) precipitate size and (b) volume fraction as a function of strain and time with and without deformation [64]. Reprinted by permission from Taylor and Francis publishers.

Cyclic deformation behavior of an Al-Zn-Mg(-Cu) alloy in an underaged and peak aged condition have been looked at to study the effect of cumulative strain, plastic strain amplitude and strain rate [58]. As seen in Figure 9(a), the hardening response is most pronounced for the underaged condition, while the 10 hours aged sample has a higher flow stress, and the hardening increment is not significant as compared to the other two. The size of GP zones formed, was constant, irrespective of applied strain rate, plastic strain amplitude and cumulative plastic strain. The volume fraction is constantly increasing while straining, suggesting the nucleation phenomenon to dominate during this time. The size of the GP zone evolution can be affected by diffusion-controlled growth, which ultimately increases the size of the particles. The other scenario could be the shearing of GP zones by dislocations, during which the size of the GP zones will decrease. Another possible effect of cyclic deformation could be the reversibility of the mobile dislocations. The overall size of GP zones remaining

constant throughout the cyclic tests suggests that it could possibly be a balance between the processes mentioned above.

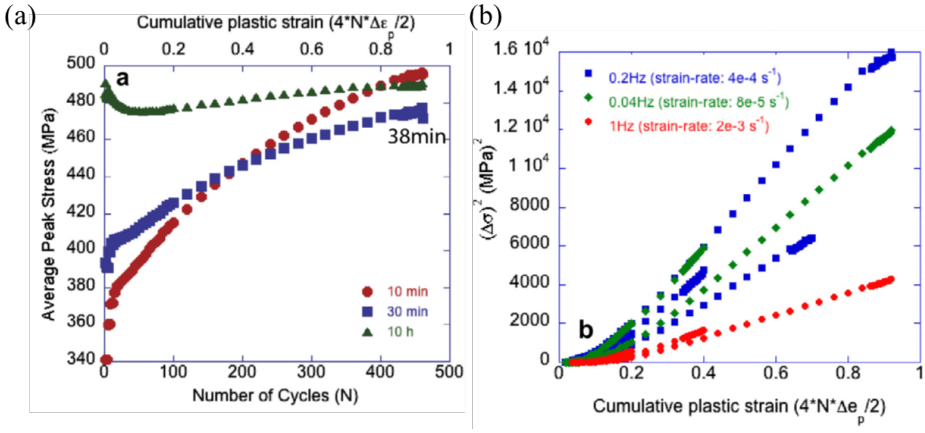

Figure 10. Average absolute values of tensile and compressive stresses for 10 min, 30 min and 10 h aged samples cyclically deformed at 0.2 Hz and plastic strain amplitude of 5 . 10^{-4} (b) square of average absolute values of cyclic hardening increment as a function of cumulative plastic strain for different number of cycles [58]. Reprinted by permission from Elsevier publishers.

Hutchinson *et al.*[58] found that the cumulative plastic strain as a function of the hardening increment was almost linear for all strain rates as seen in Figure 10(b) and since the size of dynamically formed GP zones remained constant, it was suggested that the nucleation rate is constant with respect to strain. The effect of change in plastic strain amplitude was found to be negligible during dynamic precipitation.

Sun *et al.* [13] proposed a novel method to generate excess vacancies using incremental cyclic loading. The mechanism is assumed to be the concept of dragging of jogs on dislocations, as discussed in section 2.4.1, which greatly increases the diffusivity of solute elements. The result of cyclic strengthening is a fine distribution of high number density of solute clusters at room temperature. Strength and uniform elongation equivalent or exceeding the PA condition with outstanding fatigue failure resistance were reported for Al-Cu, Al-Mg-Si and Al-Zn-Mg systems [67]. The large tensile elongations and thus high ductility, have been attributed to the homogenous distribution of solute clusters and the absence of precipitate free zones (PFZs)

[13, 68]. These PFZs are known to be soft regions devoid of a fine distribution of clusters, reducing the ductility severely.

Zhang *et al.* [69] observed an increase in yield strength without a decrease in the uniform elongation, due to a simultaneous increase in the strain hardening capability for long term NA of an Al-Zn-Mg alloy. This was attributed to the dramatic evolution of solute clusters during plastic straining, where the clusters show a dissolution to coarsening transition during deformation.

Chapter 3 Atom Probe Tomography

The work presented in this thesis is mainly experimental, and multiple techniques have been used to test and characterize the mechanical properties and microstructure. The characterizations to investigate the microstructure is done mainly using the APT in this thesis. Since the APT is used in all research papers presented in the latter sections, this chapter focuses on presenting APT reconstruction protocols used for the datasets studied. Particular attention on the determination of experimental conditions is highlighted to obtain useful and reproducible information from the atom probe data for 7xxx alloys. Different biasing phenomena or artifacts occur during APT evaporation process and when analyzing objects down to the nanometer scale like in the present case. A description on the different biasing that take place with respect to nanoparticles is given. Other experimental techniques used for complementary study is also summarized in the last part of the chapter.

3.1 Evaporation phenomenon- atom by atom

APT is one of the few characterization techniques that enable the investigation of matter down to the atomic scale. It is based on the principle of field evaporation of surface atoms of the sample being analyzed [70]. This enables the possibility to obtain the chemical nature of atoms evaporated by time-of-flight mass spectroscopy along with spatial resolution information based on a position sensitive detector. In order to evaporate atoms from a surface of a material that is 'n' times charged, it needs to overcome a barrier of Q_n as seen in Figure 11. This energy barrier is significantly high; however, it can strongly decrease in the presence of an electric field. A thermal activation or 'tunneling effect' enables the evaporation of ions and forms the principle of field evaporation., The frequency of atom evaporation in the case of thermal activation is described empirically by the Arrhenius law given as:

$$K = \nu \exp\left(\frac{-Q_n}{k_B T}\right) \tag{4}$$

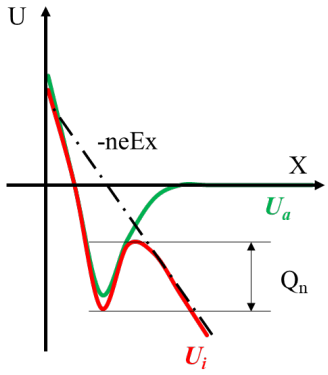

Figure 11. Schematic of atom and ion potential energy at surface during field evaporation. U_i and U_a are the potential energies of the ion and atom respectively and E is the electric field.

Where Q_n is the activation energy, v is the mean vibrational frequency of the surface atom and T is the sample temperature. The exponential variation of the frequency of evaporation with that of the reciprocal of applied temperature has been well established for a variety of materials experimentally [71].

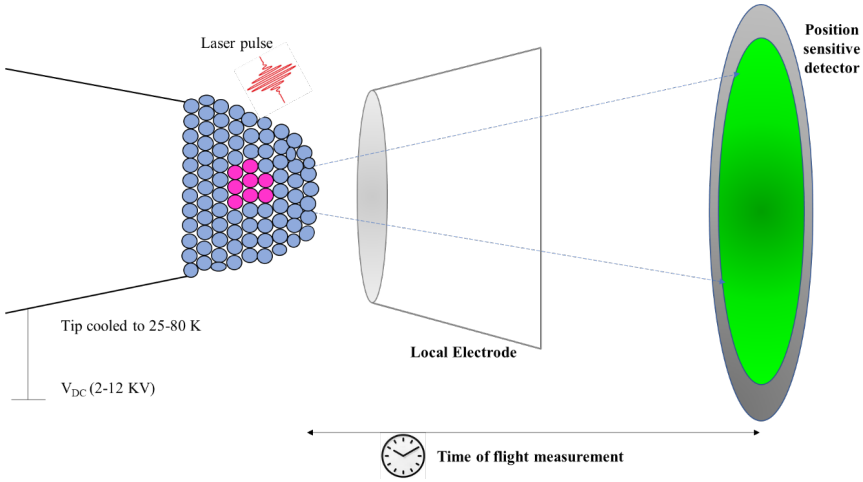

Figure 12. Schematic representation of the principal operation of an atom probe with a local electrode. Atoms are ionized with the electric or laser pulses and then can be accelerated towards a detector.

A typical APT sample consists of a sharp needle with a tip radius of 50-100 nm and is cooled down to temperatures between 25-80 K under high vacuum. A DC voltage in the range of 2-

12 kV is then applied to create a high electric field which allows controlled field evaporation of atoms layer by layer from the surface. The electric potential at the specimen surface is expressed by the relation

$$F = \frac{V}{k_F R} \tag{5}$$

Where F is the field required and V is the applied voltage to a specimen of radius R. However, as seen in Figure 12, the specimen is assumed to be a truncated cone with a quasi-hemispherical end cap whereas in real, the specimen is a sharp needle [72]. In this case, a small correction factor to the voltage/field relationship is used known as the field factor constant (k_F). Numerous numerical simulations show the dependency of it primarily on the shank angle of the truncated cone geometry of specimen [73].

The time of flight for each ion is recorded from the time of departure to it reaching the position sensitive detector to calculate its mass. Each chemical element has a unique time of flight which differentiates it from other elements. The initial position of the atom on the material surface can be inferred from the position it hits on the detector as shown in Figure 12.

As mentioned earlier, field evaporation can be induced thermally or electrically. In the case of voltage mode, the field at the tip of the specimen is increased above the threshold required for evaporation using a pulsed voltage. Thermal evaporation is achieved using laser power and was introduced by Kellogg and Tsong [74]. A thermal pulse using a laser increases the temperature at the tip above the threshold required for ion evaporation and can be followed through Figure 13.

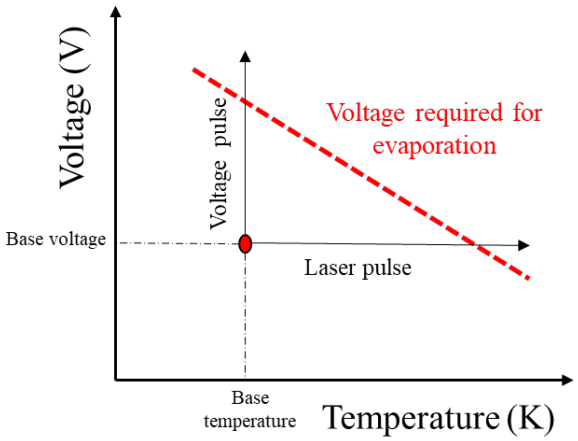

Figure 13. Schematic showing the effect of electric and laser pulsing on field evaporation.

Advantage of using laser mode for evaporation:

- The probability of premature specimen fracture reduces since less stress is being applied compared to voltage pulsing.
- Specimens with lower conductivity (semiconductors) can be analyzed.

Disadvantages of using laser power to evaporate are:

- Laser illumination is not uniform on the surface of the sample. This may cause evaporation from one side of the sample causing non-uniform end form and non-uniform field evaporation behavior.
- Loss in mass resolution for samples with low heat conducting capacity. Since the temperature of the specimen is increased, surface migration effect increases and the probability of multiple ions evaporating simultaneously also increases [75]. This leads to an overall decrease in the mass resolution.

The instrument used in this study is the ***LEAP 5000XS*** from CAMECA inc. The local electrode is introduced close to the specimen tip to enhance the electric field as shown in Figure 12 [76-78]. This also reduces the path over which the evaporated ions must be accelerated thus

improving the mass resolution. Overall, data acquisition rates are also increased as a result of reduced voltage required to create a sufficient field for evaporation.

3.2 Time of flight mass spectroscopy

When an atom is ionized, it possesses an initial potential energy given as

$$E_p = neV \tag{6}$$

Where n is the charge, e is the elementary charge of the electron ad V is the total voltage applied to the specimen. It is assumed that ions have no initial velocity and a constant velocity during flight such that the entire potential energy is converted into kinetic energy during flight given as:

$$E_k = \frac{1}{2}mv^2 \tag{7}$$

Where m is the mass of the ion and v is the velocity of the ion. Since it is assumed that the potential energy is fully converted into kinetic energy, Equations (6) and (7) can be combined to give a relation to obtain the mass to charge ratio (m/n) given as [79]

$$\frac{m}{n} = 2eV\frac{t_f^2}{L^2} \tag{8}$$

Where t_f is the time of flight and L is the flight length. Equation (8) implies that by knowing the time of flight it is possible to find the mass to charge ratio for each ion that has departed from the specimen and hit the detector. The typical detection efficiency (Q) for the LEAP 5000XS is 80%. This implies that 8 out of 10 evaporated ions are detected. The loss of ions is more random and not sensitive to any chemical element. The mass to charge ratio and hence the chemical identification of the detected ions are still obtained from equation (8).

A typical mass spectrum for Al-Zn-Mg(-Cu) system obtained during an APT analysis is shown in Figure 14(a). For each isotope of a particular chemical species, a characteristic peak is obtained. The indexing of these peaks allows for the identification of the elements present in the analyzed volume. The mass resolution of the spectrum shown in Figure 14(b) allows the distinction of the minority peak of 13Mg and the isotope of 13.5Al situated immediately after it. These are the second isotopes of $26Mg^{2+}$ and $27Al^{2+}$ respectively. If there is a significant

change in the isotope abundance, there is a possibility of another element contributing to that peak. However, we do not see such a case in the present material studied, hence will not be discussed further.

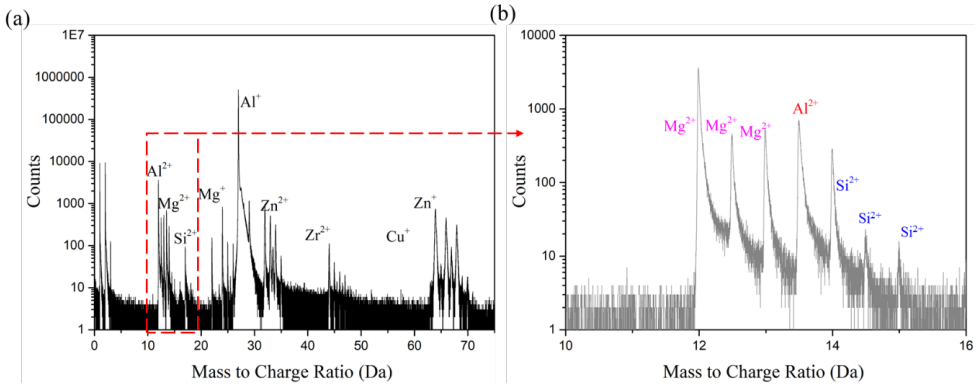

Figure 14. (a)Typical mass spectra obtained after evaporation of an Al-Zn-Mg(-Cu) alloy. (b) Peak identification for closely lying isotopes.

The concentration of each element is measured by the number of atoms contained in each peak. It is expressed in atomic percentage using equation (9)

$$C_i = \frac{N_i}{N_{total}} \tag{9}$$

Where N_i is the total number of atoms of species 'i' and N_{total} is the total number of atoms. The uncertainty is purely statistical and is given as the standard deviation:

$$\Delta C = 2\sqrt{\frac{C(1-C)}{N_{total}}} \tag{10}$$

Where C is the concentration of a specific species or element.

A higher mass resolution is crucial to deconstruct the isotopic recovery events but also to be able to separate two peaks in very close proximity to each other as seen in Figure 14. The analysis conditions like temperature, pulse fraction etc. influence the mass resolution and will be discussed in the later sections. These conditions must be optimized in advance for each material studied to accurately obtain a resolution in optimal mass.

3.3 Specimen preparation

To perform an APT experiment, a sharp needle must be fabricated form the bulk of the material. The two methods used to prepare samples are electropolishing [80-82] and focused ion beam milling techniques [83-87] and since both techniques are used to prepare samples in the present work, a brief description of them is given below.

3.3.1 Electropolishing

The shape of the needle to be fabricated requires a small cross-sectional blank of material to be cut from the bulk material. In the present case, match-stick shaped blanks of size 0.5 x 0.5 x 15 mm were cut along the extrusion direction of the material. Smaller the cross section, lesser will be the time taken for electropolishing. Ideally the cross section of the blank should be circular, and hence a mild grinding process is carried out after the cut. Due to their small size, the blanks are mounted onto Cu stubs and crimped for easy handling. Electropolishing is carried out in a two-step process. The first step involves passing the blank through a layer of electrolyte consisting of 25% perchloric acid and 75% acetic acid until a neck is formed and eventually breaks the blank into two parts. Voltages in the range of 15-22V is used during this step. The specimen is then moved through a counter electrode loop with a thin layer of electrolyte consisting of 2% perchloric acid and 98% 2-butoxyethanol. This is schematically shown through Figure 15 and is the final step of electropolishing rendering a sharp needle of 50-100 nm end radius. Lower voltages in the range of 4-7 V is used, since the needle is much thinner in this step, and an attempt is made to pass it through the micro loop many times to make the needle sharp enough. Specimens are finally cleaned with iso-propylene and stored in a vacuum desiccator to avoid further oxidation.

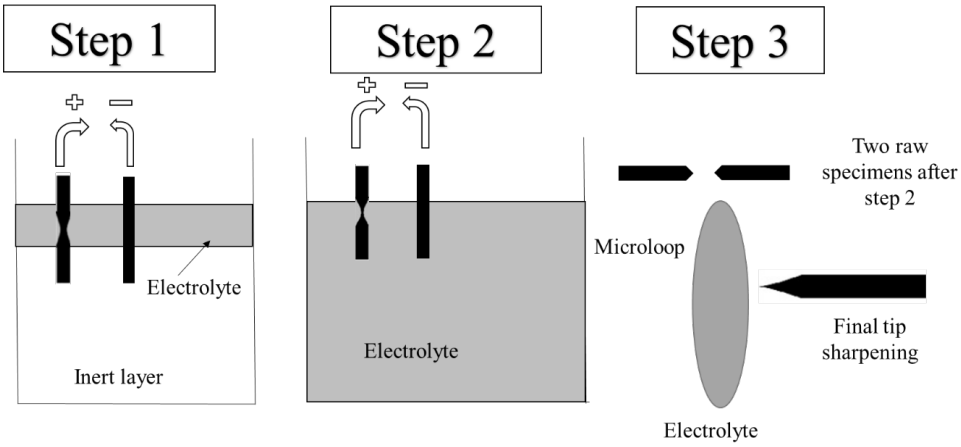

Figure 15. Schematic of the different steps in electropolishing for sample preparation of APT.

- *Challenges during electropolishing*

A high concentration of Cu is seen during the initial startup of the APT analysis. Famelton *et al.* [88] also observed a Cu enrichment layer during sample preparation. A similar phenomenon has been seen previously [89] on TEM sample preparation using electropolishing as well and is understood to be an influence of the electrolytic solution. Danoix et al.[90] also shows the presence of a Cu layer on electropolished Al systems previously. In our case, since Cu stubs were initially used to mount the blanks, a possible capillarity phenomenon could be occurring responsible for the Cu capping layer. Figure 16 shows the Cu enriched layer along with a 1D concentration profile highlighting the enrichment at the early stages of the analysis.

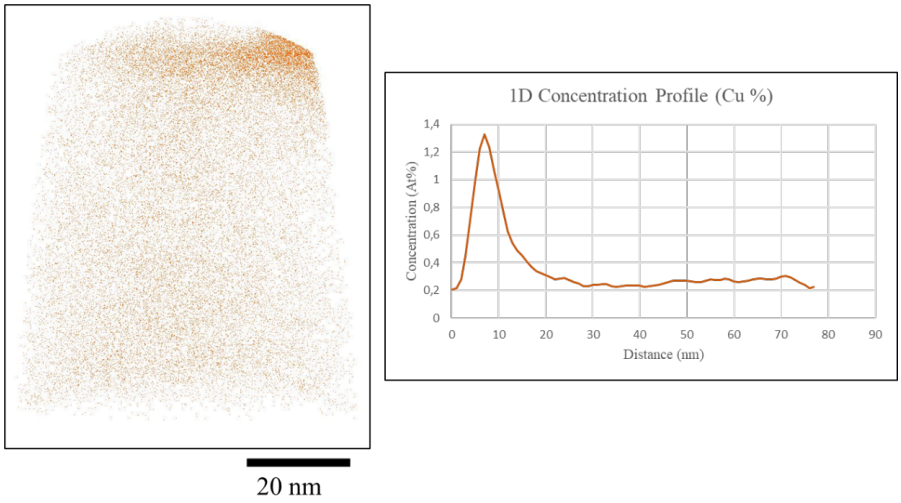

Figure 16. Cu capping layer on the tip of a 7046 alloy specimen analysed by APT and the corresponding 1D concentration profile along the evaporation direction to show the enrichment in Cu.

This is particularly challenging since the Cu seems to evaporate in bursts often prematurely fracturing the specimens. The evaporation of Cu in sudden bursts is mainly due to it being a high field element as compared to the matrix (Al) and is preferentially retained. A deeper explanation of this is given in the coming sections.

3.3.2 Focused ion beam (FIB) milling

Typically, for site specific samples, FIB is used to selectively cut out regions from the bulk of the sample and prepare needles. In the present study, cyclic aged samples needed to be probed, which had undergone significant mechanical damage and are brittle. The Cu capping layer from electropolishing also did not help as these samples were highly susceptible to fracture. With FIB prepared samples, the initial Cu capping layer was avoided and yielded high volume datasets.

The FEI Helios G2 dual beam instrument with a Ga^+ ion source was used to cut lamella of dimensions 3.5 x 25 x 3.5 µm by sputtering the surface with 30kV Ga ions. A protective layer of around 500 nm of platinum (Pt) is deposited to minimize the Ga implantation into the specimen. Silicon microtip coupons provided by Cameca Inc. were used to deposit the lamella.

The cut lamella was brought in contact with the top of the silicon post and welded on one side with Pt. The lamella was cut free, as seen in Figure 17 and the weld was strengthened by rotating the post by 180º (not shown in Figure 17). A sharp needle was then formed by annular milling of the lamella welded onto the post in steps. This was done in multiple steps with the steps summarized in Table 1. It is important to reduce the energy of Ga^+ ions to as low as possible in the final steps to prevent further implantation of Ga.

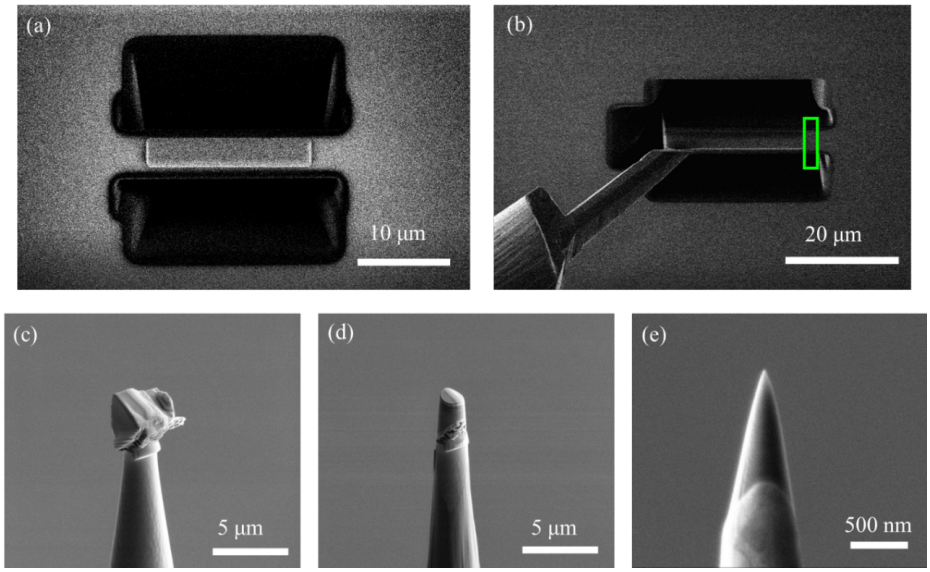

Figure 17. FIB specimen preparation involving (a) and (b) lamella preparation by depositing Pt, digging trenches and attaching the cantilever to the omni probe. (c) Deposition of a part of the lamella on the Si posts. (d) Milling of the deposited lamella in accordance with Table 1 and (e) showing the final tip.

Table 1. Recipe for sample preparation by FIB used for CA 7xxx alloys.

Inner Diameter (µm)	Outer Diameter (µm)	Ga^+ energy (kV)
1.6	5	30
0.8	4	16
0.5	4	8
0.3	2	2

The extent of the FIB induced damage region varies for different materials and is between 8-40 nm for most solid elements. During the implantation process, introduction of vacancies,

dislocation loops and self-interstitials takes place at the surface layer of the specimen [91-93]. It is also known to diffuse to the grain boundaries and dislocations in Al alloys [94-98]. An increase in the number density of clusters has been seen in Ga^+ and Xe^+ FIB sample preparation as compared to traditional electropolishing on Al alloys, although not very severe for Ga^+ [99]. A thin layer of Ga can be observed in the samples fabricated according to Table 1. This region is excluded from further data processing, as it is not representative of the true material being analyzed. To further reduce the influence of Ga, a control volume of set dimensions is used away from the crystallographic poles and Ga implanted regions to carry out cluster identification.

3.4 Reconstruction protocols

Multiple models have been developed to explain the image formation and projection of ions in field ion microscopy [100-103]. The reconstruction of datasets was done using based on the point projection model and is explained in detail elsewhere [104]. The x and y coordinates of each ion is calculated by back projection from the position of impact on the detector (X_d and Y_d) with the relation

$$x = \frac{X_d}{M} \text{ and } y = \frac{Y_d}{M} \tag{11}$$

Where M is the magnification which is strongly dependent on the shape of the specimen. The magnification is expressed as

$$M = \frac{L}{\xi \times R} \tag{12}$$

Where ξ is the image compression factor (ICF). It takes into account the fact that the magnification is slightly reduced due to the influence of the specimen shank and the effect it has on the trajectory of ions onto the detector.

The z coordinate is then determined based on the evaporation sequence of ions from the specimen tip. The relationship used to calculate the depth increment change is given as:

$$\Delta z = \frac{Q\, k_f^2\, F^2\, L^2}{\xi\, S_D\, M^2\, V^2} \tag{13}$$

Where S_D is the detector area. Hence, to create a 3D reconstruction of a dataset requires the knowledge of the above parameters.

3.4.1 ICF determination

As mentioned in the above section, the ICF directly relates the distribution of field and thus depends on the shape of the specimen. In such a case, the ICF affects the magnification of the image formed on the surface of the detector and is commonly seen in field ion microscpy (FIM) [104]. The orientation imaging microscopy (OIM) tool developed by EDAX AMETEK© is used in the state-of-the-art reconstruction software provided by CAMECA to help estimate the ICF as seen in Figure 18. Since the field desorption image contains crystallographic information of the specimen being analyzed, the angle between two crystallographic directions obtained on the detector is measured (θ_{obs}) and compared with the theoretical crystalline structure of the material (θ_{theo}) to obtain the ICF given as:

$$\xi = \frac{\theta_{obs}}{\theta_{theo}} \tag{14}$$

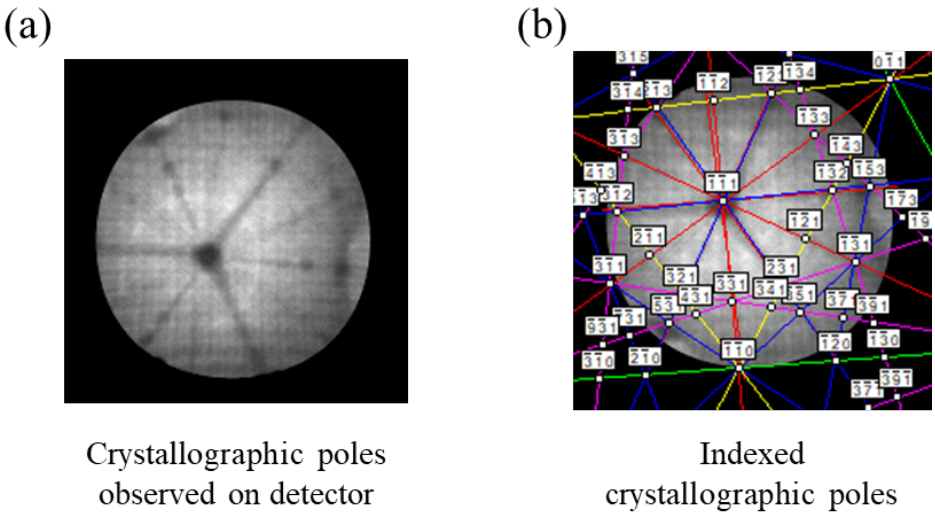

Figure 18.(a) Low density crystallographic pole regions observed on the detector during APT analysis. (b) Indexed crystallographic poles to measure the angle between specific crystallographic directions

Typically, the ICF varies between 1 and 2. A radial projection would correspond to an ICF of unity while the stereographic projection would account the ICF to be 2.

3.4.2 Field factor determination

In the case of Al alloys characterized in this study, the atomic volume of the atoms of the matrix as well as that of the particles is fixed at 0.0177 nm^3. This atomic volume corresponds to the average atomic volume of the analyzed volume with a lattice parameter 0.404 nm used to calculate the distance between successive planes as $\frac{0.404}{\sqrt{3}} = 0.233$ nm. As seen in Figure 18(a), the difference in density corresponds to the crystallographic pole (black dotted square) identified as one of the {111} planes from the stereographic projections of FCC using the OIM crystallography software.

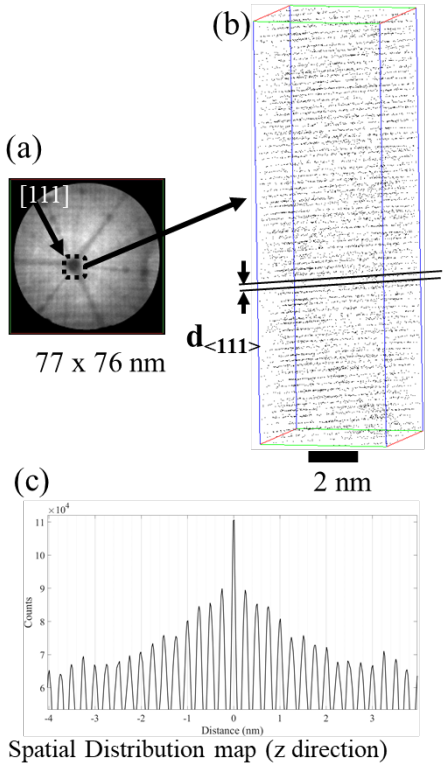

Figure 19. (a) Section of a reconstructed volume of an Al-Zn-Mg(-Cu) alloy showing atomic density variations corresponding to a crystallographic orientation identified from stereographic projection of an FCC cell. (b) Visualization of atomic planes {111} observed at the core of the crystallographic pole. (c) Spatial distribution map showing interplanar distance.

A section of the volume reconstructed is then extracted to observe the spatial distribution of the majority atoms (Al) as shown in Figure 19(b). The field factor is then adjusted so that the distance measured between two successive planes after reconstruction corresponds to the theoretical distance of the Al matrix ($d_{<111>}$ = 0.233 nm).

3.5 APT artefacts

It is very well established that the spatial resolution of the APT is controlled by the aberrations in the ion trajectories and was first observed in the FIM [105-109]. When the distribution of electric field close to the surface of the specimen being analyzed is non-uniform, there can be undesirable displacement (lateral) of the ions during the evaporation phenomenon. This leads to high- and low-density zones on the detector, which turn out to be high and low atomic density regions in the reconstruction like the poles and desorption lines. The electric field distribution around the poles tends to divert the trajectories of ions [110, 111].

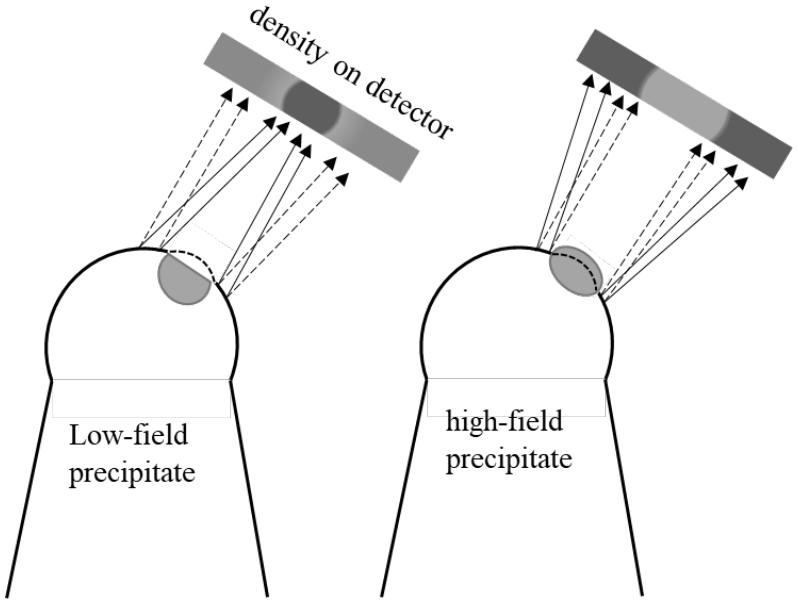

Figure 20. Density variations on the detector due to changes in surface curvature for low and high field precipitates. Dashed arrows show ideal trajectory path while the solid arrows show the trajectory aberrations.

Particles in the analyzed volume can also cause trajectory aberrations since particles require a different electric field for evaporation.

- If the electric field required to evaporate a particle is lower than that of the matrix, it causes a local flattening of the surface at the tip. This causes a lower field region as seen in Figure 20 and deflect the ions inwards causing an artificial increased density of atoms in the particle.
- If the electric field required to evaporate a particle is higher than that of the matrix, it causes an increase in the local curvature at the tip. This causes a higher field repelling the ions and an artificial decrease in the density of atoms in the particle is seen.

3.6 Analysis conditions

All APT analysis shown in this study have been carried out under laser pulses. They reduce the risk of rupture of fragile materials by avoiding electrical pulses which induce repeated mechanical stress on the sample[112, 113]. Laser pulses also help improve the mass resolution by reducing the energy spread. Optimization of parameters is also critical in order to obtain a high mass resolution with low background levels during the analysis. There are several parameters that can have an impact on the quality of an APT analysis. For instance, even the quality of vacuum maintained can have a significant role to play. In this section, brief explanation of the important parameter optimizations is mentioned.

3.6.1 Temperature

Adjustment to the base temperature is required for the stable imaging and optimal mass resolution. In general, for a majority of the alloys, a temperature in the range of 30-60 K is used, yielding high quality analysis without causing embrittlement of the specimen. This is common for very low temperatures and specimens more prone to fracture at low temperatures. Preferential evaporation is a common phenomenon observed if the optimized temperature range is not chosen. Typically, a lower temperature is used to yield a higher mass resolution. This is particularly important to resolve peaks situated very close to each other. Since not many fractures were observed at temperatures of 30K, all analysis in this work is fixed at 30K.

3.6.2 Pulse fraction

Phases with different evaporation fields can induce a preferential evaporation phenomenon if the voltage or laser pulses are not optimized. If the standing voltage (V_0) and pulsed voltage (V_T) are underestimated, it could possibly preferentially retain one of the species while an overestimation would cause preferential evaporation of the species. In order to avoid this, the optimal pulse fraction (f_p) is determined using the following relation:

$$f_p = \frac{V_T - V_0}{V_0} \tag{15}$$

This is done experimentally by first measuring the standing voltage (V_0) in kV for different laser energies *P* to obtain a fixed detection rate as shown in Figure 21(a). These points are fitted by a linear regression line as:

$$V_0 = k \text{ x } P + V_T \tag{16}$$

In one particular case shown in Figure 21(a), the standing voltage necessary to evaporate ions without laser energy is 5.28 kV and the coefficient k is -0.006 V pulse/nJ. These values can then be reintroduced in Equation (15) and (16) to express the equivalent pulse fraction (EPF) as:

$$f_p = \frac{-1}{1 + {}^{V_T}/_{k \text{ x } P}} \tag{17}$$

A plot of the EPF as a function of laser energy (Figure 21(b)) shows the laser energy required for a desired pulse fraction. In the example shown in Figure 21(b), it corresponds to a laser energy of 66 pJ/pulse for an equivalent pulse fraction close to 20%.

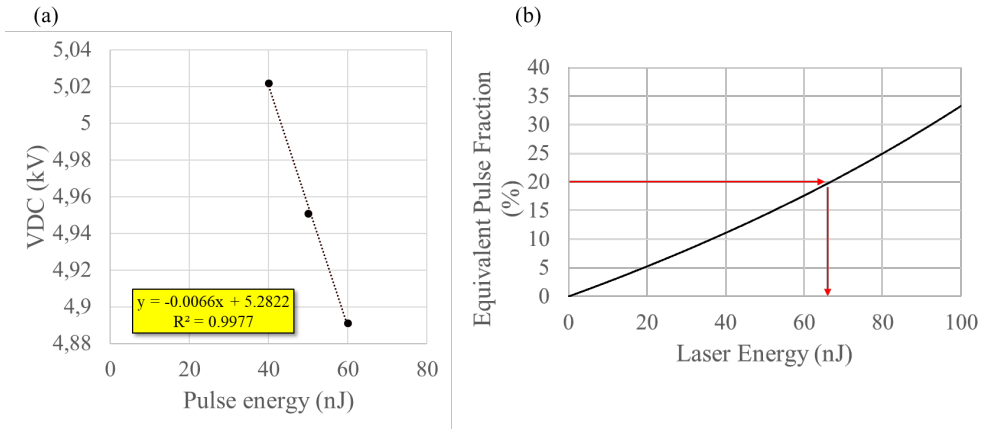

Figure 21. (a) Experimental data points fitted to obtain V_T and k for a 7003 alloy. (b) EPF curve showing the required laser energy for different pulse fractions.

An additional step to verify the process can be carried out. This involves setting a fixed laser energy to the one obtained above, and V_0 is adjusted to obtain the desired detection rate. Using Equation (15), the potential required to evaporate ions without the aid of laser energy is used to recalculate the EPF. This calculation step ensures the accuracy of the method and to have a real EPF estimated along with the one obtained from Figure 21(b).

3.7 Characterization of particles analyzed in Al-Zn-Mg(-Cu) alloys

As mentioned in the earlier sections, aging allows the strengthening of Al alloys by forming nano sized particles. These are chemical heterogeneities and can be identified by visual analysis in most cases after the APT analysis has been reconstructed. One of the aims of performing APT is to quantify the chemical heterogeneities formed after the early-stage aging and comparing different conditions. The easiest and most commonly used methodology is to use a concentration profile to measure local chemical fluctuations. It involves a 3D selection box positioned across the particle/volume to be examined. The volume is then divided into smaller sections (bins) normal to the z axis of the volume. The concentration of every element in that section is then calculated and represented in a graph, the concentration as a function of the distance. This method allows for individual examination of each particle and is used often in

this study to study the chemical fluctuations in the dataset. A more robust method is explained below for defining and characterizing the chemical heterogeneities.

3.7.1 Iso-concentration cluster identification method

The iso-concentration clustering algorithm is one of the fastest in terms of time computing. The dataset volume is divided into sub-volumes whose size can be adjusted. The atomic concentration of each species is then calculated for each of the sub-volumes ($C_i^x = {}^{N_i}/_{N}$) and a composition is assigned to the center of the sub-volume. However, this is not as straightforward since, at least it requires the consideration of compositions calculated for sub volumes in the vicinity of a particular element as shown in Figure 22(a). A gaussian weighting is applied, initially proposed by Hellman *et al.* [114, 115] to each atom to calculate the value of composition in each sub-volume. This principle is known as delocalization and the concentration of each atom within the sub-volume is the weighted average of the concentrations calculated with the neighboring sub-volumes. The weighted average is defined as the distance of the particular atom to the center of the sub-volume as shown in Figure 22(b).

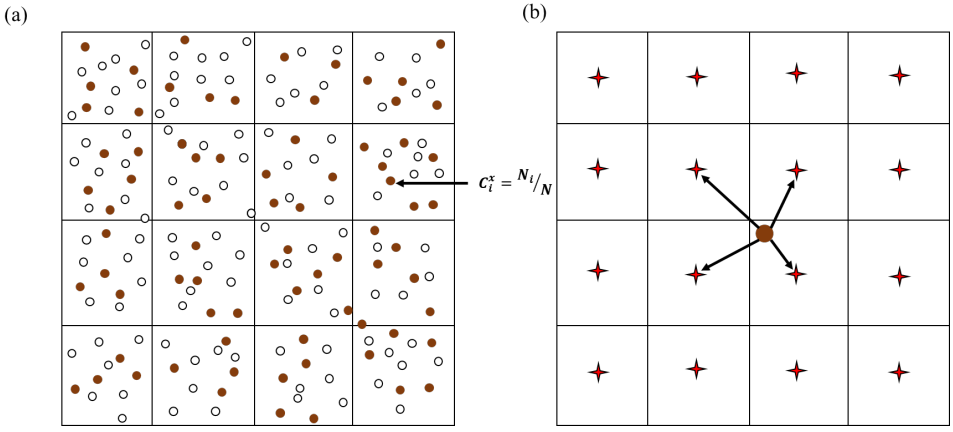

Figure 22. (a) Dividing the volume into smaller sub-volumes to calculate the concentrations. (b) Concentration calculation of each species based on its distance to neighboring sub-volumes.

If the concentration is higher than a chosen threshold, it forms a part of the particle, otherwise it is considered as a part of the matrix. The final step is to assign the atoms to a particle and is done based on the minimum size of the particle. If a particle is smaller than N_{min} number of

atoms, it again is considered a part of the matrix. The parameters chosen for the identification of particles in the 7xxx series is given in

Table 2. These parameters are accurate enough to identify a majority of the existing particles, however, very slight fluctuations or extremely small particles can be left out as matrix based on the parameters chosen and the sampling volume.

Table 2. Parameters for iso-concentration cluster identification in 7xxx Al alloy system.

Material	Elements chosen for cluster identification	Minimum threshold (at.%)
Al-Zn-Mg (7003)	Mg, Zn	10.2
Al-Zn-Mg(-Cu) (7046)	Mg,Zn	12.4

3.7.2 Determination of the number density

From the cluster identification explained in the above section, it is possible to measure the density of particles present in the APT dataset. Particles can either be present completely inside the dataset or on the edge. In the latter case, the entire volume of the particle is not present inside the volume and is accounted for as a half particle. The number density of particles (N_v) is calculated from the number of particles detected (N_p) and the total number of atoms contained in the analyzed volume, taking into account the detection efficiency (Q) and the average atomic volume [38]. The number density is thus given as:

$$N_v = \frac{N_p \text{ x } Q}{N_T \text{ x } V_{at}} \tag{18}$$

The uncertainty on the number density of particles is given by the relation:

$$\Delta N_v = \frac{N_v}{\sqrt{N_p}} \tag{19}$$

3.7.3 The Particle size

The size of a particle can be defined in a number of ways with the mean size and the size distributions the most important part of the information. With spherical particles, which is the

main type of particles studied in this thesis, the radius of gyration is the common measurement used. It is defined as:

$$R_g = \frac{\sum_{i=1}^{n}\{(x_i - x_0)^2 + (y_i - y_0)^2 + (z_i - z_0)^2\}}{N} \quad (20)$$

Where x_i, y_i and z_i are the coordinates of the i^{th} atom within the defined particle and N is the number of atoms in the particle. The radius of gyration cannot be directly compared with the size or radii measured in the TEM. However, the radius of gyration does help estimate the size distribution of a given system.

Typically, the radius of gyration is converted to the 'Guinier radius' as a more accurate representation of the size of the particles. However, the conversion factor used has no physical meaning as far as APT is concerned [116], coupled with trajectory aberrations complications was not the ideal way to define particles in this study.

Instead, the size of clusters was extracted from the $Extent_Z$ parameter (E_z) obtained from the cluster analysis. This parameter is defined as

$$E_z = \max |Z_{max} - Z_{min}| \quad (21)$$

Where Z_{max} and Z_{min} are the outermost atoms of the defined particle in the z-direction (projection direction). The z direction is chosen since it is the least biased direction in the APT [98].

Chapter 4 Summary and Outlook

This thesis is broken down into four journal articles prepared along with corresponding supplementary information, which provide the main investigations and findings of this PhD. The effect of cyclic aging has been investigated on two Al-Zn-Mg(-Cu) alloys to study the response on mechanical properties. This has been used to correlate with the microstructure investigated by advanced characterization tools such as APT and TEM. Cluster identification using a parameter dependent, and a parameter independent methodology has been applied to efficiently characterize the metallurgical information such as size of precipitates, composition, number density and solute ratio in particles. Additionally, the precipitate sequence in an Al-Zn-Mg alloy has been investigated to understand the nucleation of the main hardening phase in such an alloy. This chapter includes the main results and conclusions of the work followed by suggestions for future work.

4.1 Summary

CA on two different 7xxx alloys, one containing Cu (7046) and one being Cu free (7003), have been investigated. The cyclic aging was performed in stress-controlled mode, where the initial stress applied was close to the YS of the AQ state of the alloys. The targeted stress chosen was close to 70% of the maximum strength of the alloys in PA condition. CA and a further 10 days of NA exhibited strength and uniform elongations similar and slightly higher than that of the PA condition. This is attributed to a uniform distribution of fine solute clusters enriched in Mg and Zn. The fracture mode of the CA samples, however, was in shear without prior necking. In all cases, this started at around maximum strength, similar as the onset of necking as predicted by Considere criterion and are called slant fractures in this study. An aging treatment similar to the PA treatment was carried out after the CA. This restored the post necking ductility, indicating that possible damage caused by the CA did not influence the fracture mode. Instead, the precipitate type and the symmetry of the plate material used in this study could be

precursors for such fracture modes, which has otherwise not been observed in axisymmetric materials.

Detailed microstructural investigations of the alloys revealed that the early-stage clusters formed during and after CA had similar chemistry and structure to that of the conventional GP zones formed during NA and AA up to a certain temperature. Storage of CA samples for 10 days is found to be very important for obtaining higher strength, since these GP zones then grow further by utilizing the solute from the matrix. The number density of clusters formed in the 7046 alloy is consistently slightly lower than that of the 7003 alloy, while a similar trend is seen for the size measurements. The Cu containing clusters in the 7046 alloy, with a different Zn/Mg ratio to that of the 7003 alloy must be acting as stronger obstacles for dislocation glide.

Cluster identification by IPM and PCF methodologies for experimental datasets of 7003 and 7046 consisting of early-stage clusters have been performed to test the robustness of both methodologies. The PCF methodology helps extract an average value for different metallurgical information, such as size, composition, and volume fraction, while the IPM helps extract similar information cluster by cluster. A good agreement is seen by both methodologies in quantifying the clusters of both alloys; 7003 having slightly larger clusters than the 7046 alloy. Chemical compositions of clusters are quite similar for both alloys (GPI zones) with an average Zn/Mg ratio of around 2 for the 7003 alloy and 1.5 for the 7046 alloy. Furthermore, atom probe volumes have been simulated with predefined composition and volume fraction,. This is used to assess the sensitivity of different methods (PCF and IPM) on particle quantification. An additional parameter, the resolution of the atom probe has also been used to study its effect on accurate quantification of particles. Resolution and average size of particles play an important role in detecting them and hence quantification depends on it.

To study the evolution of precipitates and revisit the precipitation sequence in Al-Zn-Mg alloys, the 7003 alloys that has been NA for 1 year is subjected to AA at 140ºC. The NA condition has a dense population of GPI zones along with a small fraction of η’ precipitates. A 10-minute AA treatment at 140ºC saw the hardness decrease from 121 HV to 88 HV. The number densities for the two conditions were similar, however, the Zn/Mg ratio decreased from 2 to 1.7 during the 10 minutes of AA and the solute level in the matrix slightly increased. The

solute clusters no longer showed the GPI atomic structure. The peak in hardness was reached after 5 hours of AA at 140ºC. This condition was dominated by η' in combination with η_1, η_2 and T' phases seen by scanning transmission electron microscopy.

4.2 Outlook

The alloys investigated in this work are extruded plates of 7003 and 7046 alloys. A similar study on axisymmetric 6082 system has shown lower cumulative plastic strains as compared to the flat plate extruded alloys, and also with conventional necking behavior. Indications of symmetry breaking perturbations in the extruded alloys with orthotropic symmetry is seen as a possible triggering factor for early slant fractures. However, this hypothesis needs to be tested for the 7xxx system. Hence, axisymmetric processed alloys should be tested in future to see if they have slant fracture or necking.

The potential of CA on inducing precipitation in the heat treatable alloys has been promising and can be explored further moving ahead. This methodology can be tested in particular to the non-heat treatable alloys, such as the 3xxx and 5xxx alloys to study the effect of CA on strength and ductility.

CA has shown promise in the rapid hardening response but has constraints in specimen geometry to implement both tension and compression part of the test. However, there is potential for different process innovations to carry out other ways to keep on deforming plastically without too large geometry change in order to implement such a methodology in industrial use. A possible tension and retraction to zero load can be tried for large sheets where the compression part of the test would give buckling.

References

1. Polmear, I., et al., *Light alloys: metallurgy of the light metals*. 2017: Butterworth-Heinemann.
2. Embury, J., D. Lloyd, and T. Ramachandran, *Strengthening mechanisms in aluminum alloys*, in *Treatise on Materials Science & Technology*. 1989, Elsevier. p. 579-601.
3. Shao, D., et al., *Effect of Pre-strain on the Solute Clustering, Mechanical Properties, and Work-Hardening of a Naturally Aged Al-Cu-Mg Alloy.* Metallurgical and Materials Transactions A, 2017. **48**(9): p. 4121-4134.
4. Marceau, R.K., et al., *Solute clustering in Al–Cu–Mg alloys during the early stages of elevated temperature ageing.* Acta Materialia, 2010. **58**(15): p. 4923-4939.
5. Marceau, R.K., et al., *Analysis of strengthening in AA6111 during the early stages of aging: Atom probe tomography and yield stress modelling.* Acta Materialia, 2013. **61**(19): p. 7285-7303.
6. De Geuser, F., W. Lefebvre, and D. Blavette, *3D atom probe study of solute atoms clustering during natural ageing and pre-ageing of an Al-Mg-Si alloy.* Philosophical Magazine Letters, 2006. **86**(04): p. 227-234.
7. Werinos, M., et al., *Design strategy for controlled natural aging in Al–Mg–Si alloys.* Acta Materialia, 2016. **118**: p. 296-305.
8. Deschamps, A., et al., *Low-temperature dynamic precipitation in a supersaturated AI-Zn-Mg alloy and related strain hardening.* Philosophical Magazine A, 1999. **79**(10): p. 2485-2504.
9. Deschamps, A., et al., *In situ evaluation of dynamic precipitation during plastic straining of an Al–Zn–Mg–Cu alloy.* Acta materialia, 2012. **60**(5): p. 1905-1916.
10. Ghaferi, M., et al., *Evaluation of different heat treatment cycles on improving single point incremental forming of AA6061 aluminum alloy.* The International Journal of Advanced Manufacturing Technology, 2019. **105**(1): p. 83-100.

References

11. Wolverton, C., *Solute–vacancy binding in aluminum.* Acta Materialia, 2007. **55**(17): p. 5867-5872.
12. Kubota, M., J.F. Nie, and B.C. Muddle, *Characterisation of precipitation hardening response and as-quenched microstructures in Al-Mg (-Ag) alloys.* Materials transactions, 2004. **45**(12): p. 3256-3263.
13. Sun, W., et al., *Precipitation strengthening of aluminum alloys by room-temperature cyclic plasticity.* Science, 2019. **363**(6430): p. 972-975.
14. Vurpillot, F. and C. Oberdorfer, *Modeling atom probe tomography: A review.* Ultramicroscopy, 2015. **159**: p. 202-216.
15. De Geuser, F. and B. Gault, *Metrology of small particles and solute clusters by atom probe tomography.* Acta Materialia, 2020. **188**: p. 406-415.
16. Stephenson, L.T., et al., *New techniques for the analysis of fine-scaled clustering phenomena within atom probe tomography (APT) data.* Microscopy and Microanalysis, 2007. **13**(6): p. 448-463.
17. Verhoeven, J.D., *Fundamentals of physical metallurgy*. 1975: John Wiley & Sons Incorporated.
18. Zhao, H., et al., *Parameter free quantitative analysis of atom probe data by correlation functions: Application to the precipitation in Al-Zn-Mg-Cu.* Scripta Materialia, 2018. **154**: p. 106-110.
19. Porter, D.A. and K.E. Easterling, *Phase transformations in metals and alloys (revised reprint)*. 2009: CRC press.
20. Kocks, U.F., et al., *Thermodynamics and kinetics of slip.* 1975.
21. Peng, J., et al., *Solute-vacancy clustering in aluminum.* Acta Materialia, 2020. **196**: p. 747-758.
22. Starink, M. and S. Wang, *The thermodynamics of and strengthening due to co-clusters: general theory and application to the case of Al–Cu–Mg alloys.* Acta Materialia, 2009. **57**(8): p. 2376-2389.
23. Pogatscher, S., et al., *Mechanisms controlling the artificial aging of Al–Mg–Si Alloys.* Acta Materialia, 2011. **59**(9): p. 3352-3363.

References

24. Clouet, E., et al., *Precipitation kinetics of Al3Zr and Al3Sc in aluminum alloys modeled with cluster dynamics.* Acta Materialia, 2005. **53**(8): p. 2313-2325.
25. Degischer, H.P., et al., *Decomposition processes in an Al-5% Zn-1% Mg alloy.* International Journal of Materials Research, 1980. **71**(4): p. 231-238.
26. Thackery, P., *THE NATURE AND MORPHOLOGY OF PRECIPITATE IN ALUMINIUM-ZINC-MAGNESIUM ALLOYS.* J Inst Metals, 1968. **96**(8): p. 228-235.
27. Embury, J. and R. Nicholson, *The nucleation of precipitates: the system Al-Zn-Mg.* Acta Metallurgica, 1965. **13**(4): p. 403-417.
28. Schmalzried, H. and V. Gerold, *X-ray investigation of the age hardening of an aluminum-magnesium-zinc alloy.* Z. Metallk., 1958. **49**.
29. Asano, K. and K.-I. Hirano, *Precipitation Process in an Al–Zn–Mg Alloy.* Transactions of the Japan Institute of Metals, 1968. **9**(1): p. 24-34.
30. Löffler, H., I. Kovács, and J. Lendvai, *Decomposition processes in Al-Zn-Mg alloys.* Journal of Materials Science, 1983. **18**(8): p. 2215-2240.
31. Thomas, G. and J. Nutting, *The ageing characteristics of aluminum alloys.* Journal of the Institute of Metals, 1959. **88**: p. 81-90.
32. Juhász, A., et al., *Mechanical properties of Al-Zn-Mg alloys investigated by microhardness measurements.* Journal of Materials Science, 1981. **16**(2): p. 367-372.
33. Ungar, T., et al., *The decomposition of the solid solution state in the temperature range 20 to 200° C in an Al-Zn-Mg alloy.* Journal of Materials Science, 1979. **14**(3): p. 671-679.
34. Lacom, W., et al., *Decomposition Processes in an Al-5% Zn-1% Mg Alloy.* International Journal of Materials Research, 1982. **73**(12): p. 781-785.
35. Huang, Z., et al., *The mechanism of nucleation and precipitation in 7075-0.7 Li alloy.* Acta metallurgica et materialia, 1994. **42**(2): p. 549-559.
36. Lervik, A., et al., *Atomic structure of solute clusters in Al–Zn–Mg alloys.* Acta Materialia, 2021. **205**: p. 116574.
37. Cornish, A. and M. Day, *PRECIPITATION IN THE MEIGHBOURHOOD OF GRAIN BOUNDARIES IN AN ALUMINIUM-ZINC-MAGNESIUM ALLOY.* J Inst Metals, 1969. **97**(2): p. 44-52.

References

38. Kovács, Z., et al. *The effect of Cu on precipitation in Al-Zn-Mg alloys*. in *Materials Forum*. 2004.
39. Berg, L., et al., *GP-zones in Al–Zn–Mg alloys and their role in artificial aging.* Acta materialia, 2001. **49**(17): p. 3443-3451.
40. Chinh, N., et al., *The effect of Cu on mechanical and precipitation properties of Al–Zn–Mg alloys.* Journal of Alloys and Compounds, 2004. **378**(1-2): p. 52-60.
41. Shah, S., et al., *Effect of cyclic ageing on the early-stage clustering in Al–Zn–Mg (-Cu) alloys.* Materials Science and Engineering: A, 2022: p. 143280.
42. Shah, S., et al., *Precipitation, mechanical properties and early slant ductile fracture in cyclic and naturally aged Al-Zn-Mg (-Cu) alloys.* Materials & Design, 2022. **222**: p. 111026.
43. Fang, X., et al., *Effects of Cu content on the precipitation process of Al–Zn–Mg alloys.* Journal of Materials Science, 2012. **47**(23): p. 8174-8187.
44. Lorimer, G. and R. Nicholson, *Further results on the nucleation of precipitates in the Al□Zn□Mg system.* Acta Metallurgica, 1966. **14**(8): p. 1009-1013.
45. Radomsky, M., et al., *On the decomposition behaviour of Al-4.5 at% Zn-2 to 3 at% Mg alloys during continuous heating.* Journal of Materials Science, 1979. **14**(12): p. 2906-2912.
46. Li, X., et al., *HREM study and structure modeling of the η′ phase, the hardening precipitates in commercial Al–Zn–Mg alloys.* Acta materialia, 1999. **47**(9): p. 2651-2659.
47. Marioara, C.D., et al., *Atomic structure of hardening precipitates in an Al–Mg–Zn–Cu alloy determined by HAADF-STEM and first-principles calculations: relation to η-MgZn2.* Journal of Materials Science, 2013. **48**(10): p. 3638-3651.
48. Mondolfo, L., N. Gjostein, and D. Levinson, *Structural changes during the aging in an Al-Mg-Zn alloy.* JOM, 1956. **8**(10): p. 1378-1385.
49. Lorimer, G. and R. Nicholson, *The mechanism of phase transformations in crystalline solids.* Institute of Metals, 1969. **1**.
50. Hirano, K.-I., R. Agarwala, and M. Cohen, *Diffusion of iron, nickel and cobalt in aluminum.* Acta Metallurgica, 1962. **10**(9): p. 857-863.

References

51. Lendvai, J. *Precipitation and strengthening in aluminium alloys*. in *Materials Science Forum*. 1996. Trans Tech Publ.
52. Maloney, S., et al., *The chemistry of precipitates in an aged Al-2.1 Zn-1.7 Mg at.% alloy.* Scripta Materialia, 1999. **41**(10).
53. Marlaud, T., et al., *Influence of alloy composition and heat treatment on precipitate composition in Al–Zn–Mg–Cu alloys.* Acta Materialia, 2010. **58**(1): p. 248-260.
54. Dieter, G.E. and D. Bacon, *Mechanical metallurgy*. Vol. 3. 1976: McGraw-hill New York.
55. Liu, C.-Y., et al., *Static and Dynamic Precipitation Behavior of the Al–20wt.% Zn Alloy.* Chinese Physics Letters, 2016. **33**(5): p. 056101.
56. Hutchinson, C., et al., *Quantifying the strain-induced dissolution of precipitates in Al alloy microstructures using nuclear magnetic resonance.* Acta materialia, 2009. **57**(19): p. 5645-5653.
57. Hörnqvist, M. and B. Karlsson, *Dynamic strain ageing and dynamic precipitation in AA7030 during cyclic deformation.* Procedia Engineering, 2010. **2**(1): p. 265-273.
58. Hutchinson, C., et al., *Quantitative measurements of dynamic precipitation during fatigue of an Al–Zn–Mg–(Cu) alloy using small-angle X-ray scattering.* Acta materialia, 2014. **74**: p. 96-109.
59. Hutchinson, C., F.d. Geuser, and A. Deschamps, *Dynamic room temperature precipitation during cyclic deformation of an Al-Zn-Mg-Cu alloy*, in *ICAA13 Pittsburgh*. 2012, Springer. p. 1101-1106.
60. Zhang, Y., et al., *Dynamic precipitation, segregation and strengthening of an Al-Zn-Mg-Cu alloy (AA7075) processed by high-pressure torsion.* Acta Materialia, 2019. **162**: p. 19-32.
61. Liu, Z., et al., *On strain-induced dissolution of θ' and θ particles in Al–Cu binary alloy during equal channel angular pressing.* Materials Science and Engineering: A, 2011. **528**(6): p. 2217-2222.
62. Liu, M., et al., *Analysis on the dissolution behavior of various size Cu-Mg co-clusters near a fatigue crack tip of underaged Al-Cu-Mg alloy during cyclic loading.* Journal of Alloys and Compounds, 2017. **699**: p. 119-125.

References

63. Zhu, A., J. Chen, and E. Starke Jr, *Precipitation strengthening of stress-aged Al–xCu alloys.* Acta materialia, 2000. **48**(9): p. 2239-2246.
64. Deschamps, A., et al., *In-situ small-angle X-ray scattering study of dynamic precipitation in an Al-Zn-Mg-Cu alloy.* Philosophical Magazine, 2003. **83**(6): p. 677-692.
65. Pink, E. and W. Webernig, *Precipitation during serrated flow in AlZn5Mg1.* Acta Metallurgica, 1987. **35**(1): p. 127-132.
66. Han, W., et al., *Dynamic precipitation during cyclic deformation of an underaged Al–Cu alloy.* Materials Science and Engineering: A, 2011. **528**(24): p. 7410-7416.
67. Zhang, Q., et al., *Training high-strength aluminum alloys to withstand fatigue.* Nature communications, 2020. **11**(1): p. 1-8.
68. Chen, Z., et al., *Enhanced strength-plasticity combination in an Al–Cu–Mg alloy—— atomic scale microstructure regulation and strengthening mechanisms.* Materials Science and Engineering: A, 2020. **787**: p. 139447.
69. Zhang, P., et al., *Solute cluster evolution during deformation and high strain hardening capability in naturally aged Al–Zn–Mg alloy.* Acta Materialia, 2021. **207**: p. 116682.
70. Müller, E.W., *Field ionization and field ion microscopy*, in *Advances in electronics and electron physics*. 1960, Elsevier. p. 83-179.
71. Lefebvre, W., F. Vurpillot, and X. Sauvage, *Atom probe tomography: put theory into practice*. 2016: Academic Press.
72. Vella, A., *On the interaction of an ultra-fast laser with a nanometric tip by laser assisted atom probe tomography: A review.* Ultramicroscopy, 2013. **132**: p. 5-18.
73. Gomer, R. and R. Gomer, *Field emission and field ionization*. Vol. 34. 1961: Springer.
74. Kellogg, G. and T. Tsong, *Pulsed-laser atom-probe field-ion microscopy.* Journal of Applied physics, 1980. **51**(2): p. 1184-1193.
75. Ehrlich, G., *Direct observation of individual atoms on metals.* Surface Science, 1977. **63**: p. 422-447.

References

76. Smith, R. and J. Walls, *Ion trajectories in the field-ion microscope.* Journal of Physics D: Applied Physics, 1978. **11**(4): p. 409.
77. Huang, M., et al., *Measurements of field enhancement introduced by a local electrode.* Ultramicroscopy, 2001. **89**(1-3): p. 163-167.
78. Kelly, T.F., et al., *On the many advantages of local-electrode atom probes.* Ultramicroscopy, 1996. **62**(1-2): p. 29-42.
79. Blavette, D., et al., *An atom probe for three-dimensional tomography.* Nature, 1993. **363**(6428): p. 432-435.
80. Krakauer, B., et al., *A system for systematically preparing atom-probe field-ion-microscope specimens for the study of internal interfaces.* Review of scientific instruments, 1990. **61**(11): p. 3390-3398.
81. Melmed, A.J., *The art and science and other aspects of making sharp tips.* Journal of Vacuum Science & Technology B: Microelectronics and Nanometer Structures Processing, Measurement, and Phenomena, 1991. **9**(2): p. 601-608.
82. EW, M., *uller, TT Tsong, Field Ion Microscopy, Principles and Applications*. 1969, Elsevier, New York.
83. Giannuzzi, L.A., *Introduction to focused ion beams: instrumentation, theory, techniques and practice*. 2004: Springer Science & Business Media.
84. Larson, D., et al., *Field-ion specimen preparation using focused ion-beam milling.* Ultramicroscopy, 1999. **79**(1-4): p. 287-293.
85. Larson, D., et al. *Toward atom probe tomography of microelectronic devices*. in *Journal of Physics: Conference Series*. 2011. IOP Publishing.
86. Saxey, D., et al., *Atom probe specimen fabrication methods using a dual FIB/SEM.* Ultramicroscopy, 2007. **107**(9): p. 756-760.
87. Miller, M.K. and K.F. Russell, *Atom probe specimen preparation with a dual beam SEM/FIB miller.* Ultramicroscopy, 2007. **107**(9): p. 761-766.
88. Famelton, J., et al., *Xenon plasma focussed ion beam preparation of an Al-6XXX alloy sample for atom probe tomography including analysis of an α-Al (Fe, Mn) Si dispersoid.* Materials Characterization, 2021. **178**: p. 111194.

References

89. Wenner, S., et al., *Copper enrichment on aluminium surfaces after electropolishing and its effect on electron imaging and diffraction.* Materials Characterization, 2021. **172**: p. 110846.
90. Danoix, F., M. Miller, and A. Bigot, *Analysis conditions of an industrial Al–Mg–Si alloy by conventional and 3D atom probes.* Ultramicroscopy, 2001. **89**(1-3): p. 177-188.
91. Shim, S., et al., *Effects of focused ion beam milling on the compressive behavior of directionally solidified micropillars and the nanoindentation response of an electropolished surface.* Acta Materialia, 2009. **57**(2): p. 503-510.
92. Bei, H., et al., *Effects of focused ion beam milling on the nanomechanical behavior of a molybdenum-alloy single crystal.* Applied Physics Letters, 2007. **91**(11): p. 111915.
93. Tsai, W., et al., *Grain boundary imaging, gallium diffusion and the fracture behavior of Al–Zn Alloy–An in situ study.* Nuclear Instruments and Methods in Physics Research Section B: Beam Interactions with Materials and Atoms, 2003. **199**: p. 457-463.
94. Thompson, K., et al., *Minimization of Ga induced FIB damage using low energy clean-up.* Microscopy and Microanalysis, 2006. **12**(S02): p. 1736-1737.
95. Miller, M.K. and R.G. Forbes, *The art of specimen preparation*, in *Atom-Probe Tomography*. 2014, Springer. p. 189-228.
96. Vigilante, G.N., E. TROlANO, and C. Mossey, *Liquid Metal Embrittlement of ASTM A723 Gun Steel by Indium and Gallium*. 1999, ARMY ARMAMENT RESEARCH DEVELOPMENT AND ENGINEERING CENTER WATERVLIET NY ….
97. Kolman, D. and R. Chavarria, *Liquid-metal embrittlement of type 316L stainless steel by gallium as measured by elastic-plastic fracture mechanics.* Corrosion, 2004. **60**(03).
98. Gault, B., et al., *Atom probe crystallography.* Materials Today, 2012. **15**(9): p. 378-386.
99. Tweddle, D., et al., *Direct Observation of PFIB-Induced Clustering in Precipitation-Strengthened Al Alloys by Atom Probe Tomography.* Microscopy and Microanalysis, 2022: p. 1-6.

References

100. Brandon, D., *The accurate determination of crystal orientation from field ion micrographs.* Journal of Scientific Instruments, 1964. **41**(6): p. 373.
101. Walls, J. and H. Southworth, *Magnification in the field-ion microscope.* Journal of Physics D: Applied Physics, 1979. **12**(5): p. 657.
102. Wilkes, T., G. Smith, and D. Smith, *On the quantitative analysis of field-ion micrographs.* Metallography, 1974. **7**(5): p. 403-430.
103. Southworth, H. and J. Walls, *The projection geometry of the field-ion image.* Surface Science, 1978. **75**(1): p. 129-140.
104. Gault, B., et al., *Atom probe microscopy*. Vol. 160. 2012: Springer Science & Business Media.
105. Miller, M.K., et al., *Atom probe field ion microscopy.* 1996.
106. Waugh, A., E. Boyes, and M. Southon, *Investigations of field evaporation with a field-desorption microscope.* Surface Science, 1976. **61**(1): p. 109-142.
107. Vurpillot, F., A. Bostel, and D. Blavette, *Trajectory overlaps and local magnification in three-dimensional atom probe.* Applied Physics Letters, 2000. **76**(21): p. 3127-3129.
108. Marquis, E.A. and F. Vurpillot, *Chromatic aberrations in the field evaporation behavior of small precipitates.* Microscopy and microanalysis, 2008. **14**(6): p. 561-570.
109. Vurpillot, F., et al., *Modeling image distortions in 3DAP.* Microscopy and Microanalysis, 2004. **10**(3): p. 384-390.
110. Rose, D., *On the magnification and resolution of the field emission electron microscope.* Journal of Applied Physics, 1956. **27**(3): p. 215-220.
111. Birdseye, P., D. Smith, and G. Smith, *Analogue investigations of electric field distribution and ion trajectories in the field ion microscope.* Journal of Physics D: Applied Physics, 1974. **7**(12): p. 1642.
112. Grenier, A., et al., *Atomic-scale study of TbCo 2.5/Fe multilayers by laser-assisted tomographic atom probe.* Journal of Applied Physics, 2007. **102**(3): p. 033912.
113. Kelly, T.F. and M.K. Miller, *Atom probe tomography.* Review of scientific instruments, 2007. **78**(3): p. 031101.

References

114. Hellman, O.C., J.B. Du Rivage, and D.N. Seidman, *Efficient sampling for three-dimensional atom probe microscopy data.* Ultramicroscopy, 2003. **95**: p. 199-205.

115. Hellman, O.C., et al., *Analysis of three-dimensional atom-probe data by the proximity histogram.* Microscopy and Microanalysis, 2000. **6**(5): p. 437-444.

116. Williams, C.A., *Atomic scale characterisation of oxide dispersion strengthened steels for fusion applications*. 2012, University of Oxford.

RESEARCH

Paper I

Materials Science & Engineering A 846 (2022) 143280

Contents lists available at ScienceDirect

Materials Science & Engineering A

journal homepage: www.elsevier.com/locate/msea

Effect of cyclic ageing on the early-stage clustering in Al–Zn–Mg(-Cu) alloys

Sohail Shah [a,*], Elisabeth Thronsen [b], Constantinos Hatzoglou [a], Sigurd Wenner [b,c], Calin D. Marioara [c], Randi Holmestad [b], Bjørn Holmedal [a]

[a] Department of Materials Science and Engineering, Norwegian University of Science and Technology (NTNU), N-7491, Trondheim, Norway
[b] Department of Physics, Norwegian University of Science and Technology (NTNU), N-7491, Trondheim, Norway
[c] SINTEF Industry, N-7465, Trondheim, Norway

ARTICLE INFO

Keywords:
Aluminum alloys
Atom probe tomography (APT)
Transmission electron microscopy (TEM)
Cyclic ageing
Natural ageing

ABSTRACT

The cyclic application of mechanical stress to aluminum alloys at room temperature, referred to as cyclic ageing, continuously injects vacancies, enabling dynamic precipitation of a fine distribution of solute clusters. These are uniformly distributed throughout the bulk and are responsible for enhancing the mechanical properties to comparable values as T6 conditions obtained by conventional artificial aging. The atomic structure of the clusters in two Al–Zn–Mg (-Cu) alloys is studied using atomically resolved transmission electron microscopy, and their size, volume density and chemistry are investigated using atom probe tomography. It was found that cyclic ageing yields a high number density of solute clusters exhibiting structural similarities to the GPI zones commonly observed after low temperature ageing in such alloys. A subsequent 10-day natural ageing allows both cluster nucleation and further cluster growth, without altering their atomic structure. As compared to natural ageing, the strengthening caused by the solute clusters is accelerated during cyclic ageing, due to dynamic precipitation. The copper containing alloy also had higher amounts of Mg and Zn. Still, a slightly lower number density of smaller clusters with lower Zn/Mg ratio formed in this alloy, both after cyclic aging and after natural aging. The higher strength of this alloy is attributed to a higher strength contribution from each cluster.

1. Introduction

The Al–Zn–Mg (-Cu) alloys are widely used in the aerospace and automotive industry primarily due to their high strength to weight ratio and high corrosion resistance. Having good formability, these alloys allow for a wide range of processing routes such as extrusion, rolling and forging [1–3]. The main strengthening mechanism is precipitation hardening which involves a high temperature treatment above the solvus line of the system, such as a solution heat treatment (SHT, at >400 °C), followed by a rapid quench to room temperature and artificial aging (AA). During the high temperature treatment, the solute is dissolved into the host Al matrix and will, together with the high density of vacancies form a supersaturated solid solution (SSSS) after the rapid cooling. This condition has the maximum precipitation potential that will be utilized during the AA (usually at temperatures between 120 and 200 °C) to form a high density of nano-sized metastable precipitates, strengthening the material by providing obstacles for dislocation motion.

However, the SSSS is unstable even during natural ageing (NA) at room temperature, in which case the material gradually hardens due to formation of atomic clusters that are coherent with the aluminum lattice. When the clusters achieve periodic order in one or more spatial dimension, they are often referred to as Guinier-Preston (GP) zones [4, 5]. Two types of GP zones have been reported for the Al–Zn–Mg alloy system, namely the spherical GPI zones and the plate-like GPII zones [6].

The general precipitation sequence during artificial ageing is given as

$$\text{SSSS} \rightarrow \text{atomic clusters} \rightarrow \text{GP zones} \rightarrow \eta' \rightarrow \eta \quad (1)$$

Recently, Sun et al. [7] have demonstrated a new approach for precipitating a very high number density of clusters, leading to strengths equal to and even higher than those from conventionally aged materials. The novel cyclic strengthening approach involves cyclic deformation of a solution heat treated and quenched material. During plastic deformation, the back-and-forth gliding of dislocations creates vacancies produced during dragging of jogs. These excess vacancies aid local diffusion. Some dislocation loops were present in the microstructure, but the extremely fine distribution of solute clusters being formed,

* Corresponding author.
E-mail address: sohail.shah@ntnu.no (S. Shah).

https://doi.org/10.1016/j.msea.2022.143280
Received 10 March 2022; Received in revised form 7 May 2022; Accepted 9 May 2022
Available online 13 May 2022

Paper I

Effect of cyclic ageing on the early-stage clustering in Al-Zn-Mg(-Cu) alloys

Sohail Shah[a*], Elisabeth Thronsen [b], Constantinos Hatzoglou[a], Sigurd Wenner[b,c], Calin D. Marioara[c], Randi Holmestad[b], Bjørn Holmedal[a]

[a]*Department of Materials Science and Engineering, Norwegian University of Science and Technology (NTNU), N-7491 Trondheim, Norway*

[b]*Department of Physics, Norwegian University of Science and Technology (NTNU), N-7491 Trondheim, Norway*

[c]*SINTEF Industry, N-7465, Trondheim, Norway*

Abstract

The cyclic application of mechanical stress to aluminum alloys at room temperature, referred to as cyclic ageing, continuously injects vacancies, enabling dynamic precipitation of a fine distribution of solute clusters. These are uniformly distributed throughout the bulk and are responsible for enhancing the mechanical properties to comparable values as T6 conditions obtained by conventional artificial aging. The atomic structure of the clusters in two Al-Zn-Mg(-Cu) alloys is studied using atomically resolved transmission electron microscopy, and their size, volume density and chemistry are investigated using atom probe tomography. It was found that cyclic ageing yields a high number density of solute clusters exhibiting structural similarities to the GPI zones commonly observed after low temperature ageing in such alloys. A subsequent 10-day natural ageing allows both cluster nucleation and further cluster growth, without altering their atomic structure. As compared to natural ageing, the strengthening caused by the solute clusters is accelerated during cyclic ageing, due to dynamic precipitation. The copper containing alloy also had higher amounts of Mg and Zn. Still, a slightly lower number density of smaller clusters with lower Zn/Mg ratio formed in this alloy, both after cyclic aging and after natural aging. The higher strength of this alloy is attributed to a higher strength contribution from each cluster.

Keywords

Aluminum alloys, Atom probe tomography (APT), Transmission electron microscopy (TEM), Cyclic ageing, Natural ageing

1. Introduction

The Al-Zn-Mg(-Cu) alloys are widely used in the aerospace and automotive industry primarily due to their high strength to weight ratio and high corrosion resistance. Having good formability, these alloys allow for a wide range of processing routes such as extrusion, rolling and forging. [1-3]. The main strengthening mechanism is precipitation hardening which involves a high temperature treatment above the solvus line of the system, such as a solution heat treatment (SHT, at >400°C), followed by a rapid quench to room temperature and artificial aging (AA). During the high temperature treatment, the solute is dissolved into the host Al matrix and will, together with the high density of vacancies form a supersaturated solid solution

(SSSS) after the rapid cooling. This condition has the maximum precipitation potential that will be utilized during the AA (usually at temperatures between 120 to 200ºC) to form a high density of nano-sized metastable precipitates, strengthening the material by providing obstacles for dislocation motion.

However, the SSSS is unstable even during natural ageing (NA) at room temperature, in which case the material gradually hardens due to formation of atomic clusters that are coherent with the aluminum lattice. When the clusters achieve periodic order in one or more spatial dimension, they are often referred to as Guinier-Preston (GP) zones [4, 5]. Two types of GP zones have been reported for the Al-Zn-Mg alloy system, namely the spherical GPI zones and the plate-like GPII zones [6].

The general precipitation sequence during artificial ageing is given as

$$\text{SSSS} \rightarrow \text{atomic clusters} \rightarrow \text{GP zones} \rightarrow \eta' \rightarrow \eta \qquad (22)$$

Recently, Sun *et al.* [7] have demonstrated a new approach for precipitating a very high number density of clusters, leading to strengths equal to and even higher than those from conventionally aged materials. The novel cyclic strengthening approach involves cyclic deformation of a solution heat treated and quenched material. During plastic deformation, the back-and-forth gliding of dislocations creates vacancies produced during dragging of jogs. These excess vacancies aid local diffusion. Some dislocation loops were present in the microstructure, but the extremely fine distribution of solute clusters being formed, contributes to a major part of the strength, in a similar manner to that of the conventional artificially aged samples. Clusters observed in that study were suggested to not be the same type as those formed during conventional NA (the GPI and GPII zones).

Dynamic precipitation has been studied for a variety of heat-treatable aluminum alloys, and promising strength and work hardening have been reported [8-12], while other aspects like influence of the crystallographic texture, fatigue and fracture properties are still lacking. Studies focusing on the atomic structure of the clusters precipitated during cyclic strengthening, are sparse. In the present study, we aim at investigating the crystal structure of such clusters and compare them with the clusters precipitated during long-time storage, i.e., NA.

Recently, the atomic structure of the GPI zones in the 7xxx alloy system was determined [13]. The study showed that the GPI zones are built with a single building block that connects along certain directions in the Al matrix to form larger particles. The basic unit can be described as a truncated cube octahedron (TCO) consisting of three shells centered on a possible interstitial. The first shell consists of the atoms at the corners of the six faces of an inner octahedron and are occupied by Zn atoms. The second shell is an inscribed cube, for which the eight corners are occupied by Mg. The corner atoms of the octahedron are located at the cube centers. The last shell is a TCO. Its 24 vertices are ideally occupied by Zn, while the corners of the cube are located at the centers of the hexagonal faces of the TCO. The TCO can connect along <001>Al

with its unique axis [001]GPI. Normal to its unique axis it can connect along <411>Al and <330>Al. Mixing of the <411>Al- and <330>Al connections is common, hence the individual GPI zones show variation in structure.

The focus of this study is to systematically compare the clusters formed in two commercial 7xxx alloys immediately after cyclic ageing. Their stability during NA is assessed and the effect of 10 days further storage at room temperature is characterized. Emphasis is placed on characterization of the structure and chemistry of these clusters in relation to the conventional GPI zones formed by NA.

2. Materials and Methods

2.1. Materials

Two commercial alloys are studied, both received as extruded 6 mm thick plates from Benteler automotive. The compositions of the two alloys are given in Table 3. Both the alloys had similar texture. The major difference is that the 7046 contains copper and is slightly denser in solute than the 7003. The samples were SHT at 480ºC for half an hour in a salt bath followed by water quenching.

Table 3. Alloy composition of the investigated alloys (in wt.% and at.%)

		Cu	Fe	Mg	Si	Ti	Zn	Zr	Al
7046	wt%	0.28	0.2	1.31	0.08	0.03	6.47	0.15	Bal.
	at%	0.12	0.1	1.52	0.08	0.00	2.79	0.05	
7003	wt%	0.01	0.22	0.73	0.09	0.02	5.68	0.15	Bal.
	at%	0.00	0.11	0.84	0.09	0.01	2.43	0.05	

Peak Aged (PA) samples were also prepared for comparison with samples strengthened by cyclic deformation. Peak ageing heat treatment for these two alloys involved heating the samples up to 140ºC for 7 hours (16.4ºC per hour) and keeping them at 140ºC for 17 hours. The microstructure of PA samples is well known to consist of developed plate shaped η', along with $\eta_{1\text{-}2}$ [14, 15]. Only the mechanical strengths were used for comparison. NAed samples from both alloys were also used to compare the structure of clusters formed during CA with the GPI zones formed during conventional NA. Long NAed samples with stabilised hardness were also used for comparison of strength contributions with the CA samples.

2.2. Cyclic Ageing and Hardness Measurements

Samples for cyclic ageing (CA) tests, with the tensile axis along the extrusion direction, were machined. As shown in Figure 23, they were flat-shaped with a square cross section of 6 mm

thickness and width. The uniform length was 12 mm. CA tests, comprising of tension-compression following a sinusoidal waveform for the applied force, as seen in Figure 23b, were carried out at a range of different frequencies. Initially, the stress amplitude was set around the yield strength (YS) of the SHT condition. The stress amplitude was gradually increased during the CA, up to a target stress. To ensure the CA samples were not subjected to excessive plastic deformation, the target stress was chosen slightly below the YS of the PA condition and the frequency was optimized. The CA experiments were designed based on the studies by Hutchinson *et al.* [10] and Sun *et al.* [7]. The stress amplitude was increased systematically, with the stress for cycle *n* given by:

$$\sigma_n = \sigma_0 + (\sigma_t - \sigma_0)\sqrt{\frac{n}{N}}. \quad (23)$$

Here σ_0 and σ_t are the initial and target stress amplitude strength. An optimization study had been carried out previously guiding how to optimally choose the target stress and the number of cycles *N* to reach it. The ideal condition for each alloy was applied, and the clusters in the resulting condition were studied by transmission electron microscopy (TEM) and atom probe tomography (APT). The optimization study will be published as part of a separate article.

Flat pieces from the tensile samples were ground and polished for micro-hardness measurements using a 1000 gf Vickers indenter. The mean hardness values were based on 5 readings each.

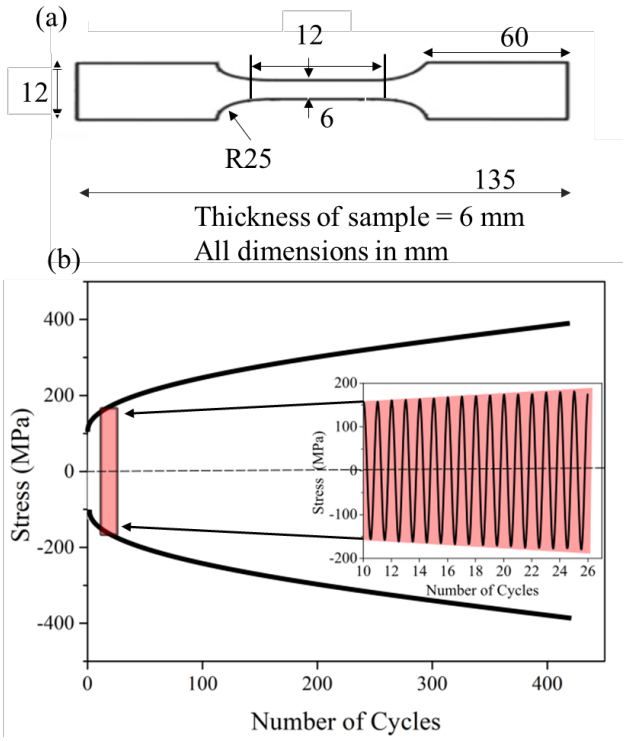

Figure 23. (a) Geometry of test specimen used for cyclic ageing and tensile tests, (b) cyclic ageing profile. Insert shows a section of the gradual increase in stress amplitude.

2.3. APT sample preparation, acquisition parameters and cluster characterization methodologies

Electropolishing is preferred preparation methodology to avoid the contamination by ion implantation techniques. However, attempts to prepare the cyclic aged samples by electropolishing did not succeed. Hence, the APT needles from the cyclic aged material were prepared according to the conventional focused ion beam (FIB) lift out method [16] using the FEI Helios G2 dual beam instrument with a Ga^+ ion source. The needles were sharpened to around 50-100 nm using an 8 kV Ga^+ beam, followed by a 2 kV final clean-up step to remove higher concentrations of implanted high-energy Ga ions.

APT samples from the 3 months NA condition were prepared by following a standard two-step electropolishing process [17]. Rods of 0.3 x 0.3 x 20 cm^3 were cut from the samples and mechanically ground. The first step of the electropolishing was done using 25 vol.% perchloric

acid in 75 vol.% acetic acid. The final step was a two-step process using 10 vol.% perchloric acid followed by 2 vol.% perchloric acid in 98 vol.% 2-butoxylethanol to produce sharp needles. APT analysis was carried using a Local Electrode Atom Probe (LEAP) 5000XS by Cameca Instruments Inc. This is a straight flight path instrument with a detection efficiency of about 80%. All samples were run at 30 K base temperature in laser mode with a detection rate of 0.5%. An equivalent pulse fraction of 20% was used and calibrated in the range of 55-110 pJ, depending on the sample geometry. The pulse rate used was 250 kHz for all samples. Datasets, ranging from 50-150 million ions, were collected for the CA material. The reconstructions and the post processing analyses were carried out using the Integrated Visualization and Analysis Software (IVAS) by Cameca Instruments Inc. Complementary to IVAS, the Norwegian Atom Probe App [18] software has been used. It has been developed by C. Hatzoglou from the Norwegian University of Science and Technology (NTNU) and is an open access software dedicated to APT data treatment [19]. The accurate estimation of the reconstruction parameters was carried out using the structural information and following the protocols of Gault *et al.* [20]. Sub-volumes were carefully chosen from APT datasets of cyclic aged samples for performing cluster analyses from regions without Ga implantation and away from the poles. The NA 3-month conditions were prepared by electropolishing and hence contained no Ga implantation, making the whole dataset suitable for analysis.

The "isoposition method" (IPM) was used to identify clusters in all the APT datasets. This method developed at the Groupe de Physique des Materiaux (University of Rouen, France) is based on chemical concentration (i.e., Mg+Zn) and atomic distance criteria. A detailed explanation of this algorithm and its criteria estimation can be found elsewhere [21, 22]. The identified clusters exhibit an over atomic density compared to the matrix (up to 4-5 times higher), plus a morphological distortion (spherical in TEM, Fig.5 and ellipsoidal in APT). This is due to the local magnification effect typically seen due to difference in evaporation fields between cluster/matrix during APT analysis [23, 24]. The cluster dimension along the evaporation direction (i.e. Z direction) remains unchanged by local magnification as previously reported in [25, 26]. The size of the clusters is so estimated from the Extent z (E_z) parameter, obtained from the cluster analysis. This parameter is defined as

$$E_z = |Z_{max} - Z_{min}| \tag{24}$$

where Z_{max} and Z_{min} are the outermost atoms of the cluster in the z-direction (the direction of evaporation). Considering local magnification effects, this is the least biased direction in the APT. E_z is based on the maximum distance between cluster atoms in this direction. The size and composition errors were calculated based on the standard deviation between the clusters while the error of the number density was calculated by dividing the number density by the square root of the total number of clusters. The clusters at the edge of the dataset which are not completely inside are considered contributing half to estimate the number density.

Cluster finding algorithms have many drawbacks, because of parameter selection biasing [27], in particular for very small clusters with size ranging from 1-2 nm. An alternative method is used here, based on the pair correlation functions (PCF) obtained from the APT dataset, as

illustrated in Figure 25. It is a radial distribution function (RDF) based method with the advantage of being self-consistent, parameter free and uses the information from all atoms in the dataset. This methodology has previously been used to characterize precipitates in an Al-Cu-(Li-Mg) alloy system [28] as well as an Al-Zn-Mg system [29].

The approach makes use of an RDF calculated from the APT datasets, in which the specified species (in our case Zn and Mg) are examined. De Geuser *et al.* [30] introduced an γ_{i-j} pair correlation function between two elements by normalizing and scaling the RDF as

$$\gamma_{i-j}(r) = C_i C_{i-j}(r) - C_i C_j \tag{25}$$

where C_i and C_j are the bulk compositions of the respective elements obtained from the APT dataset, and $C_{i-j}(r)$ is the average composition of element j at a distance r. This is obtained from the atoms of element *i* obtained from the RDF.

For $i = j$, i.e., correlations of the same element, Eq (25) can be written as

$$\gamma_{i-i}(r) = C_i C_{i-i}(r) - C_i^2 \tag{26}$$

Also, when there is no correlation, which is the case for large *r* values, $\gamma_{i-i}(r) = 0$. At $r = 0$, the PCF corresponds to the mean square composition fluctuation, i.e. of precipitates and matrix, and can be written as,

$$\gamma_{i-i}(0) = \Delta C_i^2 = (C_p - C)(C - C_m) \tag{27}$$

where, C, C_m, and C_p are the bulk, matrix, and precipitate compositions respectively. The mean square compositional fluctuation (ΔC_i^2) is observed at $r = 0$ and decreases to zero as r increases with a characteristic correlation length which relates to the size of the compositional fluctuations (precipitates/clusters).

2.4. TEM sample preparation and acquisition parameters

For TEM specimen preparation, the samples were first mechanically thinned down to ~ 100 µm. The specimens were punched out to 3 mm disks and subsequently electropolished with a Struers TenuPol-5 machine using an electrolyte consisting of 1/3 HNO_3 and 2/3 CH_3OH. The electrolyte was kept at -25°C ± 5°C and the applied voltage was 20 V. An image- and probe corrected JEOL ARM200CF microscope, operated at 200 kV, was used for high-angle annular dark-field scanning TEM (HAADF-STEM) imaging. The convergence semi-angle was 27 mrad and the inner and outer collection semi-angles were 68 and 155 mrad, respectively. The probe current was about 60 pA, which gives a good signal, while maintaining sufficient spatial resolution. The images were filtered by performing a fast Fourier transform (FFT) and superimposing a low-pass mask on the FFT of approximately 6.7 nm^{-1}, before performing an inverse FFT.

3. Results

3.1. Hardness

The hardness immediately after quenching was recorded and the subsequent reading was taken directly after CA, which took 4 hours and 40 minutes for the optimized condition running at 0.025 Hz. The results are shown in Figure 24 for both alloys. The hardness of the grip region of the CA samples was also measured as a reference. Since this region did not undergo CA and is assumed unaffected, it gives a precise estimation of the hardness evolution by NA during the time spent performing the CA. Sample preparation for both TEM and APT took around 3 hours for all conditions analyzed. As expected, the 7046 alloy was stronger than the 7003 alloy, due to its higher alloying content and Cu addition, c.f. Table 3 [31]. The hardness of 7046 was 61 ± 2 HV after solutionising and increased to around 135 ± 3 HV during the CA treatment. At the same time, the hardness at the grip area (NA) increased to 96 ± 3 HV. A similar trend was observed for 7003, where the hardness sharply increased from the as quenched (AQ) state at 47 ± 2 HV to 105 ± 1 HV after CA.

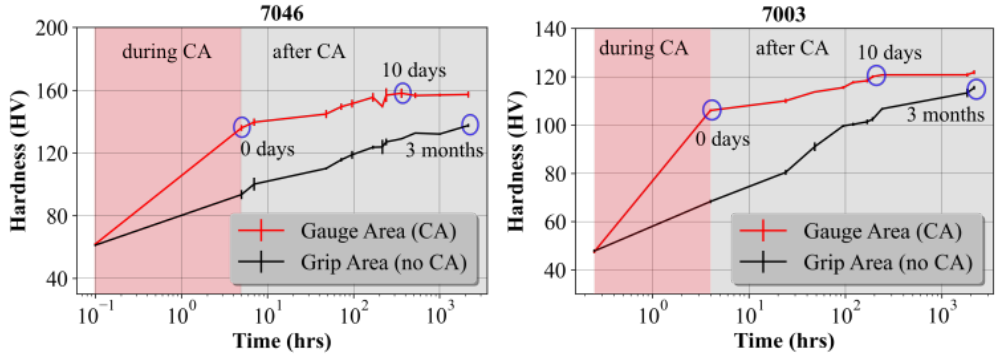

Figure 24. Hardness evolution after SHT and quenching follows the red curves, highlighting the hardness evolution of the CA samples. The black curves show the corresponding NA evolution. The blue circles indicate the conditions studied by TEM and APT.

For both alloys, there was a gradual increase in hardness during NA after CA. After 10 days at room temperature, it almost saturated to a hardnesses of around 158 ± 2 HV and 121 ± 2 HV for 7046 and 7003, respectively. Selected samples were chosen for detailed APT and TEM analysis, as indicated with blue circles in Figure 24.

3.2. APT data interpretation

APT analyses for all three conditions (CA, CA + NA 10 days and NA 3 months) show a high number density of fine solute clusters (of the order of 10^{24} clusters/m^3) for both alloys, see Figure 25. As seen in Figure 25(c) and (d), the 10 days of storage (NA) after the CA resulted in slightly larger clusters compared to the ones after CA, shown in Figure 25(a) and (b) for

7046 and 7003, respectively. During this time the number density also increased, as seen from Table 4. Figure 25(e) and (f) display the APT results of 3 months NA for 7046 and 7003, respectively, also showing a high number density of similarly sized spherical clusters. The size of the clusters in 7046 is consistently smaller compared to the ones in 7003 for the three conditions analyzed, but the difference in size is not large c.f. Table 4.

The chemistry of the clusters does not vary much between the three conditions of the same alloy, with an average Zn/Mg ratio of around 1.6 for 7046, and around 2.1 for 7003, see Table 4.

The clusters are rich in Mg and Zn and are in general spherical, which is evident from the cluster morphology maps shown in Figure 26a-c. Each map is divided into four quadrants, corresponding to disc, sphere, lath and rod. These are defined based on the oblateness and aspect ratio of the best fit of an ellipsoid to each cluster [32, 33]. L_1, L_2 and L_3 are defined as the three major axes of each cluster, where $L_1 > L_2 > L_3$, and the aspect ratio (L2/L1) vs oblateness (L3/L2) is plotted in the cluster morphology map. Each circle represents one cluster and has a size proportional to the number of ions detected in that cluster.

Table 4. Statistical results of cluster analysis for 7046 and 7003 alloys.

Alloy	Condition	Number Density ($10^{24}/m^3$)	Size (nm)	Zn/Mg	(Zn+Cu)/Mg
7046	CA	1.81 ± 0.19	1.12 ± 0.53	1.63 ± 0.49	1.66 ± 0.51
	CA + NA 10 days	3.15 ± 0.23	1.50 ± 0.89	1.58 ± 0.26	1.61 ± 0.27
	NA 3 months	2.11 ± 0.64	1.87 ± 0.65	1.53 ± 0.12	1.58 ± 0.11
7003	CA	3.75 ± 0.25	1.27 ± 0.44	2.14 ± 0.13	2.15 ± 0.14
	CA + NA 10 days	4.36 ± 0.27	1.57 ± 0.58	2.24 ± 0.25	2.21 ± 0.15
	NA 3 months	2.95 ± 0.67	2.01 ± 0.85	2.09 ± 0.14	2.10 ± 0.14

Table 5. Calculated contribution of SSSS to the yield stress based on APT measurements of solute levels in-between the clusters, and experimentally measured yield stress and UTS for the two alloys in the three investigated conditions. * indicates the yield stress and UTS from NA 1-year samples. This is done since the hardness measured has plateaued from 3 months to 1 year. The samples needed for tensile testing were not available in the 3 months NA condition.

Condition	YS from SSSS (MPa)		Experimental YS (MPa)		Experimental UTS (MPa)	
	7046	7003	7046	7003	7046	7003
CA	63.0	47.8	408	308	475	372
CA + NA 10 days	53.1	36.6	447	356	532	445
NA 3 months	48.5	35.3	368*	299*	534*	463*

Figure 26(d) and (e) show the calculated Mg-Mg and Zn-Zn PCFs, respectively, for all datasets of 7003 shown in Figure 25. Careful observation of the PCFs shows that the width of the PCF increases from CA to CA + NA 10 days and it is even larger at NA 3 months. As explained by De Geuser and Gault [34], an increased width of the PCF means an increased correlation length which in turn signifies the trend of increase in the size of clusters. This is the case for both Mg-Mg and Zn-Zn correlation lengths. The PCF for CA + NA 10 days and NA 3 months are almost identical and overlapping.

The solute concentration in the matrix in the clustered conditions was extracted based on the DIAM methodology from the APT datasets [35]. The results are summarized in Figure 26(f). A high amount of solute in SSSS is consumed during the CA as the concentrations of Mg and Zn drop sharply from SSSS assuming all solutes dissolve during SHT. The solute consumption from the matrix continues after CA until the 10 days NA. Interestingly, 3 months NA has very similar solute content in the matrix as the CA + NA 10 days in both alloys.

Table 5 summarizes the contribution of SSSS to the yield strength estimated from the model of Deschamps *et al*. [36] as

$$\sigma_{sol} = KC_{sol}^{\frac{2}{3}} \tag{28}$$

where, σ_{sol} is the strength contribution from the solute in the matrix, K= 840 MPa is a constant adjusted to the yield strength of the material in SSSS and C_{sol} is the added volume concentrations of the solutes in the matrix; in our case *sol* corresponds to being Mg, Zn and Cu [37]. The K value for both alloys is chosen the same, since the effect of Cu is negligible due to very low concentrations of it in solid solution.

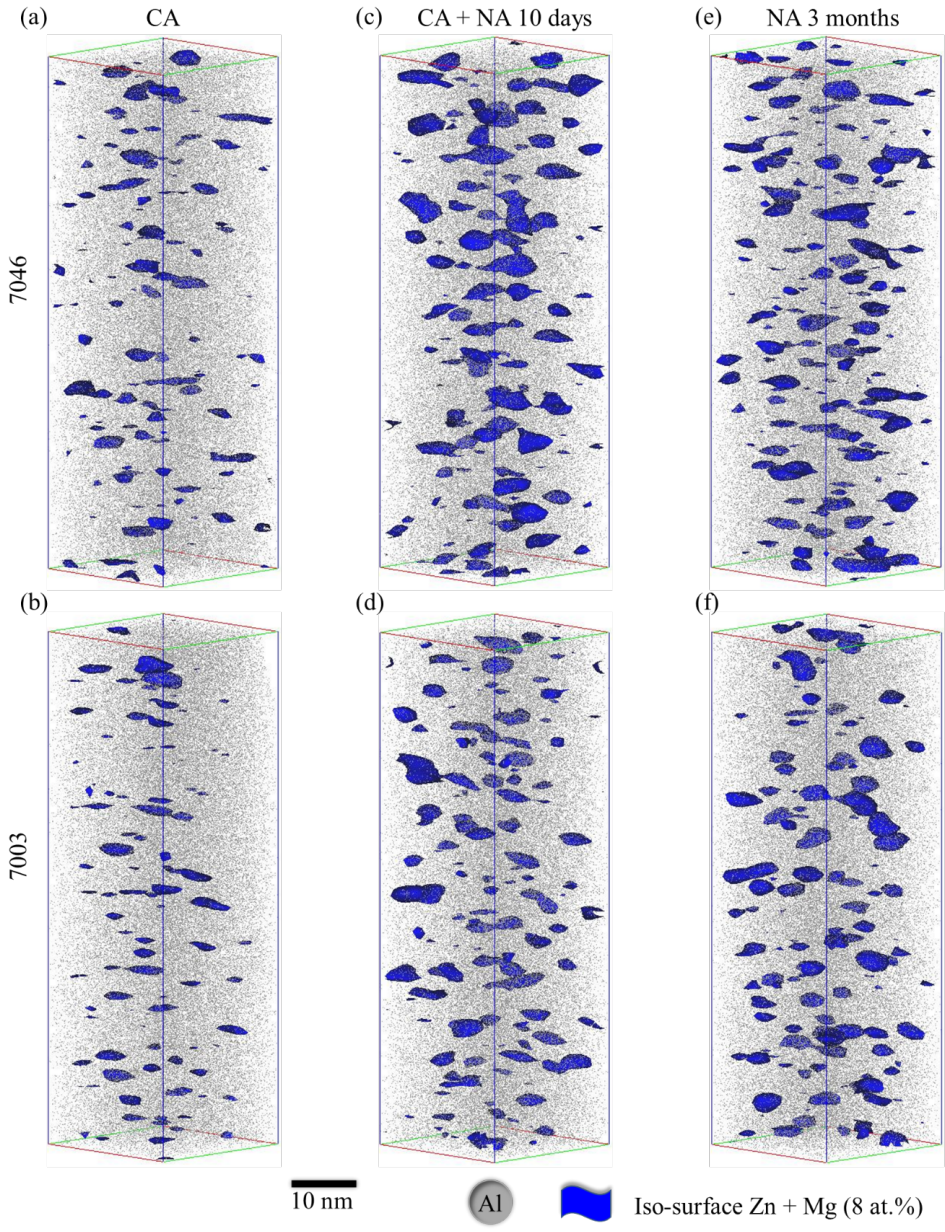

Figure 25. Sub-volumes within the dataset of dimensions 25 x 25 x 80 nm^3 to spatially visualize the clusters. The three conditions shown are (a) CA (c) CA aged + NA 10 days (e) NA 3 months for 7046 and (b) CA (d) CA + 10 days NA and (f) NA 3 months for 7003.

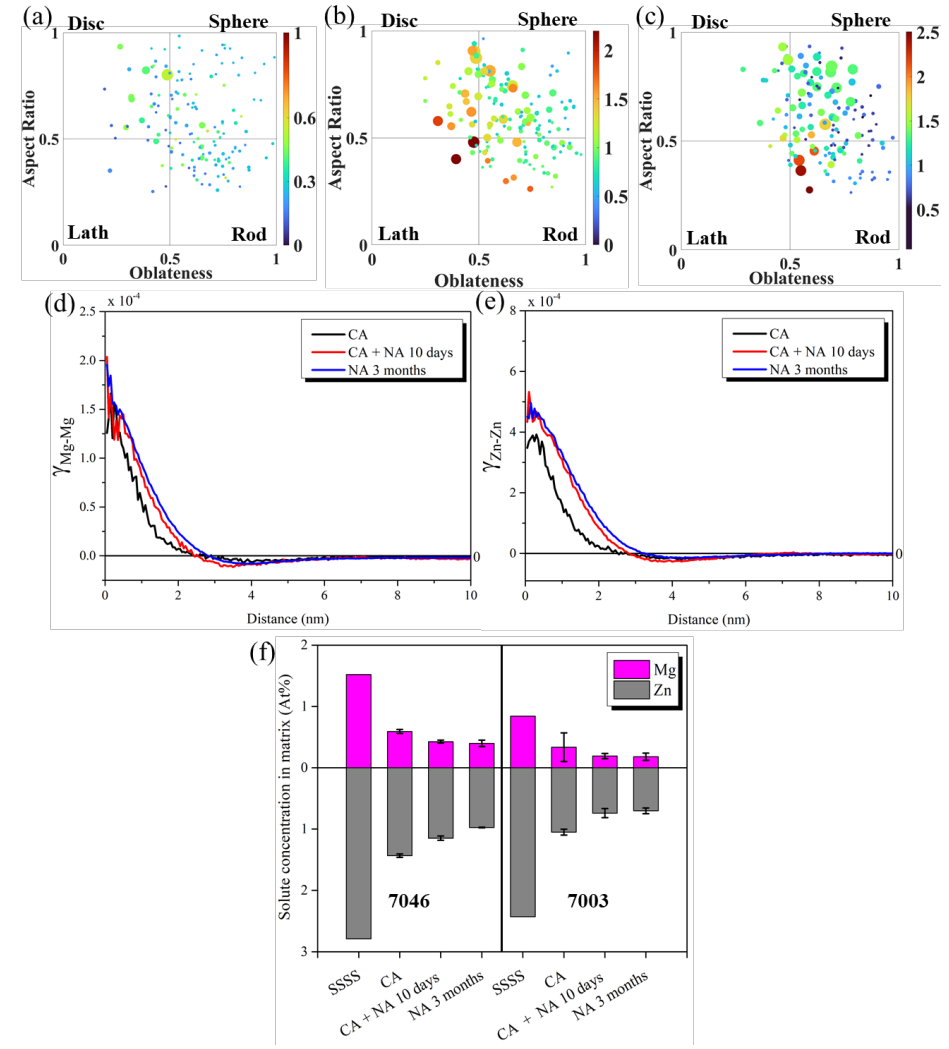

Figure 26. Aspect ratio vs oblateness plots for clusters identified in the sub-volumes for CA, CA + NA 10 days and NA 3 months shown through (a-c) respectively for the 7003 alloy. The color scale shows the size of the clusters as radius of gyration in the evaporation direction while the size of the circles indicate the total number of atoms inside each cluster. Pair correlation functions for (d) Mg-Mg pairs and (e) Zn-Zn pairs from the APT datasets shown for 7003 in Figure 25. The black line represents the theoretical PCF for a random distribution. (f) Zn and Mg concentrations in the matrix of the two alloys compared with the SSSS for different conditions.

3.3. Atomic structure of the CA and NA clusters by TEM

Figure 27 shows atomically resolved HAADF-STEM images of the microstructure in the three investigated conditions, CA, CA + NA 10 days and NA 3 months for the 7046 and 7003 alloys. All images are taken along the <001>Al zone axis. One overview HAADF-STEM image and two enlarged regions are shown for each condition. We could identify TCO structural units of the GPI zones [13] in all conditions of both alloys, and centers of TCOs are indicated with red disks in the enlarged regions, some of the disks are indicated by yellow arrows.

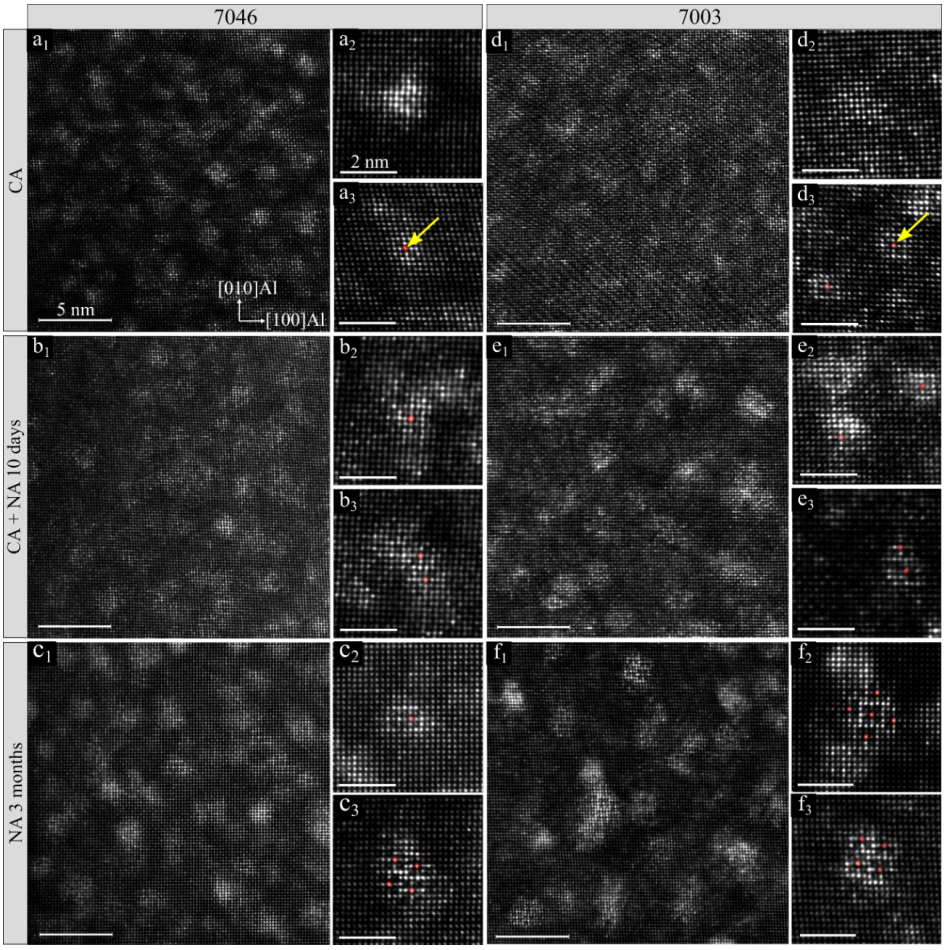

Figure 27. Atomically resolved HAADF-STEM images along <001>Al for the three investigated conditions. a_1- f_1: Overview image for each condition. a_2- f_2 and a_3- f_3: Enlarged regions showing example clusters for each condition. The red disks along with the yellow arrows indicate the center of the TCOs. The lattice appears skewed in some images because of sample drift during image acquisition.

All three conditions exhibited a high number density of spherical clusters with varying sizes. Some clusters showed no clear atomic ordering, exemplified in Fig. $5a_2$ and $5d_2$ for 7046 and 7003, respectively. Such contrast might arise from clusters being far from the entrance surface or clusters consisting of randomly aggregated solutes rather than GP zones exhibiting clear atomic ordering. Most probably, a mixture of buried clusters and randomly aggregated solutes is present. The clusters that do exhibit ordering were all based on the same TCO structural units previously found in conventional NA samples [13, 38]. The main difference was that in CA conditions they always consisted of single TCOs, as highlighted in Figure $27a_3$ and $5d_3$ by the red disks indicating the central atomic column of the TCO.

To investigate the microstructural evolution from CA to CA + 10 days NA and compare with the microstructure after NA 3 months, 300-400 clusters per condition were investigated. The clusters were investigated in terms of atomic ordering and categorized as single TCO, connected TCO and disordered. Their relative occurrence is shown in Table 6.

Table 6. Quantification of the cluster microstructural differences in CA, CA+NA 10 days and NA 3 months based on the HAADF-STEM experiments. The clusters were categorized as single-, connected TCOs and disordered, and the numbers show their relative occurrence.

Alloy	**Condition**	**Single TCO clusters**	**Connected TCO clusters**	**Disordered (no structure identified)**
7046	CA	7%	0%	93%
	CA + NA 10 days	9%	1%	90%
	NA 3 months	8%	4%	88%
7003	CA	7%	0%	93%
	CA + NA 10 days	11%	2%	87%
	NA 3 months	4%	12%	84%

The microstructures after 10 days NA are shown in Figure $27b_1$ and Figure $27e_1$ for 7046 and 7003, respectively. Most of the ordered clusters were still single TCOs. A small population of connected TCOs were observed in this condition for both alloys. Such clusters are exemplified in Figure $27b_3$ and Figure $27e_3$ for alloys 7046 and 7003, respectively.

By comparing the appearance of the GPI zones in alloy 7046 with those in 7003 in the NA 3 months condition, there is a noticeable difference: alloy 7003 contains a higher fraction of clusters based on connected TCOs. This is exemplified in Figure 27f_2 and f_3, where GPI zones consisting of 5 and 4 TCOs connected along the <411>Al directions are shown, respectively. In contrast, the GPI zones in 7046 more often consist of single TCOs, exemplified in Figure 27c_2. This effectively implies that the clusters are in general coarser in alloy 7003 compared to those in 7046. About half of the connected GPI zones in the 3 months NA condition of alloy 7046 consist of multiple TCOs connected only along <411>Al, as exemplified in Figure 27c_3.

3.4. Mechanical Response

The engineering stress-strain curves from all the test conditions are shown in Figure 28(a) and (b) for 7046 and 7003, respectively. Samples with NA for 1 year were used instead of NA 3 months to measure the effect of long-term NA and compare it with the strength of the CA conditions.

Immediately after CA, the samples are consistently lower in YS than the artificially PA samples for both alloys but have higher uniform elongations. After further 10 days NA, the samples have higher YS and UTS than CA, but similar uniform elongation. For both alloys, the CA + NA 10 days condition results in higher UTS than the PA condition. For alloy 7003, the YS in the CA + NA 10 days condition is similar to, while for 7046 it is smaller than, the respective PA condition. The uniform elongation is significantly larger for the one-year NA condition, while for all other conditions is between 0.09 to 0.11 as summarized in Figure 28 (c-f). For alloy 7003 the NA 1-year condition had YS similar to that immediately after the CA, while the YS of the CA condition of alloy 7046 was larger than the corresponding NA 1-year condition.

It is noted that the CA, as well as NA conditions, fractured very close to when they reached the maximum nominal stress. On the other hand, the PA condition for both alloys experienced a significant amount of necking before fracture occurred in the neck, as seen in Figure 28 (a and b).

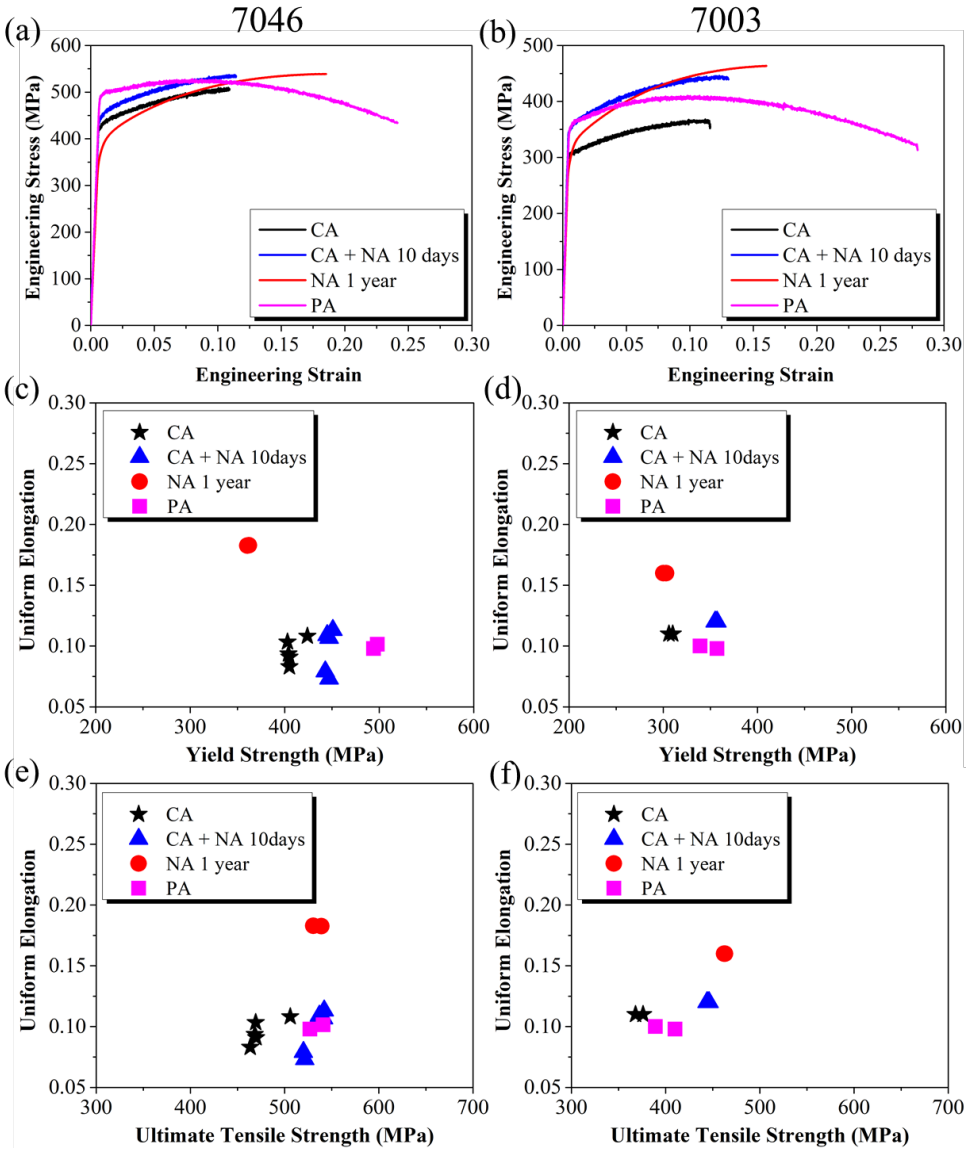

Figure 28. Mechanical response of the two alloys subjected to CA, CA + NA, NA and artificial aging (PA). Engineering stress strain curves of (a) 7046 and (b) 7003. Correlation in YS and uniform elongation for (c) 7046 and (d) 7003. Correlation in UTS and uniform elongation for (e) 7046 and (f) 7003.

4. Discussion

The iso-position cluster analysis reveals a slight increase in size from CA to CA + NA 10 days and an even larger cluster size for the NA 3 months condition (c.f. Table 4). Note that due to local magnification effects and the resolution limit of the APT, it is challenging to quantify very small clusters with cluster identification algorithms [34]. The different composition and potential crystal structure of the particles compared to the matrix lead to differences in the electric field evaporation. The difference in evaporation field leads to a development of a local radius of curvature near the specimen surface and hence in the projection's image. This also causes trajectory aberrations and overlaps, not enabling the one-to-one mapping between the detector and the specimen surface. These errors will contribute similarly for the different samples, hence the relative differences should be more trustworthy than the precise size estimates.

As an alternative to the iso-position cluster analysis, the PCF approach can be used to assess the size estimate with good statistical significance. A comparison of the decay widths of the PCFs in Figure 26 (d and e) indicates that the correlation lengths for both Mg-Mg and Zn-Zn pair correlations shows the same trend as the cluster sizes found by the iso-position method, and therefore gives the same conclusions. The PCF for the CA+ NA 10 days and NA 3 months conditions are close, indicating that the sizes of the clusters are similar for these two conditions. Hence, it can be concluded that CA for a few hours induces accelerated kinetics, and after 10 days of storage, the cluster size is almost similar to NA for three months.

The strength increases about 50MPa and 70 MPa for the 7046 and 7003 alloy respectively during the 10 days of storage after CA. During the same period of time, the concentrations of elements in solid solution, as estimated in Figure 26(f), decays due to the consumption by the growing clusters. From Table 5, this contribution to loss of strength can be estimated to be about 10 MPa. Therefore, the measured strength increases must come from the evolution of clusters. As their number density has only a small increase while they grow (see Table 4), the increase in strength must therefore be caused by the larger clusters that act as stronger obstacles for the gliding dislocations.

The size of the clusters in the 7046 alloy is smaller, with slightly lower number densities estimated than in the 7003 alloy. However, the measured strength of 7046 is higher, as seen from Figure 28 (a and b). To understand this, solute concentrations from the matrix was used to estimate the strength contribution from the atoms in solid solution. The solute concentration in the 7046 is higher than 7003 and contributes to increasing the strength of 7046 by about 15-20 MPa, according to the rough estimate by Eq.(28). However, as seen in Table 5, the difference in their strength from the experimental data is about 100 MPa, which cannot be adequately explained by the solute concentration difference. This suggests that a major part of the strength increase must stem from differences in the intrinsic cluster characteristics. In other words, the Cu-containing clusters in alloy 7046 must be acting as stronger obstacles than the Cu-free clusters of similar size in alloy 7003. The other significant difference between the clusters in the two alloys is their average Zn/Mg ratio as seen in Table 4. The lower Zn/Mg

ratio in the 7046 along with the presence of Cu must be the reason for the enhanced strengths of this alloy.

The HAADF-STEM images showed a large population of nano-sized clusters in both alloys after the CA treatment. As the specimen thickness in this work was around 30-40 nm, many of the clusters will be far from the electron entrance surface and such clusters will exhibit a lower contrast as compared to clusters close to the electron entrance surface. Due to this, the 'Disordered' category in Tab. 4 most likely also incorporates some TCO-based clusters.

The particles that did have a clear structure consisted of single TCOs, which is the basic building block of the GPI zones in Al-Zn-Mg(-Cu) alloys. A single TCO spans four (110)Al planes measured from corner to corner. This distance is $4d_{110} = 1.14$ nm. This fits well with the size of the clusters in the CA condition as measured by APT, which on the average was 1.1 nm and 1.3 nm for 7003 and 7046, respectively, c.f. Table 4.

Sun *et al.* postulated in their work that the clusters precipitated during CA should not be structurally similar to those observed during conventional natural aging, i.e. GP zones [7]. In our study however, we find that the CA clusters consisted of the same TCO building block that constructs the GPI zones in NA conditions. The main difference was that most of the structured CA clusters consisted of single TCOs, while the NA clusters consisted of aggregated TCOs. Consequently, the CA clusters must be smaller, which was proven in our work by the APT measurements c.f. Table 4. After CA + 10 days NA the microstructure consisted of more aggregated clusters, as compared to directly after the CA treatment. This aggregation was attributed to a combination of growth of the disordered clusters and the TCO clusters.

Earlier works on Al-Zn-Mg alloys have shown that the GPI zones nucleated after prolonged NA or in the early stages of AA most often consisted of connected TCOs rather than single TCOs [13, 38]. In the present study this is only verified for the NA 3 months condition of the Cu-free 7003 alloy. For the Cu-containing 7046 however, more single TCOs compared to connected TCOs were observed in the NA condition. APT showed that the clusters in the 7046 alloy incorporated Cu for all three conditions. By investigating the Z-contrast in GPI zones in HAADF-STEM images we conclude that Cu most likely substitutes Zn in their structure, as this contrast is similar in both 7003 and 7046 alloys. If a significant amount of Cu substituted Mg, the Mg atomic columns of the GPI zones would have higher brightness in 7046 compared to 7003, which was not observed. A few atoms in the Zn atomic columns may be substituted with Mg without being observable with the TEM, but as we consistently observed that the Zn atomic columns were much brighter than the Mg atomic columns, this effect is expected to be minor.

A small-angle X-ray scattering (SAXS) investigation [39] has earlier shown that the addition of Cu decreases the nucleation radius of GPI zones. This is in accordance with our observations that 7046 has a smaller average cluster size than 7003 after CA and/or NA, supported both by APT and TEM. The addition of Cu is also known to refine the structure of η' [40], demonstrating that this effect is important for precipitates as well as clusters/GP zones. Upon

comparing the CA clusters with the NA clusters for the Cu-free 7003, it is evident that the effect of CA is similar to that of Cu addition, reducing cluster size and increasing structural disorder.

It has been suggested [7] that the cyclic plastic deformation injects vacancies into the material from dragging of jogs on the gliding dislocations. This is assumed to increase the local substitutional diffusion kinetics, which enhance the precipitation and solute aggregation, and correspondingly strengthening the alloy. A 10-day NA after CA demonstrates a steady increase in the hardness, suggesting diffusion of elements in solid solution even after the CA.

The accumulated plastic strain during CA is large. By monotonic loading, e.g. cold rolling, this would give a significant strength contribution from dislocations being stored during deformation. However, during cyclic straining at low strain amplitudes, like during low-cycle fatigue, most of the storage of dislocations during tensile load are removed in the compression part of the cycle. Very few dislocations could be observed in the structure after CA, and the strength obtained was similar as by NA with a similar number density of GP-zones of comparable size. Hence, it can be concluded that the strength contribution from stored dislocations is small.

In both alloys, higher strengths are found in the 1-year NA and CA + NA 10 days conditions as compared to the strengths of the CA conditions without any NA. From Table 4 we see an increase in cluster density and size when subjecting the CA conditions to subsequent NA, which most likely is responsible for the strength increase. The 3 months NA conditions had lower cluster densities than the CA + NA 10 days, but the clusters were larger. The role of CA here is more of accelerated kinetics by pumping in vacancies and allow for nucleation of clusters with a higher number density. CA does not enhance the mechanical response compared to PA conditions for the alloys used in this study. It is known from the work by Hutchinson *et al.* [10] that the cluster number density keeps increasing during CA, while the cluster sizes remain more or less constant. They suggest that repeated shearing prevents further increase of the cluster sizes. The 10-day NA allows these clusters to slightly grow, which increases the area of the cross-sectional plane the dislocation must cut through and increases the surrounding misfit strain in the lattice. Hence, each cluster should be slightly more difficult to cut through by the gliding dislocations. This is important for achieving higher strength. This implies that the clusters immediately after CA still have the potential to grow during further NA at room temperature. As cluster density is smaller for the NA conditions, their larger clusters act as stronger obstacles to dislocation glide. The NA 1-year sample produced the highest tensile strength, as seen in Figure 28(a and b).

Interestingly, and of importance for some applications, all samples for both alloys, with and without Cu, as processed with NA, CA, and also the samples with CA + 10 days NA, fractured abruptly during tensile testing. A slant ductile shear fracture was observed in all cases, without the commonly observed necking instability, i.e., without the diffuse necking expected for specimens with a square cross section. This is in contrast to the PA samples, which undergo significant amount of necking c.f. Figure 28(a and b). Although the uniform elongations for

the CA and NA samples are comparable with those of the PA conditions, fracture strains are severely compromised due to lack of post necking ductility. This is in contrast to what is earlier reported for CA [7]. An important difference is that earlier axisymmetric material and specimens are considered for a slightly different alloy. CA, although shows promise in the rapid hardening response, has constraints in specimen geometry in order to carry out tension and compression part of the test. However, there is potential for process innovation to carry out similar tests for commercial use. Tension and retraction to zero load can be possibly tried for large sheets where compression can be a challenge. Incremental bending and unbending can also be implemented to see the effect on the mechanical response.

5. Conclusion

Clusters nucleated during cyclic ageing and during natural ageing have been studied by APT and TEM for two Al-Zn-Mg(-Cu) alloys. One of the alloys contained Cu, while the other one was Cu-free. A high number of solute clusters were observed after cyclic ageing. After subsequent storage at room temperature cluster density and size increased, which correlated with increasing material strength. This saturated after 10 days of storage, suggesting that the clusters had stabilized. Storage at room temperature after CA is concluded to be very important for obtaining strength levels comparable to that of the peak age conditions obtained by artificial ageing.

When the same alloys were subjected to conventional natural aging for three months, slightly larger clusters were observed as compared to the CA conditions, but with similar chemistry. From TEM analysis of the atomic structure of the clusters it is concluded that the dynamically precipitated clusters are constructed with the same TCO structural unit as the GPI zones nucleated during conventional natural ageing. For both alloys, most of the structurally ordered clusters found in the CA and in CA + NA 10 days conditions consisted of single TCOs. Single TCOs were also found to dominate in the naturally aged Cu-containing 7046 alloy. The Cu-free 7003 alloy, on the other hand, contained a higher number density of connected TCOs along <411>Al and <330>Al in the naturally aged condition. The number density of clusters in the 7046 alloy, either natural or cyclic aged, was found to be similar or slightly lower, and the clusters smaller than in the 7003 alloy. The higher strength of natural or cyclic aged 7046 alloy could not be explained solely by a higher concentration of elements in solid solution. It is concluded that the Cu-containing clusters with a different Zn/Mg ratio to the 7003 alloy must be acting as stronger obstacles for dislocation glide, as compared to Cu free clusters of similar size.

Data availability

The raw data used to reproduce the presented results are available in the Zenodo repository http://doi.org/10.5281/zenodo.6344071

Declaration of Competing Interest

The authors declare that they have no known competing financial interests or personal relationships that could have appeared to influence the work reported in this paper.

Acknowledgement

The authors wish to thank Hanne-Sofie Søreide for her support in the APT lab and Akash Gopal for conducting certain mechanical tests. The Research Council of Norway (RCN) is acknowledged for funding the NTNU atom probe facility through the Norwegian Laboratory for Mineral and Materials Characterization (MiMaC) project number: 269842. This work was supported by the NTNU Digital Transformation initiative 'AllDesign' (E.T. and R.H.) and the RCN through the 'SumAl' project (NFR: 294933) (C.D.M., S.W. and B.H), supported by Hydro, Benteler Automotive Raufoss AS and Neuman Aluminium. The RCN is further acknowledged for the support to the Norwegian Micro-and Nano-Fabrication Facility, NorFab. The STEM work was conducted on the NORTEM infrastructure (NFR: 197405) at the TEM Gemini Centre, Trondheim Norway.

References

[1] T. Dursun and C. Soutis, "Recent developments in advanced aircraft aluminium alloys," Materials & Design (1980-2015), vol. 56, pp. 862-871, 2014.

[2] O. Jensrud, "High strength aluminium alloys extrusions-a review of the thermo-mechanical-process in high performance profile manufacturing," in Key Engineering Materials, 2012, vol. 491: Trans Tech Publ, pp. 11-18.

[3] J. Hirsch, "Recent development in aluminium for automotive applications," Transactions of Nonferrous Metals Society of China, vol. 24, no. 7, pp. 1995-2002, 2014.

[4] A. Guinier, "Structure of age-hardened aluminium-copper alloys," Nature, vol. 142, no. 3595, pp. 569-570, 1938.

[5] G. Preston, "The diffraction of X-rays by age-hardening aluminium copper alloys," Proceedings of the Royal Society of London. Series A. Mathematical and Physical Sciences, vol. 167, no. 931, pp. 526-538, 1938.

[6] V. Hansen, O. Karlsen, Y. Langsrud, and J. Gjønnes, "Precipitates, zones and transitions during aging of Al-Zn-Mg-Zr 7000 series alloy," Materials science and technology, vol. 20, no. 2, pp. 185-193, 2004.

[7] W. Sun et al., "Precipitation strengthening of aluminum alloys by room-temperature cyclic plasticity," Science, vol. 363, no. 6430, pp. 972-975, 2019.

[8] W. Han, Y. Chen, A. Vinogradov, and C. Hutchinson, "Dynamic precipitation during cyclic deformation of an underaged Al–Cu alloy," Materials Science and Engineering: A, vol. 528, no. 24, pp. 7410-7416, 2011.

[9] A. Deschamps, G. Fribourg, Y. Brechet, J. L. Chemin, and C. Hutchinson, "In situ evaluation of dynamic precipitation during plastic straining of an Al–Zn–Mg–Cu alloy," Acta materialia, vol. 60, no. 5, pp. 1905-1916, 2012.

[10] C. Hutchinson, F. De Geuser, Y. Chen, and A. Deschamps, "Quantitative measurements of dynamic precipitation during fatigue of an Al–Zn–Mg–(Cu) alloy using small-angle X-ray scattering," Acta materialia, vol. 74, pp. 96-109, 2014.

[11] R. Pahl and J. Cohen, "Effects of fatigue on the GP zones in Al-Zn alloys," Metallurgical and Materials Transactions A, vol. 15, no. 8, pp. 1519-1529, 1984.

[12] W. Han, A. Vinogradov, and C. Hutchinson, "On the reversibility of dislocation slip during cyclic deformation of Al alloys containing shear-resistant particles," Acta Materialia, vol. 59, no. 9, pp. 3720-3736, 2011.

[13] A. Lervik et al., "Atomic structure of solute clusters in Al–Zn–Mg alloys," Acta Materialia, vol. 205, p. 116574, 2021.

[14] H. Löffler, I. Kovács, and J. Lendvai, "Decomposition processes in Al-Zn-Mg alloys," Journal of Materials Science, vol. 18, no. 8, pp. 2215-2240, 1983.

[15] A. Lervik, C. D. Marioara, M. Kadanik, J. Walmsley, B. Milkereit, and R. Holmestad, "Precipitation in an extruded AA7003 aluminium alloy: Observations of 6xxx-type hardening phases," Materials & Design, vol. 186, p. 108204, 2020.

[16] T. J. Prosa and D. J. Larson, "Modern focused-ion-beam-based site-specific specimen preparation for atom probe tomography," Microscopy and Microanalysis, vol. 23, no. 2, pp. 194-209, 2017.

[17] T. F. Kelly and M. K. Miller, "Atom probe tomography," Review of scientific instruments, vol. 78, no. 3, p. 031101, 2007.

[18] "Atom Probe Tomography (APT) - Department of Materials Science and Engineering - NTNU." https://www.ntnu.edu/ima/research/apt (accessed.

[19] B. Gault et al., "Advances in the calibration of atom probe tomographic reconstruction," Journal of Applied Physics, vol. 105, no. 3, p. 034913, 2009.

[20] J. M. Hyde et al., "Analysis of radiation damage in light water reactors: comparison of cluster analysis methods for the analysis of atom probe data," Microscopy and Microanalysis, vol. 23, no. 2, pp. 366-375, 2017.

[21] W. Lefebvre, F. Vurpillot, and X. Sauvage, Atom probe tomography: put theory into practice. Academic Press, 2016.

[22] C. Hatzoglou, B. Radiguet, F. Vurpillot, and P. Pareige, "A chemical composition correction model for nanoclusters observed by APT-Application to ODS steel nanoparticles," Journal of Nuclear Materials, vol. 505, pp. 240-248, 2018.

[23] R. Lawitzki, P. Stender, and G. Schmitz, "Compensating local magnifications in atom probe tomography for accurate analysis of nano-sized precipitates," Microscopy and Microanalysis, vol. 27, no. 3, pp. 499-510, 2021.

[24] F. Vurpillot, A. Bostel, and D. Blavette, "Trajectory overlaps and local magnification in three-dimensional atom probe," Applied Physics Letters, vol. 76, no. 21, pp. 3127-3129, 2000.

[25] F. Vurpillot and C. Oberdorfer, "Modeling atom probe tomography: A review," Ultramicroscopy, vol. 159, pp. 202-216, 2015.

[26] E. A. Marquis and J. M. Hyde, "Applications of atom-probe tomography to the characterisation of solute behaviours," Materials Science and Engineering: R: Reports, vol. 69, no. 4-5, pp. 37-62, 2010.

[27] R. Ivanov, A. Deschamps, and F. De Geuser, "A combined characterization of clusters in naturally aged Al–Cu–(Li, Mg) alloys using small-angle neutron and X-ray scattering and atom probe tomography," Journal of Applied Crystallography, vol. 50, no. 6, pp. 1725-1734, 2017.

[28] H. Zhao, B. Gault, D. Ponge, D. Raabe, and F. De Geuser, "Parameter free quantitative analysis of atom probe data by correlation functions: Application to the precipitation in Al-Zn-Mg-Cu," Scripta Materialia, vol. 154, pp. 106-110, 2018.

[29] F. De Geuser, W. Lefebvre, and D. Blavette, "3D atom probe study of solute atoms clustering during natural ageing and pre-ageing of an Al-Mg-Si alloy," Philosophical Magazine Letters, vol. 86, no. 04, pp. 227-234, 2006.

[30] Y.-g. Liao, X.-q. Han, M.-x. Zeng, and M. Jin, "Influence of Cu on microstructure and tensile properties of 7XXX series aluminum alloy," Materials & Design, vol. 66, pp. 581-586, 2015.

[31] R. A. Karnesky, C. K. Sudbrack, and D. N. Seidman, "Best-fit ellipsoids of atom-probe tomographic data to study coalescence of γ′(L12) precipitates in Ni–Al–Cr," Scripta Materialia, vol. 57, no. 4, pp. 353-356, 2007.

[32] R. K. Marceau, A. de Vaucorbeil, G. Sha, S. P. Ringer, and W. J. Poole, "Analysis of strengthening in AA6111 during the early stages of aging: Atom probe tomography and yield stress modelling," Acta Materialia, vol. 61, no. 19, pp. 7285-7303, 2013.

[33] F. De Geuser and B. Gault, "Metrology of small particles and solute clusters by atom probe tomography," Acta Materialia, vol. 188, pp. 406-415, 2020.

[34] F. D. Geuser and W. Lefebvre, "Determination of matrix composition based on solute-solute nearest-neighbor distances in atom probe tomography," Microscopy research and technique, vol. 74, no. 3, pp. 257-263, 2011.

[35] A. Deschamps and Y. Brechet, "Influence of predeformation and ageing of an Al–Zn–Mg alloy—II. Modeling of precipitation kinetics and yield stress," Acta Materialia, vol. 47, no. 1, pp. 293-305, 1998.

[36] I. Zuiko and R. Kaibyshev, "Deformation structures and strengthening mechanisms in an Al-Cu alloy subjected to extensive cold rolling," Materials Science and Engineering: A, vol. 702, pp. 53-64, 2017.

[37] E. Thronsen et al., "Studying GPI zones in Al-Zn-Mg alloys by 4D-STEM," Materials Characterization, p. 111675, 2021.

[38] A. Deschamps, Y. Bréchet, and F. Livet, "Influence of copper addition on precipitation kinetics and hardening in Al–Zn–Mg alloy," Materials Science and Technology, vol. 15, no. 9, pp. 993-1000, 1999.

[39] K. Watanabe, K. Matsuda, S. Ikeno, T. Yoshida, and S. Murakami, "TEM Observation of precipitate structures in Al-Zn-Mg alloys with additions of Cu/Ag," in Materials Science Forum, 2014, vol. 794: Trans Tech Publ, pp. 985-987.

Paper II

Materials & Design 222 (2022) 111026

Contents lists available at ScienceDirect

Materials & Design

journal homepage: www.elsevier.com/locate/matdes

Precipitation, mechanical properties and early slant ductile fracture in cyclic and naturally aged Al-Zn-Mg(-Cu) alloys

Sohail Shah [a,*], Akash Gopal [a], Elisabeth Thronsen [b], Constantinos Hatzoglou [a], Bjørn Holmedal [a]

[a] Department of Materials Science and Engineering, Norwegian University of Science and Technology (NTNU), 7491 Trondheim, Norway
[b] Department of Physics, Norwegian University of Science and Technology (NTNU), N-7491 Trondheim, Norway

HIGHLIGHTS

- The implications of cyclic ageing on strength, ductility and more importantly fracture has been investigated.
- Early shear/slant fractures are reported to occur for cyclic and naturally aged plate alloys.
- Plate materials with an underaged microstructure are more prone to such slant fracture as compared to axisymmetric materials.

GRAPHICAL ABSTRACT

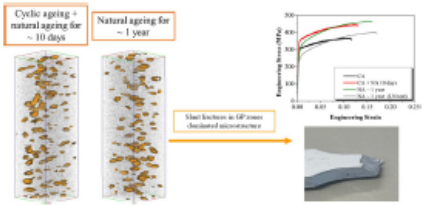

ARTICLE INFO

Article history:
Received 14 June 2022
Revised 25 July 2022
Accepted 2 August 2022
Available online 5 August 2022

Keywords:
Aluminum alloys
Atom probe tomography (APT)
Slant fractures
Cyclic ageing
Natural ageing

ABSTRACT

Natural and artificial ageing treatments are compared with ageing by cyclic deformation at room temperature. Atom probe tomography and transmission electron microscopy revealed that a fine distribution of GP-zones, was responsible for the strength after cyclic ageing. Ten days further natural ageing allowed these early-stage clusters to grow into more stable ones, thereby improving the mechanical response. This resulted in similar tensile strength and uniform elongation as for the peak aged condition by artificial ageing. It was found that fracture of cyclic aged samples occurred earlier, in the form of a ductile slant shear fracture without necking in advance. In all cases, the slant fracture started at about the same point as reaching maximum strength, i.e., at the uniform limit. However, by an artificial ageing treatment after the cyclic hardening treatment, an ordinary necking behavior was seen, similar as for the peak aged samples. Natural aged samples had similar GP-zones as the cyclic hardened ones, and the same slant fracture mode, indicating that the precipitation structure controls the fracture type. Similar behavior was observed for two different Al-Zn-Mg alloys, with and without copper.

1. Introduction

Aluminum alloys aged by precipitation hardening have a good combination of strength, formability, corrosion resistance and low weight, making them attractive as engineering materials. The alloying elements in supersaturated solid solution after solution heat treatment and quenching, forms a high number of nano-sized precipitates that act as obstacles for dislocation movement and thereby strengthen the alloy. In Al-Zn-Mg alloys, similar high strength can be obtained either by natural ageing (NA) for several months or by artificial ageing (AA) for some hours [1].

After quenching, the density of vacancies is also supersaturated. The vacancies play an important role for the precipitation. They are required to facilitate substitutional diffusion of the solute atoms and play a role for the cluster nucleation. In general, diffusion,

* Corresponding author.
E-mail address: sohail.shah@ntnu.no (S. Shah).

https://doi.org/10.1016/j.matdes.2022.111026
0264-1275/

Paper II

Precipitation, mechanical properties and early slant ductile fracture in cyclic and naturally aged Al-Zn-Mg(-Cu) alloys

Sohail Shah[a*], Akash Gopal[a], Elisabeth Thronsen[b], Constantinos Hatzoglou[a], Bjørn Holmedal[a]

[a]*Department of Materials Science and Engineering, Norwegian University of Science and Technology (NTNU), 7491 Trondheim, Norway*

[b]*Department of Physics, Norwegian University of Science and Technology (NTNU), N-7491 Trondheim, Norway*

Abstract

Natural and artificial ageing treatments are compared with ageing by cyclic deformation at room temperature. Atom probe tomography and transmission electron microscopy revealed that a fine distribution of GP-zones, was responsible for the strength after cyclic ageing. Ten days further natural ageing allowed these early-stage clusters to grow into more stable ones, thereby improving the mechanical response. This resulted in similar tensile strength and uniform elongation as for the peak aged condition by artificial ageing. It was found that fracture of cyclic aged samples occurred earlier, in the form of a ductile slant shear fracture without necking in advance. In all cases, the slant fracture started at about the same point as reaching maximum strength, i.e., at the uniform limit. However, by an artificial ageing treatment after the cyclic hardening treatment, an ordinary necking behavior was seen, similar as for the peak aged samples. Natural aged samples had similar GP-zones as the cyclic hardened ones, and the same slant fracture mode, indicating that the precipitation structure controls the fracture type. Similar behavior was observed for two different Al-Zn-Mg alloys, with and without copper.

Keywords

Aluminum alloys, Atom probe tomography (APT), Slant fractures, Cyclic ageing, Natural ageing

1. Introduction

Aluminum alloys aged by precipitation hardening have a good combination of strength, formability, corrosion resistance and low weight, making them attractive as engineering materials. The alloying elements in supersaturated solid solution after solution heat treatment and quenching, forms a high number of nano-sized precipitates that act as obstacles for dislocation movement and thereby strengthen the alloy. In Al-Zn-Mg alloys, similar high strength can be obtained either by natural ageing (NA) for several months or by artificial ageing (AA) for some hours [1].

After quenching, the density of vacancies is also supersaturated. The vacancies play an important role for the precipitation. They are required to facilitate substitutional diffusion of the solute atoms and play a role for the cluster nucleation. In general, diffusion, and hence precipitation kinetics, are faster at elevated temperatures, as the equilibrium concentration of vacancies and their diffusivity increases with temperature [2]. However, the driving force for nucleation increases with higher supersaturation at lower temperatures [3]. The optimal combination of temperature and time for the conventional precipitation ageing, is always a compromise between these two factors.

Recently, Sun *et al.* [2] demonstrated that aluminum alloys can be processed at room temperatures with cyclic plasticity, providing strength and uniform elongation equivalent or slightly exceeding the peak aged (PA) condition. The repetitive cyclic deformation leads to dragging of jogs on dislocations, which produces vacancies [4] and thereby facilitates local diffusion at room temperature.

With precipitation and deformation occurring simultaneously, the process becomes more complex. The plastic straining will influence the precipitation. In general, nucleation and growth are accelerated as a result of the local vacancy generation by glide of heavily jogged dislocations during plastic deformation [5, 6]. As argued by Sun *et al.* [2] the repeated shearing of the clusters might prevent their early growth and enable an increased number of nuclei to form. The dislocations may act as heterogeneous nucleation sites for precipitates, which was reported by Deschamps *et al.* [7] for cases of artificial ageing of a pre-strained Al-Zn-Mg alloy. Dynamic strain ageing occurs in Al-Zn-Mg alloys, causing heterogenous plastic deformation and involving local substitutional pipe diffusion of Zn and Mg around temporarily stored dislocations [8-10].

Hutchinson *et al.* [11] studied the room temperature cyclic deformation behavior of underaged and peak aged Al-Zn-Mg-Cu alloys for different plastic strain amplitudes, strain rates and number of cycles. Based on small angle X-ray scattering measurements, they concluded that the nucleation rate of GP zones formed during cyclic deformation remained constant. Based on their characterization, they vaguely suggested that the size of the GP zones did not increase significantly during the cyclic treatment, suggesting continuous nucleation and restricted growth of the GP-zones during cyclic deformation.

Even though it takes months of storage at room temperature, NA can in some cases be an interesting alternative for achieving the desired strength for Al-Zn-Mg alloys. Also, NA plays an important role for the welding properties [12]. Interestingly, higher work hardening, higher uniform elongation and higher uniform strength, as well as a yield strength similar to the artificially peak aged condition, was reported to be obtained by NA of an Al-Zn4.8-Mg1.4 alloy [13]. However, in some cases, an early shear fracture has been reported to occur, rather than ordinary necking in tensile tests of naturally aged alloys [14-16]. Chung et al. [15] found for an as quenched 7075 alloy, that the shear fracture was replaced by ordinary necking instability at low temperature tests and suggested that the reason for shear fractures may be the dynamic strain ageing phenomenon, associated with the Portevin-Le Chatelier effect in this

type of alloys [17]. The early fracture may make the NA alloy less suited for applications in energy absorbing safety parts, e.g., in automotive applications.

The specific purpose of this study is to investigate the effect of systematic cyclic ageing (CA) at different frequencies on strengthening of two Al-Zn-Mg(-Cu). Most of the investigations are done on the 7046 alloy, however some experiments on a copper [18] free leaner 7003 alloy have also been done. The mechanical properties and work hardening imparted to the alloy as a

result of the CA, are studied by tensile testing. Atom probe tomography has been employed to characterize the clusters formed after the CA. Special emphasis has been given to the type of fracture causing these samples to fail, which is characterized by light optical and scanning electron microscopy.

2. Experimental

A commercial 7046 and 7003 alloy with composition Al-6.5Zn-1.3Mg-0.3Cu-(Fe,Zr,Si) and Al-5.7Zn-0.7Mg-0.01Cu-(Fe,Zr,Si) respectively measured by spectrograph analysis, was received from Benteler automotive as extruded 6 mm thick plates. The thermomechanical treatment performed in this study involves 40 minutes of solution heat treatment (SHT) at 480 ^{o}C in a salt bath followed by a drop quench in cold water. This is done to retain a complete solid solution. Then the samples are strengthened by either NA, AA or CA treatments.

Samples with the tensile axis along the extrusion direction were machined with dimensions suited for CA tests. They had a square cross section of 6x6 mm^2 and a short uniform length of 12 mm, to avoid buckling during the compression part of the cyclic loading. Detailed information about the sample geometry can be found in the supplementary information. Selected samples were grounded and polished for micro hardness testing, using a 1000 gf Vickers indenter with 5 parallel readings for each condition.

The cyclic loading experiments were designed based on the study in reference [11] and [2]. During each cycle, the engineering stress σ was varied sinusoidally through tension and compression by a prescribed stress amplitude σ_a. The stress amplitude was increased systematically from cycle to cycle. At cycle number n, it was prescribed as

$$\sigma_n = \sigma_0 + (\sigma_t - \sigma_0)\sqrt{\frac{n}{N}} \tag{29}$$

Here σ_0 is approximately the initial yield stress of the material (after solution heat treatment), σ_t is the targeted strength (close to the initial yield stress of the conventional PA sample), and N is the total number of cycles, applied to reach the desired stress. Hence, the CA tests were stress controlled, using an INSTRON 250KN with a servo-hydraulic test system. All tests were carried out at room temperature.

Strain measurements during the cyclic experiments were carried out using a digital image correlation [19] system developed by Fagerholt [20]. It consists of a high-speed CCD camera

with a resolution of 1280×1024 pixels capturing digital images at a rate ranging from 1 to 50 frames per second. The rate was varied according to the frequency of the cycle sampled in each test. The samples were sprayed with a white background on the gauge area, followed by decoration with a black speckle pattern. The speckles are used by the DIC software to track the strain during deformation. This method of calculating strain is accurate and provides strain field maps to check for any strain localization.

A virtual extensometer for the tensile test was obtained from the DIC processing, by tracking the length change between two selected points at the specimen surface, having an initial distance $l_0 = 12mm$. All plots are based on the nominal tensile stress and the nominal strain calculated by this virtual extensometer.

The sinusoidal load cycle n consists of first a maximum nominal tensile stress σ_{max}^{n}, then a minimum nominal compression stress σ_{min}^{n}. Each cycle contributes to two stress ranges: $\Delta\sigma^{2n-1}$ from the maximum to the minimum stress, and $\Delta\sigma^{2n}$ from the minimum to the maximum stress of the next cycle.

$$\Delta\sigma^{2n-1} = \sigma_{max}^{n} - \sigma_{min}^{n}, \qquad \Delta\sigma^{2n} = \sigma_{max}^{n+1} - \sigma_{min}^{n} \tag{30}$$

The corresponding nominal strain ranges Δe^{2n-1} and Δe^{2n} are calculated as

$$\Delta e^{2n-1} = e_{max}^{n} - e_{min}^{n}, \qquad \Delta e^{2n} = e_{max}^{n+1} - e_{min}^{n} \tag{31}$$

The corresponding plastic part of the strain ranges Δe_p^{2n-1} and Δe_p^{2n} were computed as

$$\Delta e_p^{2n-1} = \Delta e^{2n-1} - \frac{\Delta\sigma^{2n-1}}{E}, \qquad \Delta e_p^{2n} = \Delta e^{2n} - \frac{\Delta\sigma^{2n}}{E} \tag{32}$$

Where E is the elastic modulus. The first onloading Δe_p^1 requires special treatment

$$\Delta e_p^1 = e_{max}^{n} - \frac{\sigma_{max}^{1}}{E} \tag{33}$$

The cumulative plastic strain is defined as e_{cp}^{i} at each extrema, as

$$e_{cp}^{i} = \sum_{k=1}^{i} \Delta e_p^k \tag{34}$$

Hence, for each cycle n, the cumulative plastic strain is recorded at the maximum and minimum points, at $i = 2n - 1$ and $i = 2n$, respectively.

The grain structure was investigated using an optical microscope. The sample surface was first grinded on progressively finer grades of SiC paper up to 4000 mesh and then the surface was polished using 3 μm and 1μm diamond paste. Finally, the samples were chemically polished using active oxide suspension (OP-U) to obtain a smooth and scratch free surface. The grain structure was revealed by anodizing the polished samples using 5% fluoroboric acid (HBF4)

for 45 seconds at an applied voltage of around 12 V at ambient temperature. The samples were examined in an optical microscope with polarized light. The distribution of the intermetallic particles and the fracture surface were studied using the scanning electron microscopy (SEM).

Atom Probe Tomography (APT) samples were prepared using the FEI Helios Focused Ion Beam (FIB) using Ga^+ as the ion source. Electropolishing was attempted as it was the preferred methodology, though the CA samples fractured. Silicon microtip coupons provided by Cameca

Inc. were used to deposit the lamella and sharpened to around 100 nm to produce the APT needles. The specimens were sharpened by using a 16 kV Ga^+ beam followed by a 2 KV final cleanup step to remove higher concentrations of implanted high-energy Ga ions. The APT sample with NA for 1 year was prepared following a two-step standard electropolishing process [21], since unlike the CA samples, had high yield in the preferred electropolishing method.

All APT analyses were carried out using a Local Electrode Atom Probe (LEAP) 5000XS by Cameca Instruments Inc. This is a straight flight path instrument with a detection efficiency of 80%. All samples were run at 25 K base temperature in laser mode with a detection rate of 0.5%. Depending on the sample geometry, it was calibrated in the range of 70-100 pJ. A pulse rate of 250 kHz was used for all the samples. Datasets, ranging from 50- 150 million ions, were collected from the samples. The reconstructions and the post processing analyses were carried out using the Integrated Visualization and Analysis Software (IVAS) by Cameca Instruments Inc and the Norwegian Atom Probe App [22]. The latter has been developed in Norwegian University of Science and Technology (NTNU) by C. Hatzoglou and is an open access software dedicated to APT data treatment [23]. The estimation of the reconstruction parameters was carried out using the structural information, according to the protocols of Gault et al. [24]. The size of clusters is defined based on the $Extent_z$ parameter as explained in [25] and the number densities are measured by taking the ratio of the number of clusters identified to the number of atoms in the dataset. This is done by also taking into account detection efficiency of the APT and the average atomic volume. The uncertainty is calculated by dividing the number density by the square root of the total number of clusters.

The TEM samples were prepared by first grinding down bulk samples to ~100 μm and punching out to 3 mm disks. The specimens were subsequently electropolished in a Struers TenuPol-5 machine using an electrolyte mixture consisting of 1/3 HNO_3 and 2/3 CH_3OH. The applied voltage was 20 V and the liquid was kept at -25±5°C. An image and probe corrected JEOL JEM-ARM200CF microscope operated at 200 kV was used to collect the high-angle annular dark-field scanning TEM (HAADF-STEM) images. The convergence semi-angle was 27 mrad, while the inner-and outer semi-angles were 67 and 155 mrad, respectively. The high-frequency noise in the images was reduced using an inverse fast Fourier transform (FFT) filtering by applying a low-pass mask on the FFT of approximately 6.7 nm^{-1} and then taking the inverse FFT of the masked FFT. The selected area diffraction patterns (SADP) and bright-field (BF) images were acquired on a JEOL 2100 microscope operated at 200 kV.

3. Results

CA of 7046 alloy was carried out at different frequencies to examine the plastic strain accumulation within the samples during the tension-compression cycles. Times ranging from 5 sec/cycle to 120 sec/cycle were used for 420 cycles.

3.1 CA and Hardness

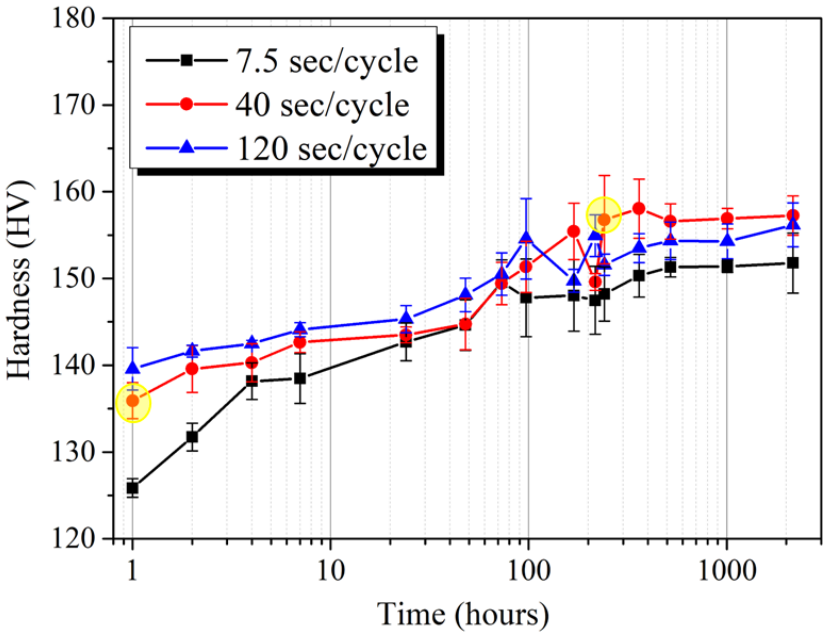

Figure 29. Hardness measurements for 7046 alloy at room temperature as a function of time after quenching. The different time/cycle from the CA used here are: 7.5 sec/cycle, 40 sec/cycle, and 120 sec/cycle. The yellow circles indicate the conditions selected for the microstructural analyses.

The stress amplitude (σ_0) for the first cycle was very close to the yield stress of the material in the solutionized state (~120 MPa) and the targeted strength (σ_{max}) was 370 MPa. Higher strengths (σ_{max}) were tested but resulted in fracture during the CA. To limit the amount of damage being inflicted onto the sample, the final strength was chosen slightly lower than the yield strength of the PA sample. The optimization of σ_{max} is shown in detail in the supplementary information. After this initial optimization study, a combination of 420 cycles and σ_{max} =370 MPa were chosen.

To check the stability of the strength of the samples immediately after their CA treatment, hardness tests were carried out afterwards on the samples that had been cyclically aged at 7.5, 40 and 120 sec/cycle, respectively. As shown in Figure 29, the hardness increases sharply during the first few hours after the cyclic ageing and then gradually less until around 10 days. After around 10 days, the hardness from the CA region has saturated.

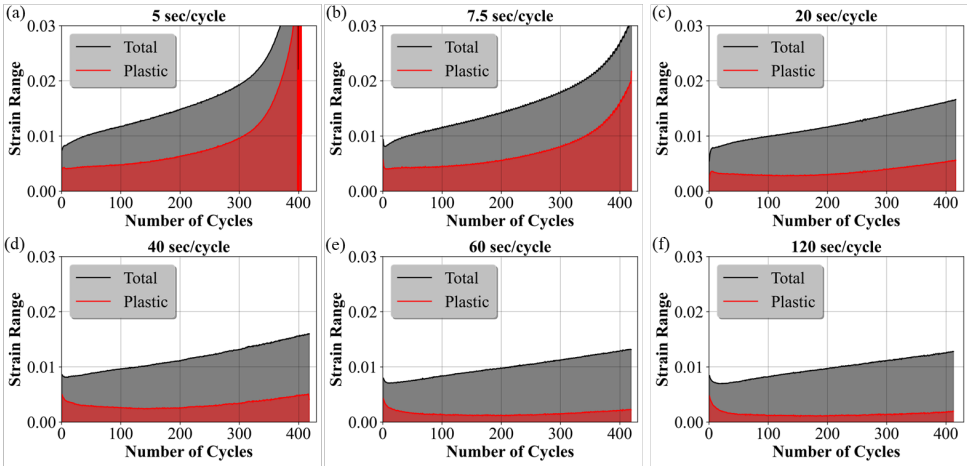

Figure 30. Measured total strain range Δe and plastic strain range Δe_p during CA experiments of 7046 alloy at time/cycle ranging from (a) 5 sec/cycle - (f) 120 sec/cycle, as indicated

The strain was measured by DIC during each cyclic ageing test. The plastic strain range Δe_p was calculated at two points per cycle according to Equation (32). As can be seen from Figure 30, the highest frequencies lead to the largest amount of plastic strain in each cycle. The fastest, 5 sec/cycle sample fractured before completing the 420 cycles. This is evident from Figure 30(a), where the plastic strain increases rapidly, before ending in a fracture. From Figure 30, the 60 and 120 sec/cycle tests with the lowest frequencies and the longest time spent for each cycle, went through the least amount of plastic strain range during each cycle.

In Figure 31, the square of the stress amplitude increases linearly with the cumulative plastic strain, similar as earlier reported by Hutchinson et al. [11]. However, for the 5 and 7.5 sec/cycle conditions, the curve is no longer linear at cumulative strains larger than around 2.

Optimizing the frequency for better mechanical response is a trade-off between imposing the sufficient amount of plastic deformation that is required for the cyclic hardening to occur and limiting the plastic strain to avoid too much damage during the plastic deformation, potentially leading to fracture. The 40 sec/cycle sample gave the best mechanical response, as seen from Figure 30d.

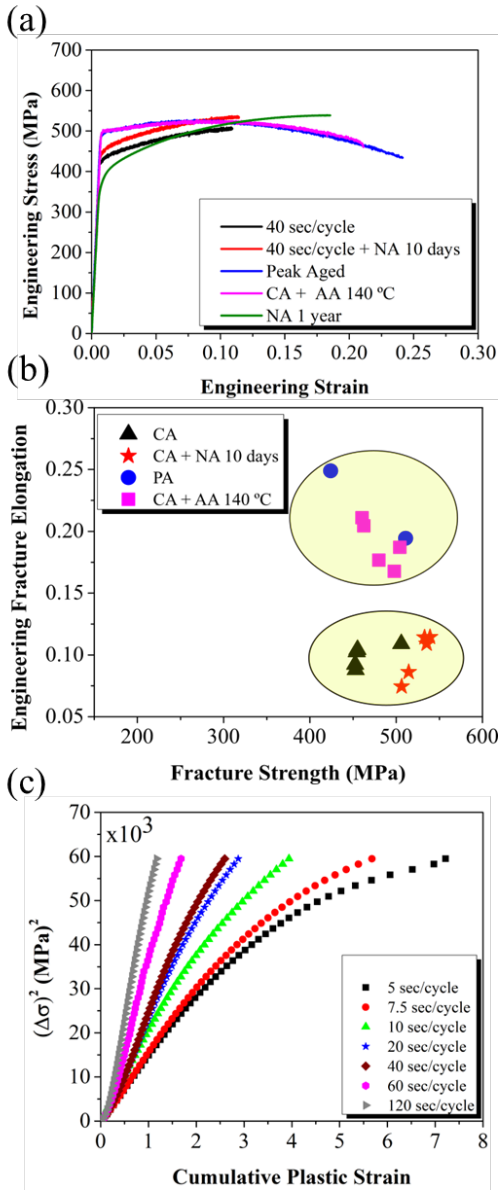

Figure 31. (a) Mechanical response of the 7046 alloy with stress-strain plots showing a comparison of CA, NA, PA and CA+ AA. Fracture strengths for the corresponding stress strain plots are summarized in (b). (c) the square of the stress amplitude is plotted as a function of the cumulative plastic strain, for all tests, ranging from 5 sec/cycle to 120 sec/cycle. The nominal strain rate of the tensile tests was $1.4 \cdot 10^{-3}$.

3.2 Mechanical testing of the 7046 alloy

Paper II

Tensile tests were carried out immediately after the CA experiments and after 10 days of further storage at room temperature. To confirm any statistical fluctuations within the strength measurements, 5 tests were performed for each of the optimized conditions. Tensile tests for the PA condition and for a specimen with NA for one year are also included in Figure 31. for comparison. The yield stress was larger for the PA condition than for any other condition, while the NA alloy had the largest uniform strain but the lowest YS as seen in Table 7.

The tensile tests of 7046 alloy done immediately after the cyclic treatment did not reach the initial yield stress (YS) of the PA sample but showed about the same uniform elongation (408 vs 596 MPa and 9.6% vs 10%). Nor the samples treated by CA+ NA 10 days of reached the YS of the PA condition (447 vs 496 MPa). However, as can be seen from Figure 31a and Table 7, all cyclic aged samples with 10 days of subsequent storage consistently surpassed the UTS of the PA sample, with a 12% increase in the UTS from 475 MPa ± 12 MPa to 532 MPa ±10 MPa, as compared to without the 10 days of storage. The maximum strength reached after 10 days is similar for all frequencies tested and similar to the one-year NA condition. The average yield strength increased from 408 MPa ±8 MPa to 446 MPa ± 2.9 MPa after 10 days of storage, a 9.4% increase in YS

For both 7003 and 7046 alloy, the PA sample had a significant amount of necking before fracture occurred, while the cyclic aged samples fractured before reaching the maximum load. The fracture, as observed from the transverse plate direction, consisted of a 45° plane fracture surface without any visual signs of necking. To investigate if the shear fracture was due to damage evolution during the cyclic loading, the CA samples were afterwards artificially aged at 140ºC for 8 hours and then tensile tested. Interestingly, the PA condition and CA+ AA 140ºC sample had similar strengths and similar normal necking behavior, as seen by the fracture strengths from Figure 31b for 7046 alloy and Figure 32(b) for 7003 alloy. The cumulative plastic strain evolution of the 7046 alloy is shown in Figure 3c for all cases, as calculated from Equation (34). Almost all the curves are nearly straight lines, except for the samples run at lowest time per cycle (5 and 7.5 sec/cycle), for which fracture occurred during the CA. The true fracture strains measured by inspecting the projected area of the fracture surface for all conditions, is listed in the supplementary information.

Table 7. Measured tensile properties under different test conditions for 7046.82. All measurements are based on the standard deviation of 5 values

	Yield Strength (MPa)	UTS (MPa)	Fracture Strength (MPa)	Elongation at Uniform Strain (%)	Elongation at fracture (%)
CA	408 ± 8	475 ± 17	464 ± 23	9.6 ± 1	10 ± 0.9
CA + NA 10 days	447 ± 3	532 ± 10	526 ± 14	9.6 ± 1.8	10 ± 1.8
NA 1 year	364	535	531	18.3	18.3
Peak Aged	496	530	467	10	22
CA+ AA 140 °C	503 ± 6	532 ± 9	481 ± 20	9.4 ± 0.7	18 ± 3.3

3.3 Mechanical testing of 7003 alloy

To rule out any role played by Cu in causing the early shear fractures, similar tensile CA processing and corresponding tensile tests as for the 7046 alloy, were performed on a Cu free 7003 alloy. The resulting tensile tests are shown in Figure 32a for the samples fractured in slant mode without pronounced necking. An identical trend is seen as compared to the 7046 alloy, where the CA and CA + 10 days sample undergo the same type of early shear fractures near the point where the stress reaches the UTS, while the PA and CA + PA and a NA 1 year sample was Peak aged, all underwent necking behavior prior to fracture as seen in Figure 32b. For this alloy the CA+10 days specimens reached a similar YS as the PA samples, while the NA for one year reached both a larger UTS and a larger uniform strain than any of the others.

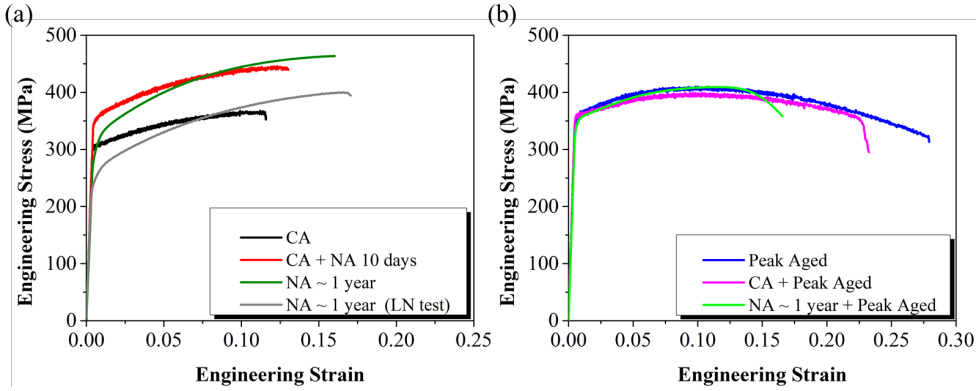

Figure 32. Tensile stress-strain curves of the 7003 alloy for all samples that had (a) slant fractures and (b) fracture in the neck. The strain rate of the tensile tests was $1.4 \cdot 10^{-3}$. LN is liquid nitrogen test (-196ºC)

3.4 TEM and APT of the 7046 alloy

To help understand the origin of the strength gained by CA, APT and HRTEM were used to characterize the microstructure. Detailed quantitative microstructural analysis can be found in Ref [25]. Some additional HAADF-STEM images and SADPs from the 7046 alloy in the CA, CA + 10 days and NA 1 year are provided in Appendix B. Consistently with the work in Ref. [25], these additional images provide evidence that the same type of clusters and GP zones are present in the three conditions, mainly GPI zones and smaller clusters. Microstructural investigations with BF-TEM revealed dislocations that are present both in CA and CA + NA 10 days condition, as seen in Figure 33(a and b).

In addition, the NA 1 year condition has been investigated by APT to compare the chemistry of the GP zone evolution. As seen from Table *8* which is based on cluster identification, the concentrations of Zn and Mg in the clusters do not change from CA to 10 days of storage after

CA, while the size increases but is still smaller than after 1 year of NA. Furthermore, the number density increased during the 10 days of storage after CA. NA for 1 year showed that the number density is consistently lower than the CA condition.

Table 8. Cluster analysis data for APT datasets shown in Figure 5.

Condition	Composition (At%)	Number Density ($10^{24}/m^3$)	Size (nm)	Zn/Mg Ratio
CA	Mg- 7.43 ± 1.45 Zn- 12.17 ± 1.69 Cu- 0.39 ± 0.21	1.81 ± 0.18	1.12 ± 0.52	1.64 ± 0.71
CA + NA 10 days	Mg- 8.03 ± 0.66 Zn- 12.58 ± 1.21 Cu- 0.24 ± 0.11	3.15 ± 0.23	1.50 ± 0.89	1.58 ± 0.48
NA 1 year	Mg- 7.98 ± 0.33 Zn- 11.55 ± 0.48 Cu- 0.29 ± 0.07	2.29 ± 0.61	1.85 ± 0.88	1.46 ± 0.17

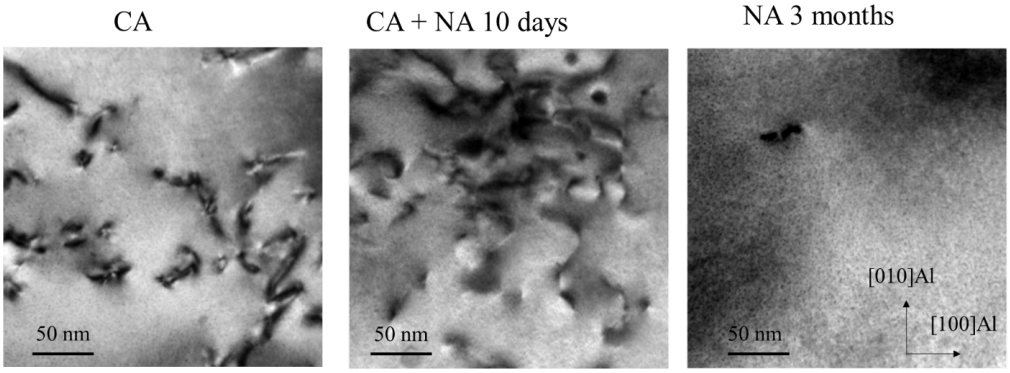

Figure 33. BF-TEM images of 7046 (a) CA, (b) CA + NA 10 days and (c) NA 1 year conditions showing the presence of dislocations in the cyclically aged conditions.

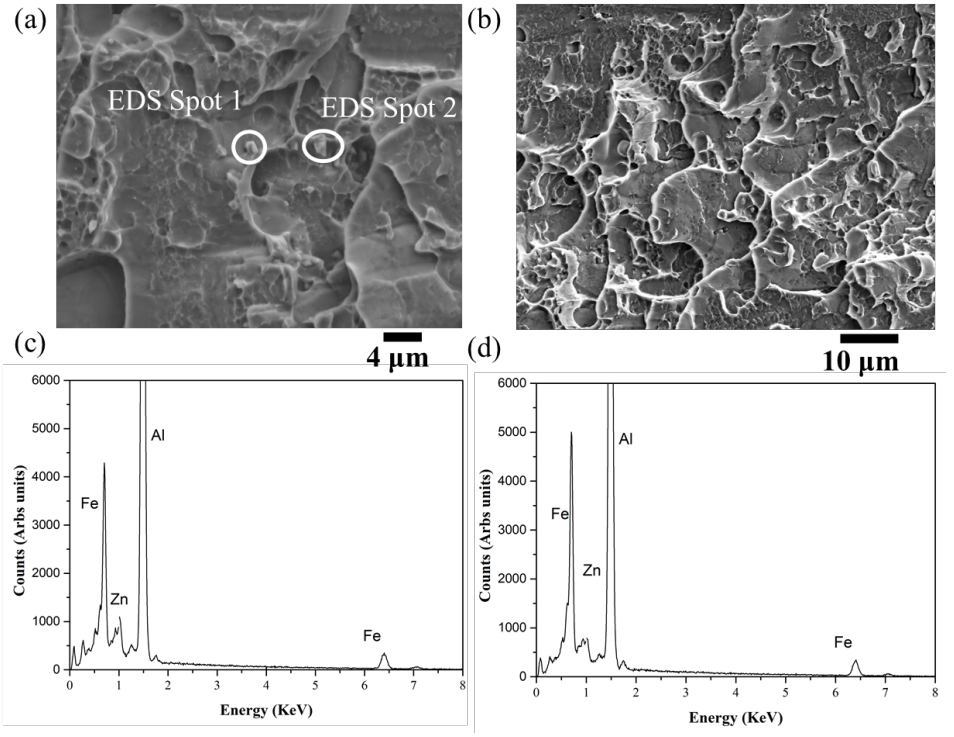

Figure 34. (a) SEM micrograph of the dimples seen on the fracture surface of the 40sec/cycle sample for 7046 alloy. (b-d) showing the EDS spectra of the iron rich intermetallic particles.

3.5 Fracture Surfaces

The fracture surfaces, after failure of the cyclic aged samples, were inspected using a scanning electron microscope (SEM). From a macroscopic level, the fracture appears to be in a shear mode making an approximately 45° angle to the transverse axis of the plate specimen. This was the case for all cyclically aged samples of 7046 and 7003 alloy (supplementary information) that were tested in uniaxial tension until fracture. A high number of dimples were seen, with particles inside many of them. Energy dispersive spectroscopy (EDS) of these particles, as shown in Figure 34 for 7046 alloy, revealed mainly iron rich particles. Some regions had a high density of dimples, but also flat regions without dimples were present, as seen in Figure 34(b).

Optical micrographs, taken from the transverse direction, reveal non-recrystallized grains that are elongated in the extrusion direction, as shown in Figure 35(b) for the case of 7046 alloy (7003 supplementary information). An overview of the fracture mode in shear is provided in Figure 35(a). On a finer scale in Figure 35, near the fracture surface, it can be seen from the bending of the grain boundaries close to the fracture surface, that most of the grains did undergo shear deformation near the fracture surface just before fracture occurred, indicating a ductile

fracture mode. There is a presence also of grains that abruptly end without visible deformation, indicating some cases of grain boundary fracture, though not the dominating mode.

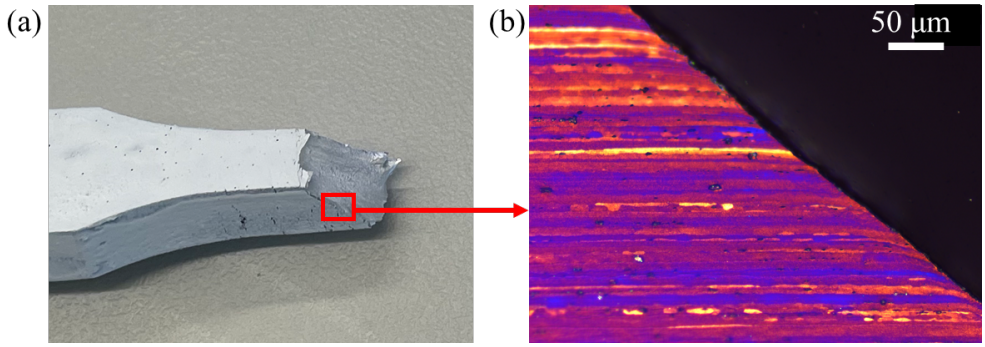

Figure 35. (a) Optical micrograph of the shear fracture location after a uniaxial tensile test of 7046 alloy. (b) Higher magnification optical micrograph of the grains ending at the shear fracture, taken from the transverse direction.

4. Discussion

4.1 Parameter optimizations for CA of 7046 alloy

Optimization of the CA treatment involved 3 main parameters: frequency, target stress and the number of cycles. Higher frequencies led to a large amount of cumulated plastic strain. The back and forward glide of jog-dragging dislocations is assumed to generate vacancies locally, but when the frequency of the load is high, there seems not to be enough time for the vacancies that are generated to contribute to the clustering. With lower frequencies, the measured amount of cumulative plastic strain was reduced, offering the time needed for the local solute diffusion that is required to form clusters. The minimum amount of plastic strain accumulation was obtained with the lowest frequencies (0.016 Hz, 0.008 Hz). These gave very similar strength as the 0.025 Hz sample, which therefore was chosen as the optimum condition to minimize the time spent during the cyclic ageing.

4.2 Microstructure and mechanical response of 7046 alloy

From the series of mechanical tests done after CA and 10 days of storage (NA), higher strengths are reached, while maintaining similar elongations, within the statistical measuring variation, which is in good agreement with what was reported by Sun *et al*. [2]. The cyclic plasticity forms dislocations as well as excess vacancies [26]. This speeds up the kinetics of supersaturated elements in the matrix, forming a high number density of solute clusters [2] (of the order of $10^{24}\ m^{-3}$), which are seen in atom probe immediately after the CA. The increase in strength is attributed to the clusters, which are found to be extremely fine and uniformly distributed after the CA.

Based on extensive SAXS and APT investigations, Hutchinson et al. [11] concluded that the back and forward gliding dislocations during the CA repetitive shears the clusters and thereby keeps their size small and maintain their nucleation rate. However, there are still excess vacancies present after finishing the cyclic loading, which for a while enable faster local

diffusion of elements in substitutional solid solution during the subsequent storage and enhance further growth of the small clusters present after the cyclic ageing. The increased size of the clusters makes them more difficult to cut by gliding dislocations and hardens the material. As a result, the hardness increases most rapidly during the first few hours of storage after the cyclic ageing treatment. In other words, the clusters immediately after CA grow further during storage. However, after 10 days of NA after the CA, the further strength increase is very slow.

From the APT and TEM analysis of the alloy after 10 days of storage, a combination of larger clusters along with smaller ones similar to those seen immediately after CA, are observed. This may indicate that either cluster nucleation is still occurring, resulting in new small clusters, or there is a coarsening of the clusters, where the smaller ones are subcritical in size and dissolving. This indicates that the cluster structure is still evolving, but the measured hardness is not changing much anymore. The NA 1 year condition revealed a very similar microstructure to the CA + NA 10 days condition with a slightly decreased Zn/Mg ratio indicating the coarsening of the microstructure to developed GP zones. The average size of clusters has slightly increased as compared to the CA + NA 10 days condition c.f. Table *8* and Figure 36(d) and e. Similar strengths for the NA 1 year as compared to the CA + NA 10 days can be strongly related to the similar microstructure in the two conditions.

Size estimates from APT data by a cluster identification method are expected to be sensitive to the considered representative material volume, and since the considered clusters are fine, a precise cluster analysis is challenging [27]. Hence, to provide an additional qualitative judgment of the trend on the evolution of the precipitate sizes, as seen by the cluster identification method, we also show the pair correlation function (PCF) in Appendix A. Analyzing the radial distribution function, as described by Zhao *et al.* [28] and also implemented in the previous study for the same alloy [25] provides a statistical approach, which gives a somehow better estimation of the average values within a dataset. Consistent with the cluster identification method, it can be concluded, also from analyzing the PCFs, that the size increased during the 10 days of storage after CA and the size after NA for 1 year is consistently larger than for the CA conditions.

Although the accumulated plastic strain during CA is large, most of the stored dislocations during the tensile load are removed during the reversal compression part of the cycle. A qualitative comparison between the dislocations observed by BF-TEM in, and dislocations seen by BF-TEM in the 2% pre-strained alloys in Ref [18], suggests that fewer dislocations are seen in CA conditions than by this relatively small pre-strain. The strength contribution from the dislocations stored during CA is smaller than the monotonic prestrain contribution of about 60 MPa, as estimated by Stemper *et al.*[18]. Since the strength, as well as the structure and chemistry of the GP zones, are quite similar for the CA and NA conditions, it is reasonable that the strength contribution from the GP zones is dominant, and that the contribution from the dislocations present in the CA conditions is very small compared to this.

4.3 Slant fractures in CA and NA samples

Surprisingly, the CA, CA + NA 10 days, and also the NA conditions, all experienced slant, ductile shear fractures for both 7046 and 7003 alloys. This fracture mode occurred at about the same strain as the uniform strain predicted by the Considère criterion for the onset of diffuse necking. The UTS and the uniform elongation reached after 1 year of NA were higher than for

the CA samples, indicating stronger work hardening for the NA condition and that the shear fracture seems to occur at the maximum force. The effect of Cu does not seem to influence the fracture mode since very similar results were obtained for the Cu free 7003 alloy.

Pedersen et al. [29] demonstrated similar abrupt shear fractures instead of diffuse necking, in tensile tests of a 7075 T651 alloy. In their investigation, the fracture was mainly brittle and following the grain boundaries. Whereas in the alloys studied here, the fracture can be regarded as mainly ductile, due to the presence of dimples and the bending of the grains close to the fracture surface as seen in Figure 35b. Only a few grains do not undergo bending/deformation.

Fe containing intermetallic constitutive particles are known to nucleate damage during plastic deformation, and thereby contribute to a decreased ductility [30]. Their size and number density increases with the Fe content. Such particles were observed in the bottom of the dimples in the fracture surfaces. The damage and void nucleation seem to be correlated with these particles. The question is whether the damage occurred as part of a flow instability leading to the shear fracture, or if the damage accumulated due to the plastic cyclic deformation, i.e., low-cycle fatigue, was the reason for the fracture to occur? To shed light on this question, the cyclically aged tensile samples for both 7046 and 7003 alloys, with accumulated low-cycle fatigue damage, were artificially aged at 140 ºC for ~8 hours. As this resulted in diffuse necking, similar to the peak aged condition and with considerable ductility (see Figure Figure 31d and Figure 32b), it is reasonable to argue that the shear fracture is not caused by the damage accumulated during the cyclic plastic deformation.

The microstructure after the subsequent artificial ageing is assumingly dominated by η' precipitates [31], as opposed to the high number density of clusters in the CA microstructure. Since the η' precipitates are well developed and larger precipitates, there will be more solute left in the matrix in the CA condition than it is after the subsequent artificial ageing. The Zn and Mg content of atoms in solid solution in the matrix will contribute to dynamic strain ageing (DSA). The Portevin Le Chatelier (PLC) instability, causing serrated yielding, can be seen as a few MPa serrations on the stress strain curves. The DSA can modify and enhance the strain localization during fracture. Chung *et al.* [15] observed a similar type of slant shear fracture, but for an as quenched 7075 alloy with significantly stronger dynamic strain ageing due to higher amounts of Mg and Zn in solid solution in this condition. Since they observed normal diffuse necking for tensile tests performed at -196°C, where the strain rate sensitivity was found to be positive, i.e. no DSA, they concluded, that the reason for this fracture mode in their case was the DSA. The fact that this type of shear fracture for 7003 alloy was found in both NA and cyclic aged conditions at room temperature as well as at -196°C (LN test), suggests that DSA is not the sole reason to the slant fractures observed for the NA and CA conditions considered here.

Wang *et al.* [32] observed similar shear fractures in C-Mn steels at elevated temperatures, at which dynamic strain ageing occurs in these alloys. They observed similar fracture surfaces, which are commonly referred to as slant fractures for these alloys. They found from finite element simulations that PLC bands, either inclined or conical PLC bands, traversed the uniform region during testing of thick tensile specimens. The conical bands lead to cup and cone fracture, while the inclined bands lead to ductile shear fractures, similar to those reported here. Note that simulations of an isotropic C-Mn steel [33] showed that the choice between a slant fracture and an axisymmetric cup and cone fracture depends sensitively on symmetry breaking perturbations. Hence, for a plate material with an orthotropic anisotropy, the slant fracture might be preferred. Furthermore, this might explain why the shear fracture did not

occur in tensile tests of the axisymmetric Al-Zn-Mg cyclic aged alloy tested by Sun *et al.* [2]. Finite element models containing different cracks in Al 2024 T3 alloys observed the direction of maximum effective plastic strain at the onset of crack growth to be strongly correlated with the orientation of the slant fracture surface[34].

Figure 32a and b distinguish the conditions that underwent slant fractures and diffuse necking phenomenon respectively. A clear trend is seen wherein the conditions with a microstructure of early-stage clusters and GP zones (as seen from the atom probe results in Figure 36) undergo slant fractures while the microstructure, which is more developed and dominated by η', undergoes diffuse necking. While the influence of DSA has been ruled out with the tests carried out at -196°C (LN tests, see Figure 32), the possible reason for these early slant fractures seem to be a combination of microstructure and plate material with an orthotropic anisotropy.

This type of fracture has not been reported for the cyclic aged Al-Zn-Mg alloys in earlier investigations [2]. It involves a very local shear flow instability. This fracture mode can be important in applications involving plastic deformations, e.g. in energy absorbing structures used for safety constructions like bumpers and crash boxes in a car. Precautions should be taken considering applications of cyclic and/or NA Al-Zn-Mg alloys in such safety constructions, where plastic deformations are involved. An interesting question is, whether this fracture mode may play a role also after artificial ageing, say for underaged conditions?

5. Conclusions

Processing parameters for room temperature cyclic aging have been optimized with respect to strength and ductility for two Al-Zn-Mg(-Cu) alloys. APT and TEM characterization after cyclic ageing reveal a high number density of clusters that grow during the subsequent NA occurring during 10 days of storage at room temperature and contributes to increased strength, while maintaining about the same uniform elongation in tensile tests.

An early shear fracture, denoted a slant fracture, is reported to occur for cyclic and for NA Al-Zn-Mg(-Cu) plate materials. Fracture surface investigations revealed dimples and plastically deformed grains near the fracture surface, from which it is concluded that it is a plastic flow instability causing the ductile shear fracture. Due to the presence of a normal diffuse necking instability after subsequent artificial ageing, it is concluded that the imposed fatigue damage during the cyclic deformation is not causing this instability and fracture mode. Furthermore, the same fracture mode is reported for the two alloys with and without Cu. The potential role of dynamic strain ageing in these early slant fractures was ruled out by low temperature tests in liquid nitrogen. It is argued that plate materials might be more prone for this fracture mode than axisymmetric materials. Special attention is required when considering cyclic or NA of Al-Zn-Mg alloys for applications requiring ductility at high strengths.

Data availability

The raw data used to reproduce the presented results are available in the Zenodo repository 10.5281/zenodo.6342915

Declaration of Competing Interest

The authors declare that they have no known competing financial interests or personal relationships that could have appeared to influence the work reported in this paper.

Acknowledgement

The authors wish to thank Hanne-Sofie Søreide for her support in the APT lab. The Research Council of Norway (RCN) is acknowledged for funding the NTNU atom probe facility through the Norwegian Laboratory for Mineral and Materials Characterization (MiMaC) project number: 269842. The RCN is further acknowledged for the support to the Norwegian Micro-and Nano-Fabrication Facility, NorFab. We thank Benteler automotives for providing material to carry out the study. The (S)TEM work was conducted on the NORTEM (NFR: 197405) infrastructure at the TEM Gemini Centre, Trondheim, Norway. E.T. acknowledges the NTNU Digital Transformation initiative 'Alldesign' and the 'SumAl' (NFR: 294933) project, supported by Hydro, Benteler Automotive Raufoss AS and Neuman Aluminium

Appendix A APT analysis

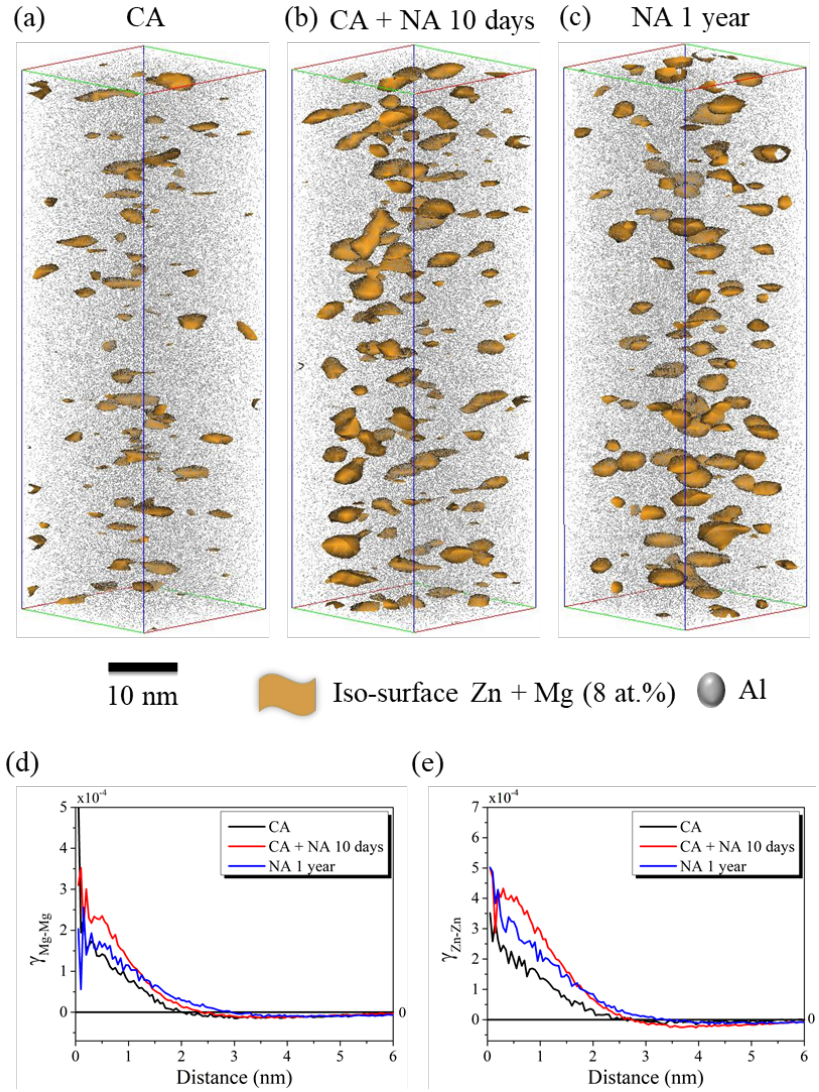

Figure 36. 25 x 25 x 80 nm^3 region of interest chosen from the 7046 APT datasets to magnify the visualization of clusters in the respective condition in (a) CA, (b) CA + NA 10 days and (c) NA 1 year. PCF of the above shown APT datasets for (d) Mg-Mg and (e) Zn-Zn pairs.

The iso-position method (IPM) [35] was used to identify clusters. This methodology is based on a solute concentration criterion, where a concentration value is estimated for each atom in the

analyzed volume. A concentration threshold of $C_{threshold}$ = 14% was used, for which the concentration histogram of a randomized dataset is negligible (less than 0.1%). A minimum number of atoms, N_{min} = 36 or 40 was required for the cyclic and cyclic + 10 days condition, to ensure that no clusters were identified in a randomized volume with $C_{threshold}$. A detailed explanation of how the clusters are defined and identified can be found elsewhere [35, 36]. A sub volume from each dataset was extracted and visualized to have a closer look at the clusters shown through Figure *36*(a) and (b), showing that 10 days further storage of the sample after the CA resulted in slightly larger clusters compared to the ones found immediately after CA.

The PCFs are plotted for Zn and Mg in Figure 36 (d and e). As explained by De Geuser and Gault [27], an increase in the width of the PCF indicates an increased correlation length, i.e. an increased cluster size. Hence, the PCFs suggests that the cluster size increased during the 10 days of storage after CA, and that the cluster sizes are larger for the NA for 1 year condition than for the CA condition.

Appendix B HAADF-STEM

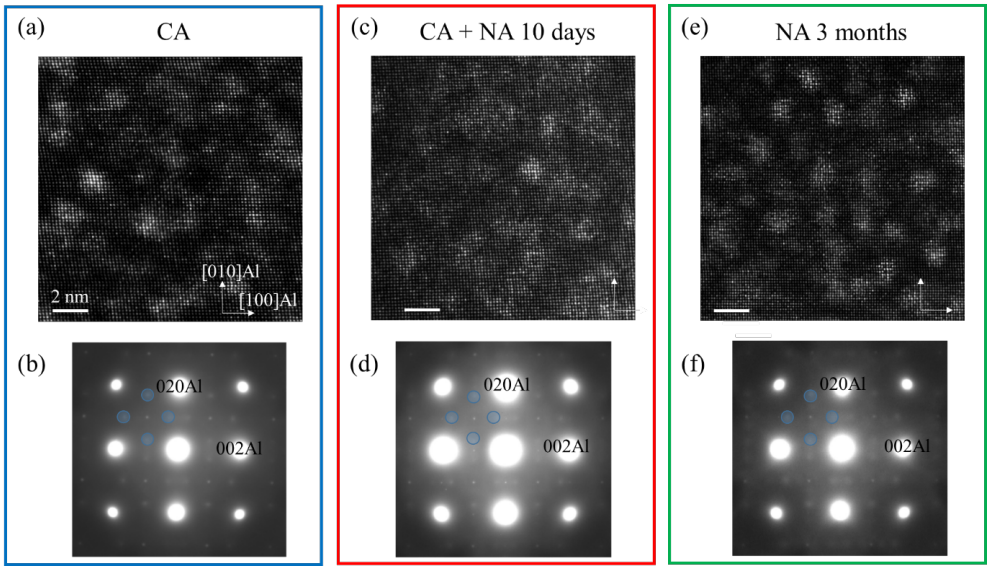

Figure 37. (a), (c), (e): HAADF-STEM images of the clusters in the CA, CA + 10 days and NA 3 months for 7046, respectively. (b), (d), (f): SADP from CA, CA + 10 days and NA 3 months for 7046, respectively. The blue disks in the SADPS indicate the diffracted intensities from the clusters, showing that the same type of clusters prevail in all three conditions.

Figure 37 shows HAADF-STEM images in (a), (c), (e) and SADP in (b), (d) and (f) from the 7046 alloy in the CA, CA + 10 days and NA 3 months condition. The 3 months condition was

chosen here since it is very similar in terms of hardness with the NA 1 year condition. The blue disks in the SADPs indicate the diffracted intensities from the clusters and exhibit good correspondence with the ones presented in Refs.. Both the HAADF-STEM images and SADP provide evidence that the same type of clusters, mainly GPI zones, are present in all three conditions.

6. References

1. Hornbogen, E., Hundred years of precipitation hardening. Journal of light metals, 2001. 1(2): p. 127-132.

2. Sun, W., et al., Precipitation strengthening of aluminum alloys by room-temperature cyclic plasticity. Science, 2019. 363(6430): p. 972-975.

3. Porter, D.A. and K.E. Easterling, Phase transformations in metals and alloys (revised reprint). 2009: CRC press.

4. Saada, G., Production de défauts ponctuels par écrouissage dans un métal cubique à faces centrées. Physica, 1961. 27(7): p. 657-660.

5. Chandler, H. and J. Bee, Cyclic strain induced precipitation in a solution treated aluminium alloy. Acta Metallurgica, 1987. 35(10): p. 2503-2510.

6. Han, W., et al., Dynamic precipitation during cyclic deformation of an underaged Al–Cu alloy. Materials Science and Engineering: A, 2011. 528(24): p. 7410-7416.

7. Deschamps, A., F. Livet, and Y. Brechet, Influence of predeformation on ageing in an Al–Zn–Mg alloy—I. Microstructure evolution and mechanical properties. Acta materialia, 1998. 47(1): p. 281-292.

8. Hörnqvist, M. and B. Karlsson, Effect of heat treatment on the strain hardening behaviour of an Al–Zn–Mg alloy. International journal of materials Research, 2009. 100(11): p. 1574-1581.

9. Pink, E. and W. Webernig, Precipitation during serrated flow in AlZn5Mg1. Acta Metallurgica, 1987. 35(1): p. 127-132.

10. Zhou, P., et al., Mechanical behavior and deformation mechanism of 7075 aluminum alloy under solution induced dynamic strain aging. Materials Science and Engineering: A, 2019. 759: p. 498-505.

11. Hutchinson, C., et al., Quantitative measurements of dynamic precipitation during fatigue of an Al–Zn–Mg–(Cu) alloy using small-angle X-ray scattering. Acta materialia, 2014. 74: p. 96-109.

12. Kalemba, I., et al., Natural Aging Behavior of Friction Stir Welded Al-Zn-Mg-Cu Aluminum Alloys. Archives of Metallurgy and Materials, 2015. 60.

Paper II

13. Zhang, P., et al., Solute cluster evolution during deformation and high strain hardening capability in naturally aged Al–Zn–Mg alloy. Acta Materialia, 2021. 207: p. 116682.

14. Chen, J., et al., Plastic flow and ductile rupture of a 2198 Al–Cu–Li aluminum alloy. Computational Materials Science, 2011. 50(4): p. 1365-1371.

15. Chung, N., et al., Unstable shear failure in a 7075 aluminum alloy. Acta Metallurgica, 1977. 25(4): p. 377-381.

16. Fjeldly, A. and H.J. Roven, Effects of strain rate and anisotropy on the tensile deformation properties of extruded AlZnMg alloys. Metallurgical and Materials Transactions A, 2000. 31(3): p. 669-678.

17. Pink, E., W. Bernt, and M. Fellner, Flow and fracture of aluminum alloys and of iron and steel within and outside the range of inhomogeneous flow. Scripta Metallurgica et Materialia;(United States), 1993. 28(9).

18. Stemper, L., et al., Giant hardening response in AlMgZn (Cu) alloys. Acta Materialia, 2021. 206: p. 116617.

19. Stephenson, L.T., et al., New techniques for the analysis of fine-scaled clustering phenomena within atom probe tomography (APT) data. Microscopy and Microanalysis, 2007. 13(6): p. 448-463.

20. Fagerholt, E., Field measurements in mechanical testing using close-range photogrammetry and digital image analysis. 2012.

21. Gault, B., et al., Atom probe microscopy. Vol. 160. 2012: Springer Science & Business Media.

22. Samudrala, S., et al., A graph-theoretic approach for characterization of precipitates from atom probe tomography data. Computational Materials Science, 2013. 77: p. 335-342.

23. Atom Probe Tomography (APT) - Department of Materials Science and Engineering - NTNU. 2022; Available from: https://www.ntnu.edu/ima/research/apt.

24. Gault, B., et al., Advances in the calibration of atom probe tomographic reconstruction. Journal of Applied Physics, 2009. 105(3): p. 034913.

25. Shah, S., et al., Effect of cyclic ageing on the early-stage clustering in Al–Zn–Mg (-Cu) alloys. Materials Science and Engineering: A, 2022: p. 143280.

26. Shi, L., et al., The effect of chemical patterning induced by cyclic plasticity on the formation of precipitates during aging of an Al–Mg–Si alloy. Materials Science and Engineering: A, 2021. 815: p. 141265.

27. De Geuser, F. and B. Gault, Metrology of small particles and solute clusters by atom probe tomography. Acta Materialia, 2020. 188: p. 406-415.

28. Zhao, H., et al., Parameter free quantitative analysis of atom probe data by correlation functions: Application to the precipitation in Al-Zn-Mg-Cu. Scripta Materialia, 2018. 154: p. 106-110.

Paper II

29. Pedersen, K.O., T. Børvik, and O.S. Hopperstad, Fracture mechanisms of aluminium alloy AA7075-T651 under various loading conditions. Materials & Design, 2011. 32(1): p. 97-107.

30. Taylor, J.A. The effect of iron in Al-Si casting alloys. in 35th Australian foundry institute national conference. 2004. Australian Foundry Institute (AFI).

31. Löffler, H., I. Kovács, and J. Lendvai, Decomposition processes in Al-Zn-Mg alloys. Journal of Materials Science, 1983. 18(8): p. 2215-2240.

32. Wang, H., et al., Portevin–Le Chatelier (PLC) instabilities and slant fracture in C–Mn steel round tensile specimens. Scripta Materialia, 2011. 64(5): p. 430-433.

33. Ren, S., et al., A constitutive model accounting for strain ageing effects on work-hardening. Application to a C–Mn steel. Comptes Rendus Mécanique, 2017. 345(12): p. 908-921.

34. Lan, W., et al., Study of slant fracture in ductile materials. International journal of fracture, 2006. 141(3): p. 469-496.

35. Lefebvre, W., F. Vurpillot, and X. Sauvage, Atom probe tomography: put theory into practice. 2016: Academic Press.

36. Hyde, J.M., et al., Analysis of radiation damage in light water reactors: comparison of cluster analysis methods for the analysis of atom probe data. Microscopy and Microanalysis, 2017. 23(2): p. 366-375.

Supplementary Information for

Early slant ductile fracture characteristics of cyclic and naturally aged Al-Zn-Mg(-Cu) alloys and its effect on precipitation and strength

1. Specimen Geometry for Cyclic Strengthening Experiments

Samples for cyclic strengthening were cut from 6 mm thick sheets which were heavily cooled by water during extrusion. The specimen geometry for the cyclic treatments and the tensile test is given in Figure S1(a). Thickness of sample was 6 mm. Tensile tests in liquid nitrogen (LN) were carried out on smaller samples due to setup limitations and the geometry is shown in Figure S1(b).

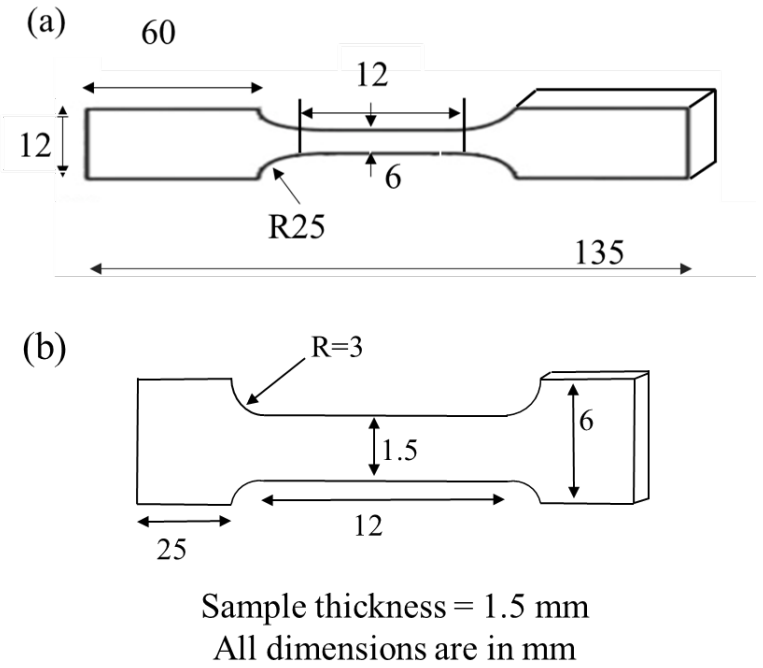

Figure S1. (a) Sample geometry for cyclic and subsequent tensile tests. (b) Sample geometry of tensile tests in LN.

2. Test for Optimizing Number of Cycles and Maximum Stress to be reached

While choosing the maximum targeted strength (σ_{target}) close to the yield stress, we saw that the samples were prematurely fracturing indicating strain localization. In such a scenario, we decided to go for a lower maximum stress while doing it with minimum number of cycles but enough to prevent strain localization and fracture of samples.

Figure S2 shows the optimization considerations used after optimising a targeted stress of slightly less than 400 MPa. Using 400 MPa resulted in extremely high plastic strain accumulation (>3) even after regulating the number of cycles.

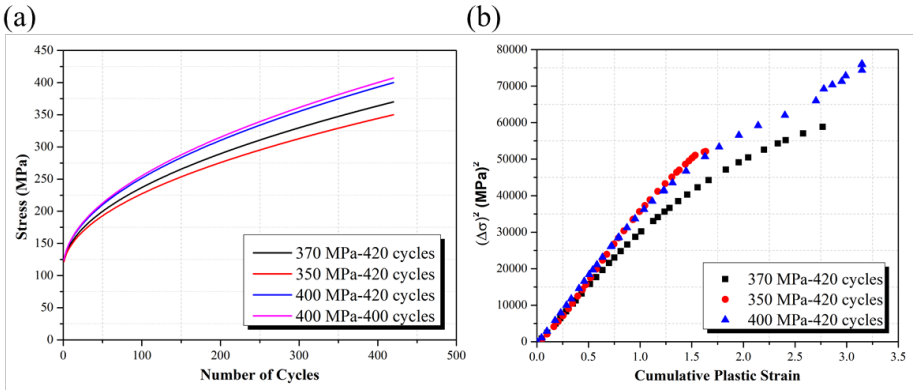

Figure S2. Optimization of cycles and targeted stress. (a) Targeted stress with different cycles and (b) square of cyclic hardening increment as a function of half of cumulative plastic strain.

Slightly lower targeted stress (350 and 370 MPa) yielded better results and hence an intermediate targeted stress of 370 MPa and 420 cycles was chosen for all the different frequency runs used in this study. This optimization study was done for a frequency of 0.13 Hz.

Tests for 700 cycles to reach the same targeted stress was also performed. As expected, the total accumulated plastic strain was lower than the 420 cycle run (Figure S3). However, this did not have any significant improvements in the mechanical response between the two as shown in Table1.

Paper II

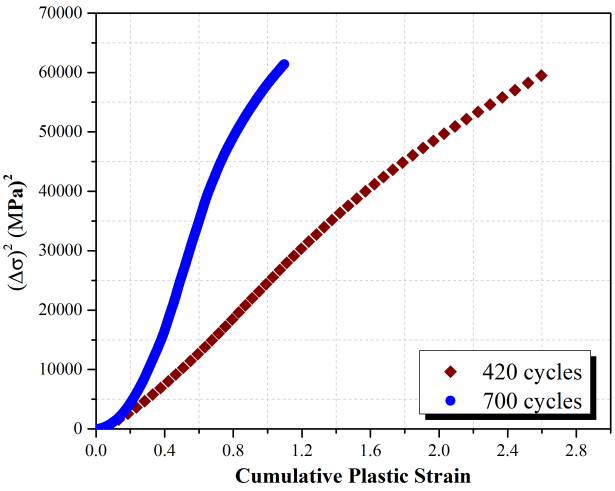

Figure S3. Variation in the cumulative plastic strain for different cycles for a set targeted stress of 370 MPa.

Table 1. Yield Strength and Ultimate Tensile Strength for different cycle runs at 0.025 Hz.

	420 cycles	700 cycles
Yield Strength	424	407
Ultimate Tensile Strength	506	471

Table 2. True fracture strains for 7003 and 7046

Sample	7003			7046		
	Initial	Final	True fracture strain	Initial	Final	True fracture strain
CA	36	33	8.70	37.50	34.44	8.51
CA + NA 10 days	36	33.162	8.21	37.20	32.25	14.28
CA + Peak Aged	36	25.597	34.10	36	29.04	21.47
NA 1 year	2.26	1.936	15.68	2.23	1.80	21.58
NA 1 year + Peak Aged	2.23	1.69	27.94	2.26	1.67	30.11
NA ~ 1 year (LN) test	2.22	1.834	19.10			
Peak Aged	36	24.667	37.80	36	28.25	24.24

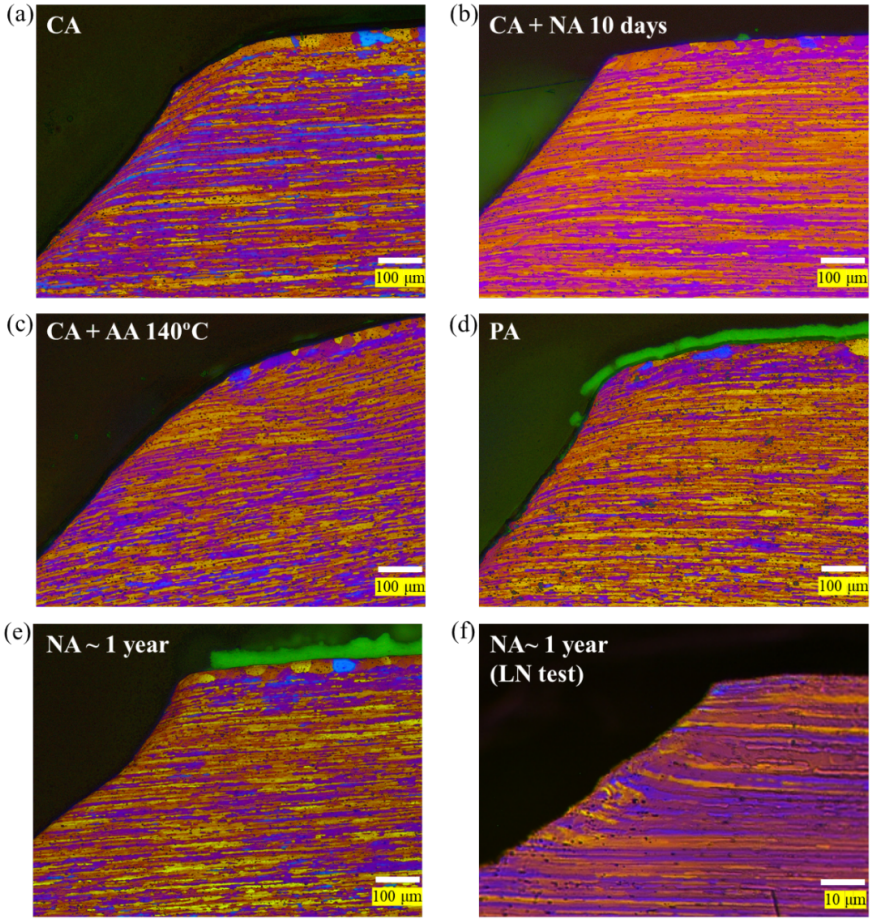

Figure S4. Optical images of grains ending in shear fracture, taken from the transverse direction for (a) CA, (b) CA + NA 10 days, (c) CA + AA 140°C, (d) PA, (e) NA 1 year and (f) NA 1 year tested in liquid nitrogen.

Paper III

Shah, Sohail; Thronsen, Elisabeth; De Geuser, Frederic; Hatzoglou, Constantinos; Marioara, Calin Daniel; Holmestad, Randi; Holmedal, Bjørn. “Comparison of a cluster identification method to a statistical approach for analyzing atom probe tomography data for GP zones in Al- Zn-Mg(-Cu) alloys”. Manuscript ready for submission in Microscopy and Microanalysis.

This paper is not yet published and is therefore not included.

Paper IV

Thronsen, Elisabeth; Shah, Sohail; Hatzoglou, Constantinos; Marioara, Calin Daniel Wenner, Sigurd; Anderson, Sigmund J.; Holmedal, Bjørn; Holmestad, Randi. “The evolution of precipitates in an Al-Zn-Mg alloy”. Ready for submission in Journal of Alloys and Compounds.

This paper is not yet published and is therefore not included.

ISBN 978-82-326-6580-8 (printed ver.)
ISBN 978-82-326-6973-8 (electronic ver.)
ISSN 1503-8181 (printed ver.)
ISSN 2703-8084 (online ver.)

NTNU

Norwegian University of
Science and Technology